

Metal Phosphate and Oxide based Electroactive Material for Energy Conversion and Storage Application

By

Abhisek Padhy

CHEM11201804001

**National Institute of Science Education and Research (NISER),
Jatani, Khurda, Odisha-752050**

*A thesis submitted to the
Board of Studies in Chemical Sciences*

In partial fulfillment of requirements for the Degree of

DOCTOR OF PHILOSOPHY

of

HOMI BHABHA NATIONAL INSTITUTE



August, 2023

Homi Bhabha National Institute¹

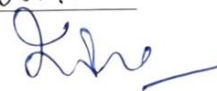
Recommendations of the Viva Voce Committee

As members of the Viva Voce Committee, we certify that we have read the dissertation prepared by Abhisek Padhy entitled “Metal Phosphate and Oxide-based Electroactive Material for Energy Conversion and Storage Application” and recommend that it may be accepted as fulfilling the thesis requirement for the award of Degree of Doctor of Philosophy.

Chairman - Name & Signature with date Prof. A. Srinivasan

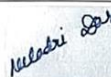


Guide / Convener - Name & Signature with date Dr. Jogendra Nath Behera



Co-guide - Name & Signature with date (if any)

Examiner - Name & Signature with date Dr. Neeladri Das



Member 1- Name & Signature with date Dr. Chandra Shekhar Purohit



Member 2- Name & Signature with date Dr. Moloy Sarkar



Member 3- Name & Signature with date Dr. Srikanta Patra



Final approval and acceptance of this thesis is contingent upon the candidate's submission of the final copies of the thesis to HBNI.

I/We hereby certify that I/we have read this thesis prepared under my/our direction and recommend that it may be accepted as fulfilling the thesis requirement.

Date: 22/08/2023

Place: NISER.

Signature

Co-guide (if any)

Signature

Guide



¹ This page is to be included only for final submission after successful completion of viva voce.

STATEMENT BY AUTHOR

This dissertation has been submitted in partial fulfilment of requirements for an advanced degree at Homi Bhabha National Institute (HBNI) and is deposited in the library to be made available to borrowers under rules of the HBNI.

Brief quotations from this dissertation are allowable without special permission, provided that accurate acknowledgement of source is made. Requests for permission for extended quotation from or reproduction of this manuscript in whole or in part may be granted by the Competent Authority of HBNI when in his or her judgment the proposed use of the material is in the interests of scholarship. In all other instances, however, permission must be obtained from the author.

Abhishek Padhy.

Name & Signature of the student

DECLARATION

I, hereby declare that the investigation presented in the thesis has been carried out by me. The work is original and has not been submitted earlier as a whole or in part for a degree / diploma at this or any other Institution / University.

Abhishek Padhy.

Name & Signature of the student

LIST OF PUBLICATIONS

(a) Published

1. Cobalt pyrophosphate ($\text{Co}_2\text{P}_2\text{O}_7$) derived from an open-framework cobalt phosphite: a durable electroactive material for electrochemical energy conversion and storage application, **Abhisek Padhy**, Aneeya K. Samantara, J. N. Behera, *Sustainable Energy & Fuels*, 5, 14, 2021, 3729-3736.
2. A synergistic electrochemical approach of boron-doped carbon/cobalt pyrophosphate//MXene for high-performance all solid-state asymmetric devices, **Abhisek Padhy**, R. Samal, C S Rout, J. N. Behera, *Sustainable Energy & Fuels*, 6, 8, 2022, 2010-2019.
3. Revealing the electrochemical performance of a manganese phosphite/RGO hybrid in acidic media, **Abhisek Padhy**, R. Kumar, J. N. Behera, *Dalton Transactions*, 51, 42, 2022, 16256-16265.
4. Prussian blue analogue (PBA) derived cobalt telluride nano-granules: an efficient catalyst for energy conversion and storage, Rajat K. Tripathy, **Abhisek Padhy**, N. Sahu, J. N. Behera, *Sustainable Energy & Fuels*, 6, 18, 2022, 4146-4152.
5. Tetra germanium nonaselenide enwrapped with reduced graphene oxide and functionalized carbon nanotubes ($\text{Ge}_4\text{Se}_9/\text{RGO}/\text{FCNTs}$) hybrids for improved energy storage performances, Jiban K. Das, **Abhisek Padhy**, S. Parida, R. M. Pathi, J. N. Behera, *Dalton Transactions*, 51, 30, 2022, 11526-11535.

Communicated

1. Synthesis and electrochemical study of $\text{SnO}_2/\text{Ti}_3\text{C}_2\text{T}_x$ hybrid towards supercapacitor application, **Abhisek Padhy**, J. N. Behera.

CONFERENCES

1. **Presented** a virtual **poster** at **Catalysis science and technology 10th anniversary** symposium 2021 organized by RSC during November **16 - 17, 2021**.
2. **Participated and presented a poster** at the **ACS CRSI poster session** of 27th CRSI-National Symposium Chemistry held at the Novotel Hotel, Kolkata during **September 26 – 29, 2021**.
3. **Participated and presented a virtual poster** on **Recent Advances in Catalysis Science and Engineering (RACSE)** at 27th International Conference of International Academy of Physical Sciences. Organized by NIT Jamshedpur During **October 26 - 28, 2021**.

Abhishek Padhy.

Name & Signature of the student

**Dedicated to
(My Beloved Parents)**

ACKNOWLEDGEMENTS

I would like to thank **my supervisor Dr. Jogendra Nath Behera**, for continuous support, encouragement, patience exhibited and freedom provided for free thinking.

I am thankful to **Prof. Sudhakar Panda, Director-NISER**, for the laboratory facilities and financial support.

I thank my Doctoral committee members, **Prof. A. Srinivasan** and **Dr. C. S. Purohit, Dr. Moley Sarkar, Dr. Srikanta Patra** and all the faculty members in SCS.

I warmly thank our collaborator, **Dr C. S. Rout (JAIN UNIVERSITY, BENGALURU)**.

I thank all my past and present lab members Dr Jiban K. Das, Dr Rajat K. Tripathy, Dr Malaya k Sahoo, Nachiketa, Manisha, Kismat, Vamsi, R. Pathi, Deepak, Nikhil, Rahul, Smruti and Ayushi for their continuous support and valuable discussion.

I thank all my friends, especially Nachiketa, Tanmay, Sahadev and Shyam for their scientific discussions and moral support.

Above all, I would like to thank my parents, sister, nephew and beloved wife for their unconditional love, care and support in this challenging but beautiful journey.

CONTENTS

Sl. No.	Titles	Page No.
1	Recommendations of the Viva Voce Committee	i
2	Statement by Author	ii
3	Declaration	iii
4	List of Publication	iv
5	Conferences	v
6	Dedication	vi
7	Acknowledgements	vii
8	Contents	viii
9	Motivation and Objective	ix
10	Synopsis	x
11	List of Schemes	xvii
12	List of Figures	xviii
13	List of Tables	xxii
14	List of Abbreviations	xxiii
15	Chapter 1	1-34
16	Chapter 2	35-53
17	Chapter 3	54-79
18	Chapter 4	80-104
19	Chapter 5	105-124

MOTIVATION AND OBJECTIVE

Research on electrochemical energy conversion and storage applications is motivated by the increasing global demand for clean and sustainable energy solutions. The primary objective of this research is to develop efficient, reliable, and environmentally friendly technologies to address the challenges posed by fossil fuel depletion, climate change, and the need for decentralised energy sources. Fossil fuels are finite and contribute to environmental pollution and climate change. Electrochemical energy conversion and storage technologies offer the potential to harness renewable energy sources (such as solar and wind) and convert/store them efficiently, reducing our dependence on fossil fuels. As we know, renewable energy sources like solar and wind are intermittent, meaning they don't produce energy consistently. Effective energy storage solutions, such as batteries and supercapacitors, are crucial to storing excess energy generated during peak production times and releasing it when demand is high. However, the cost, efficiency, energy density, power density, cyclic stability and durability still remains a major issue that needs to be tackled. Thus, in my research work, I am motivated to develop an electroactive material that can show high efficiency towards oxygen evolution reaction and shows maximum energy and power density with high cyclic stability.

SYNOPSIS

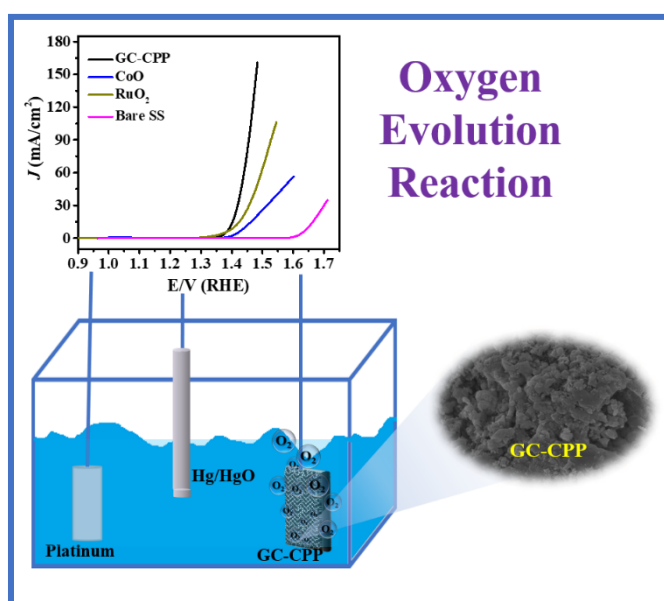
This present thesis involves the study of various metal phosphate and oxide-based materials for electrochemical energy conversion and storage application. The thesis comprises of five chapters. **Chapter 1:** Includes the introduction part where the motivation for the search of alternative electrode materials towards electrochemical energy conversion and storage application is explained. Along with that the basic information regarding the characterization techniques and electrochemical parameters are also explained. **Chapter 2:** Explains the detailed study on cobalt pyrophosphate ($\text{Co}_2\text{P}_2\text{O}_7$) as a durable electroactive material for electrochemical energy conversion application. **Chapter 3:** Presents the detailed analysis of Boron doped carbon/cobalt pyrophosphate hybrid towards high-performance all solid-state asymmetric supercapacitor device. **Chapter 4:** Reveals the electrochemical performance of a manganese phosphite/RGO hybrid in acidic media. **Chapter 5:** Presents the synthesis and electrochemical study of $\text{SnO}_2/\text{Ti}_3\text{C}_2\text{T}_x$ hybrid towards supercapacitor application.

Chapter 1: Introduction

The recent increase in energy demand has led to a greater focus on renewable energy sources like oxygen (O_2) and hydrogen (H_2), that can be produced through a straightforward electrochemical water splitting process while ignoring the effects of greenhouse gases.¹ This chapter provides an overview of the energy conversion process, including the two half-cell reactions in the respective electrodes. Where in the cathodic half-cell hydrogen evolution reaction (HER) and in anode oxygen evolution reaction (OER) takes place. The basic working principles, the mechanism of overall surface reactions, various precious or non-precious metal based materials as electrode materials to carry out HER and OER, and various carbon-based materials used for mechanical support and further improvement of electrocatalytic performances of the as-prepared catalyst, various synthetic technique using which they can be synthesized, and common parameters employed for the energy conversion process is elaborated in this chapter.²⁻⁵ Like energy conversion process, the energy storage system towards supercapacitor application plays a crucial part in the current energy sector and opens up new doors to meet future energy demands.⁶⁻⁸ This chapter also discusses the significance of

supercapacitors in comparison to conventional capacitors and batteries based on energy storage devices.⁹ Furthermore, this chapter also covers the supercapacitor's operating principles, the mechanism involved in the charge storage process, electrode materials used to boost supercapacitor performance, various electrochemical experiments, and the evaluation techniques involved to calculate the storage performance.

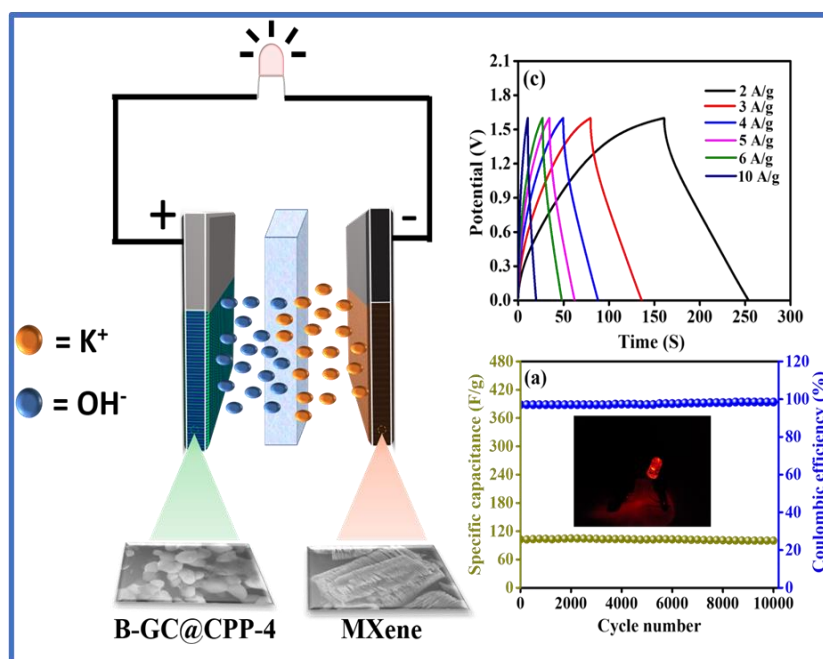
Chapter 2: Cobalt pyrophosphate ($\text{Co}_2\text{P}_2\text{O}_7$) a durable electroactive material for electrochemical energy conversion application.



Graphical abstract

In this work, we have derived a hybrid structure of partially graphitized carbon/cobalt pyrophosphate (GC-CPP) from an inorganic open-framework cobalt phosphite by annealing at an optimized temperature under inert atmosphere. After successful synthesis and step-by-step physicochemical analysis, the electrochemical oxygen evolution reaction is carried out in three electrode set-ups. Oxygen evolution reaction (OER) is analyzed in freshly prepared 3 M KOH electrolyte. On employing as anode electrocatalyst, the GC-CPP catalyzes the OER efficiently which needs only 165 mV of overpotential to reach 10 mA cm⁻² current density. Also, it endows the catalysis process with favorable kinetics showing a Tafel slope of 41 mV dec⁻¹ and robust durability (increase of only 10 mV overpotential after 20 hours of electrolysis) with an unaltered crystallinity as well as surface morphology.

Chapter 3: Boron doped carbon/cobalt pyrophosphate hybrid for high-performance all solid-state asymmetric supercapacitor device.

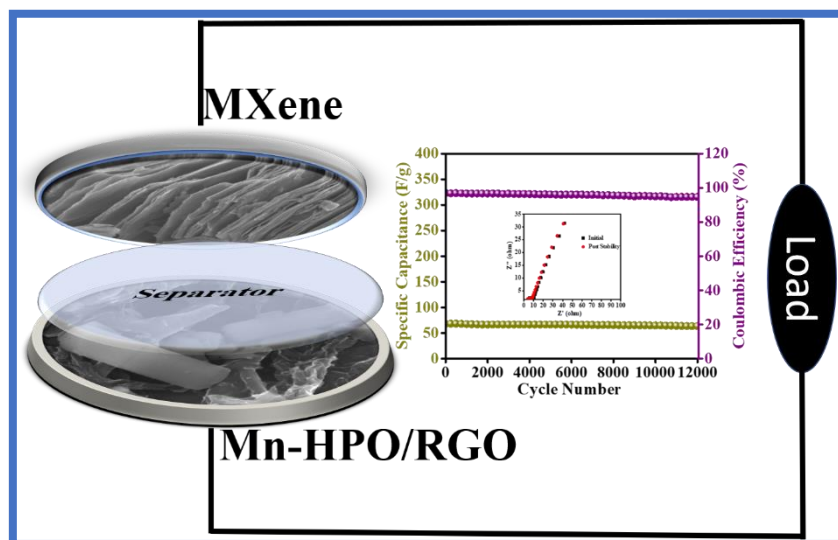


Graphical Abstract

In the present chapter, boron doped carbon/cobalt pyrophosphate hybrid for supercapacitor application is studied. The presence of boron in the carbon matrix increases the pseudocapacitive behavior of the carbon. Furthermore, the excellent stability of cobalt pyrophosphate and the inherent redox behavior of cobalt provides an opportunity to employ this hybrid as a positive active material. Herein, a two-step process is followed for the synthesis of a boron-doped carbon/ cobalt pyrophosphate hybrid. Through the appropriate adjustment of the amount of boron during synthesis, the electrochemical performances of a set of materials were studied. The material synthesized with 4 mg of boron (B-GC@CPP-4) exhibited a specific capacitance of 395.1 F g^{-1} at 1.5 A g^{-1} mass normalized current density. Boron, with one electron less than carbon, is the vital reason behind the improved electrochemical performance of the hybrid material. However, the intrinsic hydrophilicity and metallic conductivity of MXene make it an eminent electroactive material for use as a negative electrode. Owing to the above properties, the all-solid-state asymmetric supercapacitor cell (ASC) was fabricated [B-GC@CPP-4// MXene], that exhibits a specific capacitance of 125 F g^{-1}

with an energy density of 45 W h kg^{-1} at a power density of 1735 W kg^{-1} at 2 A g^{-1} current density. The ASC device possesses an excellent coulombic efficiency of 98.5% and capacitance retention of 96% over 10000 consecutive charge/discharge cycles. The study reveals B-GC@CPP-4//MXene to be a promising set-up for energy storage devices.

Chapter 4: Revealing the electrochemical performance of a manganese phosphite/RGO hybrid in acidic media.

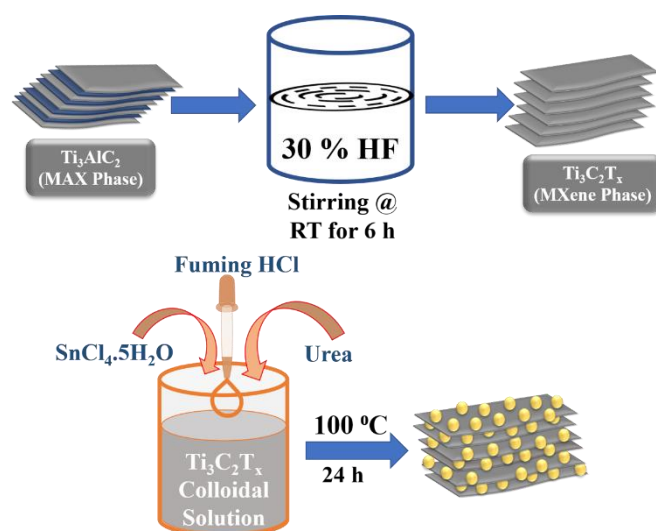


Graphical Abstract

Herein, we present manganese phosphite $[\text{Mn}_{11}(\text{HPO}_3)_8(\text{OH})_6]$, an interesting inorganic material with spectacular structural features for supercapacitor application. A single step hydrothermal synthetic route was employed for the fabrication of a series of manganese phosphite/RGO hybrids (Mn-HPO/RGO-5, Mn-HPO/RGO-10, Mn-HPO/RGO-20). Among all the as-synthesized hybrid, Mn-HPO/RGO-10 delivers a specific capacitance of 770 F g^{-1} when operated at 1 A g^{-1} current density in three-electrode set-up and maintains a rate capability of 66%. To broaden the practical applicability of the Mn-HPO/RGO-10 hybrid, an asymmetric supercapacitor (ASC) device was fabricated with MXene ($\text{Ti}_3\text{C}_2\text{T}_x$) as a negative electroactive material and a Mn-HPO/RGO-10 hybrid as a positive active material. The as-fabricated device projects a specific capacitance of 108 F g^{-1} with an energy density of 34 W h kg^{-1} at a power density of 508 W kg^{-1} . Moreover, the ASC device retains a specific capacitance of 94% after 12 000 constant charge and discharge cycles, suggesting the excellent

durability of the ASC device. These systematic investigations illustrate the potential of the Mn-HPO/RGO-10 hybrid as a positive active material for high-performance energy storage device in acidic electrolytic condition.

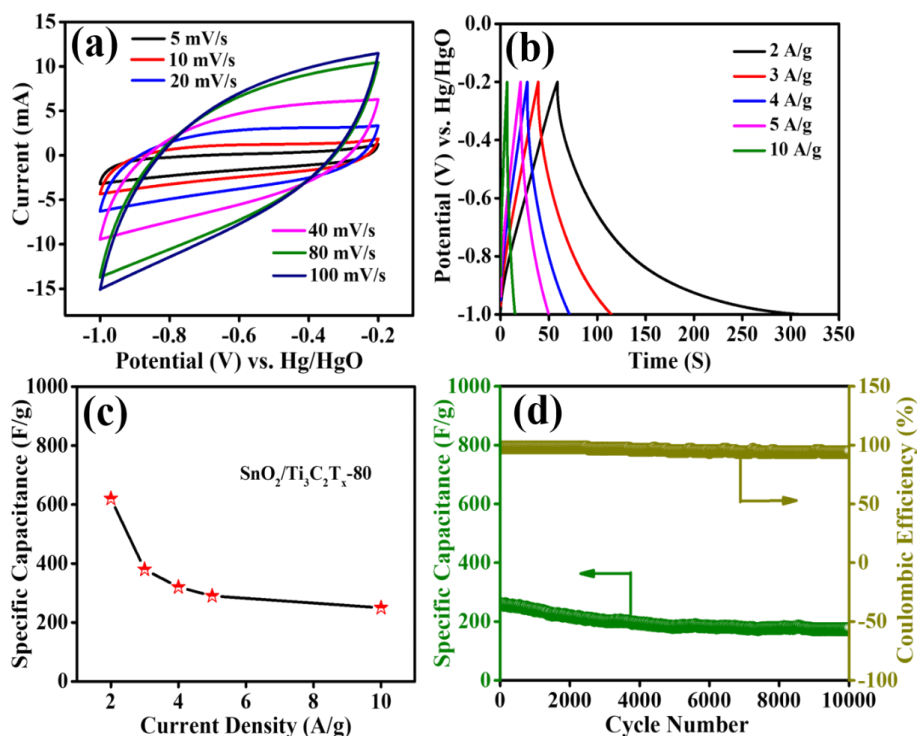
Chapter 5: Presents the synthesis and electrochemical study of $\text{SnO}_2/\text{Ti}_3\text{C}_2\text{T}_x$ hybrid towards supercapacitor application.



Reaction Scheme

In this chapter, we report a single step hydrothermal route to synthesize $\text{SnO}_2/\text{Ti}_3\text{C}_2\text{T}_x$ composites with varying the amount of $\text{Ti}_3\text{C}_2\text{T}_x$ from 50 to 100 mg. After successful synthesis of the pristine SnO_2 , $\text{Ti}_3\text{C}_2\text{T}_x$ and $\text{SnO}_2/\text{Ti}_3\text{C}_2\text{T}_x$ hybrids, the phase purity is confirmed through powder XRD analysis, the morphology was analysed through FESEM, TEM and HRTEM. FESEM images of SnO_2 reveals the agglomerated morphology that is further intercalated in between the $\text{Ti}_3\text{C}_2\text{T}_x$ layers in the hybrid material. Moreover, the TEM image of SnO_2 disclose that the agglomerated architecture is actually the composed of small rice grain type nanoparticles. However, the interlayer spacing of $\text{Ti}_3\text{C}_2\text{T}_x$ in $\text{SnO}_2/\text{Ti}_3\text{C}_2\text{T}_x$ -80 hybrid is increased can be observed from HRTEM analysis. This increase in interlayer spacing again facilitates the charge transport in supercapacitor electrode.¹⁰ Afterwards the electrochemical study of $\text{SnO}_2/\text{Ti}_3\text{C}_2\text{T}_x$ -80 shows better supercapacitor performance compared to pristine SnO_2 , $\text{Ti}_3\text{C}_2\text{T}_x$ and other synthesized composites. In three electrode set-up $\text{SnO}_2/\text{Ti}_3\text{C}_2\text{T}_x$ -80 delivers a specific capacitance of 620 F/g with a rate capability of 42 %. After 10,000

cycles of constant charge and discharge at 10 A/g, it was found that the electrode retains 73 % of its initial capacitance.



(a) CV, (b) GCD, (c) Csp values at different current density, (d) Stability and coulombic efficiency of SnO₂/Ti₃C₂T_x-80 hybrid.

Synopsis Conclusion

Water electrolysis or water splitting reaction is the most viable and cheapest method to produce H₂. The electrolysis of water molecules requires, a theoretical potential of 1.23 V. But in actual use, a greater cell voltage is essential because of a number of internal and external factors, that reduces efficiency all around. Despite the fact that some noble metals, such as platinum, iridium, and rhodium, have demonstrated exceptional electrocatalytic activity, their precious metal status in terms of high cost and availability holds them back for large scale commercialization. Similarly, the commercial or domestic use of electricity requires a continuous and smooth flow, consequently calls for suitable storage devices to be coupled with these intermittent renewable energy sources. The energy storage systems such as batteries, supercapacitors and capacitor store electrical energy through electrochemical process

and supplies them as required. Based upon these ideas, in the present thesis work initially the details of electrochemical energy conversion and storage application is explained in chapter 1. Then in chapter 2, I, have synthesized graphitized carbon/cobalt pyrophosphate (GC-CPP) from a cobalt phosphite open framework and studied its electrochemical performance towards oxygen evolution reaction. Furthermore, in chapter 3 this cobalt phosphite open framework is used as a precursor material along with boron powder to synthesize boron doped carbon/cobalt pyrophosphate (B-GC@CPP) and its supercapacitor performance is studied in 3 M KOH electrolyte. Again, in search of new electrode material for supercapacitor application I have further explored the supercapacitor performance of Manganese phosphite/RGO hybrid (Mn-HPO/RGO) in acidic electrolyte (1 M H₂SO₄) in chapter 4. Moreover, SnO₂/Ti₃C₂T_x hybrid is synthesized through a simple hydrothermal process. The incorporation of SnO₂ in between Ti₃C₂T_x layers increases the interlayer spacing, facilitating the charge transport in the electrode material makes it a suitable choice for supercapacitor application in KOH electrolyte and studied in chapter 5.

LIST OF SCHEMES

Scheme No.	Caption	Page No.
Scheme 2.1	Schematic representation for the Synthesis of cobalt pyrophosphate (GC-CPP)	39
Scheme 3.1	Schematic representation for the Synthesis of B-GC@CPP	59
Scheme 4.1	Schematic representation for the Synthesis of Mn-HPO/RGO hybrid	86
Scheme 5.1	Schematic representation for the synthesis of SnO ₂ /Ti ₃ C ₂ T _x hybrid	110

LIST OF FIGURES

Figure No.	Caption	Page No.
Figure 1.1	A typical three electrode set-up	4
Figure 1.2	Two electrode system showing electrolysis process	5
Figure 1.3	Mechanism of hydrogen evolution reaction in acidic and alkaline media	7
Figure 1.4	Mechanism of OER in both alkaline (red line) and acidic medium (blue line)	8
Figure 1.5	Graphical representation of Tafel plot showing linear Tafel region and Exchange current density	10
Figure 1.6	(a) CV curve showing Faradaic and non-Faradaic region, (b) Enlarged CV curves in non-Faradaic region, (c) Cathodic and anodic slope to evaluate C_{dl}	11
Figure 1.7	Nyquist plot of pristine and Fe/P dual doping CoS_2 polycrystalline nanowire for HER showing EIS.	13
Figure 1.8	long-term stability at 10 mA/cm^2 current density for graphitized carbon cobalt pyrophosphate (GC-CPP)	15
Figure 1.9	For HER activity of electrocatalyst vs. calculated Gibb's free energy	16
Figure 1.10	Various components of a supercapacitor device	20
Figure 1.11	Helmholtz model for the electrical double-layers	21
Figure 1.12	Schematic representation showing EDL capacitor	21
Figure 1.13	Representation of various pseudocapacitive process	22
Figure 1.14	EIS of the cobalt nickel phosphate electrodes with different ratios	25
Figure 2.1	(a) XRD and (b) IR spectra of synthesized GC-CPP	41
Figure 2.2	(a) Raman Spectra of $CoHPO-CJ2$ & GC-CPP	42
Figure 2.3	(a) FESEM, (b-c) HRTEM and (d) SAED pattern of GC-CPP	43
Figure 2.4	(a) survey and high-resolution X-ray photoelectron spectrum of (b) Co 2p, (c) P 2p, (d) O 1s and (e) C 1s of GC-CPP	44
Figure 2.5	(a) Linear sweep voltammogram, (b) Tafel plot, (c) Nyquist impedance spectrum	45

Figure No.	Caption	Page No.
Figure 2.6	(a), (c) & (e) Cyclic voltammograms at different sweep rate in non-Faradic potential window, (b), (d) & (f) plot of cathodic and anodic current against sweep rate for GC-CPP, RuO ₂ and CoO respectively.	47
Figure 2.7	(a) Long term stability at 10 mA/cm ² current density for GC-CPP, (b) LSV before and after 20 hours of stability test.	48
Figure 2.8	(a) PXRD and (b) FESEM of GC-CPP post OER	48
Figure 2.9	(a) Survey and high-resolution X-ray photoelectron spectrum of (b) Co 2p, (c) P 2p, and (d) O 1s of GC-CPP after OER stability measurement	49
Figure 3.1	FESEM images of (a) MAX (Ti ₃ AlC ₂) and (b) MXene (Ti ₃ C ₂)	60
Figure 3.2	(a) Raman spectra (b) PXRD patterns of GC@CPP and B-GC@CPP-4	63
Figure 3.3	(a) Full-range survey spectra of B-C@CPP-4. (b)–(f) Fine spectra of B 1s, C 1s, Co 2p, P 2p and O 1s, respectively.	64
Figure 3.4	(a) and (d) FESEM, (b), (e) and (c), (f) TEM and HRTEM images of GC@CPP and B-GC@CPP-4 respectively.	64
Figure 3.5	SEM images of B-GC@CPP with varying boron quantity from 0 to 8 mg (0, 2, 4, 8mg)	65
Figure 3.6	(a) CVs at different scan rates, (b) log(i) vs. log(v), (c) GCD curves at different current densities. (d) C _{sp} at various current densities.	67
Figure 3.7	(a) CV at 5 mV/s and (b) GCD at 1.5 A/g for B-GC@CPP with varying Boron quantity (c) C _{sp} values at 1.5 A/g with varying boron quantities, (d) EIS	69
Figure 3.8	(a) CV, (b) log (i) vs. log (v), (c) GCD, (d) C _{sp} values, (e) capacitive contribution, (f) stability & coulombic efficiency	70
Figure 3.9	(a) CV of MXene and B-GC@CPP-4 at 40 mV s ⁻¹ (b) CV and (c) GCD curves of ASC device (d) C _{sp} values at different current densities.	71
Figure 3.10	(a) Cyclic stability of the ASCs, (b) Ragone of the ASC device. (c) EIS of the ASC before and after stability	72
Figure 3.11	(a) GCD profiles of the ASC before and after 10,000 th cycle, SEM image of B-GC@CPP-4 along-with acetylene black and PVDF (b) before cycling (c) after cycling.	73

Figure No.	Caption	Page No.
Figure 4.1	1 (a) Powder XRD pattern (b) Raman spectra of Pristine Mn-HPO and Mn-HPO/RGO-10 hybrid, (c) crystal structure of Mn-HPO based on ICSD-75269.	88
Figure 4.2	XPS survey spectrum of Mn-HPO/RGO hybrid	89
Figure 4.3	Core level XPS spectra of (a) Mn 2p, (b) P 2p, (c) O 1s and (d) C 1s.	90
Figure 4.4	(a) & (b) FESEM image of Mn-HPO, (c) & (d) FESEM image of Mn-HPO/RGO-10, (e) EDX-mapped distribution of Mn, P, O, C in Mn-HPO/RGO-10	91
Figure 4.5	EDX spectrum of the Mn-HPO/RGO hybrid with atomic percentage of elements	92
Figure 4.6	(a) and (b) Low-resolution TEM image of Mn-HPO/RGO-10, (c) HRTEM image showing the nanoparticles of Mn-HPO, (d) fringe width of Mn-HPO in Mn-HPO/RGO-10	92
Figure 4.7	CV curves at 5 mV/s and GCD curves at 1 A/g for Mn-HPO/RGO-5, Mn-HPO/RGO-10 and Mn-HPO/RGO-20.	93
Figure 4.8	(a) CV profiles of Mn-HPO, (b) CV profiles of Mn-HPO/RGO-10 hybrid. (c) $\log(i)$ vs. $\log(v)$. (d) Percentage of the surface and diffusion-controlled process.	95
Figure 4.9	(a) GCD profile of Mn-HPO, (b) GCD profile of Mn-HPO/RGO-10, (c) C_{sp} vs. current density (d) coulombic efficiency and cycling stability of the Mn-HPO/RGO-10, (e) EIS of the Mn-HPO and Mn-HPO/RGO-10	96
Figure 4.10	(a) CV of Mn-HPO and MXene at 40 mV s^{-1} , (b) CV and (c) GCD curves of the ASC device. (d) C_{sp} of ASC device at various current density	98
Figure 4.11	(a) Stability and Coulombic efficiency of the ASC device, (b) Ragone plot showing the relation between Power density vs. Energy density	99
Figure 5.1	(a) PXRD pattern Pure $\text{Ti}_3\text{C}_2\text{T}_x$, SnO_2 and all the $\text{SnO}_2/\text{Ti}_3\text{C}_2\text{T}_x$ hybrids	112
Figure 5.2	(a) PXRD pattern of SnO_2 matching with PDF 00-021-1250, (b) PXRD pattern of MAX & MXene phase	112
Figure 5.3	Core level XPS spectra of (a) Ti 2p, (b) C 1s, (c) O 1s, (d) Sn 3d	113
Figure 5.4	Low and High Magnification FESEM Image of (a) and (b) SnO_2 , (c) and (d) $\text{Ti}_3\text{C}_2\text{T}_x$ 2D layers, (e) and (f) $\text{SnO}_2/\text{Ti}_3\text{C}_2\text{T}_x$ -80	114

Figure No.	Caption	Page No.
Figure 5.5	TEM and HRTEM image of (a) & (b) SnO ₂ , (c) & (d) Pristine Ti ₃ C ₂ T _x , (e) & (f) SnO ₂ /Ti ₃ C ₂ T _x -80 respectively	115
Figure 5.6	(a) CV curves of pristine SnO ₂ (b) mechanism of charge storage process, (c) GCD curves of pristine SnO ₂ , (d) C _{sp} vs. current density.	117
Figure 5.7	(a) CV at 5 mV/s and (b) GCD at 2 A/g for all the SnO ₂ /Ti ₃ C ₂ T _x hybrids (c) C _{sp} values of all the hybrids at 2 A/g (d) EIS of all the SnO ₂ /Ti ₃ C ₂ T _x hybrids	118
Figure 5.8	(a) CV curves of SnO ₂ /Ti ₃ C ₂ T _x -80, (b) charge storage mechanism determined by using power law, (c) percentage contribution towards total current calculated from CV profile, (d) GCD profiles of SnO ₂ /Ti ₃ C ₂ T _x -80, (e) specific capacitance vs. applied current density, (f) stability and coulombic efficiency after 10000 cycles of charge-discharge	120

LIST OF TABLES

Table No.	Caption	Page No
Table 2.1	OER performance comparison of GC-CPP with reported materials	50
Table 3.1	Comparison table for phosphate-based material showing supercapacitor behaviour	74
Table 4.1	Values of various parameters involved in EIS	97
Table 4.2	Comparison of supercapacitor performance of Mn-HPO/RGO with previous reports	99

LIST OF ABBREVIATION

PXRD	:	Powder X-ray Diffraction
XPS	:	X-ray Photoelectron Spectroscopy
TEM	:	Transmission Electron Microscopy
FE-SEM	:	Field Emission Scanning Electron Microscopy
HRTEM	:	High-Resolution Transmission Electron Microscopy
EDS	:	Energy-Dispersive X-ray Spectroscopy
EDAX	:	Energy Dispersive X-Ray Analysis
ICP-OES	:	Inductively Coupled Plasma - Optical Emission Spectrometry
CV	:	Cyclic Voltammogram
LSV	:	Linear-Sweep Voltammogram
PESI	:	Potentiostatic Impedance Spectra
GCD	:	Galvanostatic Charge Discharge
CP	:	Chronopotentiometry
CA	:	Chronoamperometry
TOF	:	Turn Over Frequency
ECSA	:	Electrochemically Accessible Surface Area
EDLC	:	Electrochemical Double Layer Capacitance
R_{CT}	:	Charge Transfer Resistance
R_s	:	Solution Resistance
FE	:	Faradaic Efficiency
C_{dl}	:	Double Layer Capacitance
h	:	Hours
min	:	Minute
GCE	:	Glassy Carbon Electrode
NF	:	Nickel foam

CHAPTER – 1

Electrochemical Energy Conversion through Water Splitting and Energy storage through Supercapacitors of Metal Phosphate and Oxide-based materials

A Brief Overview

1.1 Introduction

1.2 Electrochemical Cell

1.3 Water Splitting Reaction

1.3.1 Types of Water Splitting Reaction

1.4 Mechanism of Water Splitting Reaction

1.4.1 Mechanism for Hydrogen Evolution Reaction

1.4.2 Mechanism for Oxygen Evolution Reaction

1.5 Basic parameters involved to understand the water splitting process

1.5.1 Over potential

1.5.2 Tafel slope

1.5.3 Electrochemical active surface area

1.5.4 Electrochemical impedance spectroscopy

1.5.5 Turn over frequency

1.5.6 Faradaic efficiency

1.5.7 Cyclic stability

1.6 Materials used for Electrolysis process

1.6.1 Noble metal-based material

1.6.2 Carbon-based materials

1.6.3 Transition metal oxides and hydroxides

1.6.4 Transition metal phosphate-based materials

1.7 Supercapacitors

1.7.1 Components of a supercapacitor

1.7.2 Mechanism of supercapacitors based on electroactive material

1.7.2.1 Materials showing EDLC behaviour

1.7.2.2 Pseudocapacitive material

1.7.2.3 Hybrid capacitor

1.8 Basic parameters involved to understand the activity of supercapacitor

1.8.1 Specific capacitance

1.8.2 Energy density and power density

1.8.3 Electrochemical impedance spectroscopy

1.8.4 Cyclic stability and coulombic efficiency

1.9 Metal oxide and phosphate-based supercapacitors

1.10 References

1.1 Introduction

The rapid industrialization and population growth leads to increase in energy demand. However, environmental pollution and global warming caused by the overuse of traditional fossil fuels provoke researchers around the globe to search for clean and green renewable energy sources.^{1,2} The renewable energy sources such as nuclear energy has the drawback of bringing catastrophic disaster whereas, the intermittency of solar and wind energy limits their usage. In recent times hydrogen energy is the potential sustainable energy source but the evolution of hydrogen is mainly from natural gas via steam methanol reforming that again releases CO₂ as a by-product.³⁻⁵ On the other hand the most prevalent precursor for hydrogen production is water that surrounds the 70 % of the Earth's surface. Water electrolysis or water splitting reaction is carried out in an electrolytic cell. The electrolytic cell consists of two half-cell reactions, where at cathode hydrogen evolution reaction (HER) and at anode oxygen evolution reaction (OER) occurs. The electrolysis of water molecules requires, a theoretical potential of 1.23 V. But in actual use, a greater cell voltage is essential because of a number of internal and external factors, that reduces efficiency all around.⁶ Despite the fact that some noble metals, such as platinum, iridium, and rhodium, have demonstrated exceptional electrocatalytic activity, their precious metal status in terms of high cost and availability holds them back for large scale commercialization.⁷⁻¹¹ Therefore, in the last decade, numerous earth-abundant transition metal-based catalysts known as noble metal-free electrocatalyst (metal oxide/hydroxide, metal chalcogenides, and metal phosphate-based materials, etc.) have been investigated in order to make the manufacture of electrocatalysts economically viable.¹²⁻¹⁵

Energy storage systems are also necessary for the wise use of renewable energy sources. Now a days the energy storage system is a matter of debate as the renewable energy sources like wind, solar, tidal, etc. are used to generate electricity, are erratic and mostly reliant on the weather and environment. The commercial or domestic use of electricity requires a continuous and smooth flow, consequently calls for suitable storage devices to be coupled with these intermittent renewable energy sources. These storage systems would maintain the balance between energy supply and demand. The energy storage

systems such as batteries, supercapacitors and capacitors store electrical energy through electrochemical process and supplies them as required. The subsequent sections give us an elaborate idea on this energy conversion (water splitting) and energy storage (supercapacitors) systems.

1.2 Electrochemical Cell

A device that can either produce electrical energy from chemical reactions or use electrical energy to carry out a chemical reaction is called an electrochemical cell. Voltaic or galvanic cells are electrochemical devices that produce an electric current from chemical reaction, and electrolytic cells are devices that do chemical reactions by using electrical energy, such as electrolysis. This kind of electrochemical cell has a three-electrode configuration as presented in Figure 1.1,¹⁶ consisting of a counter electrode, a working electrode and a reference electrode. Despite the fact that the relevant electrodes are submerged in the electrolytes, some potential need to be provided to start the electrolysis process.

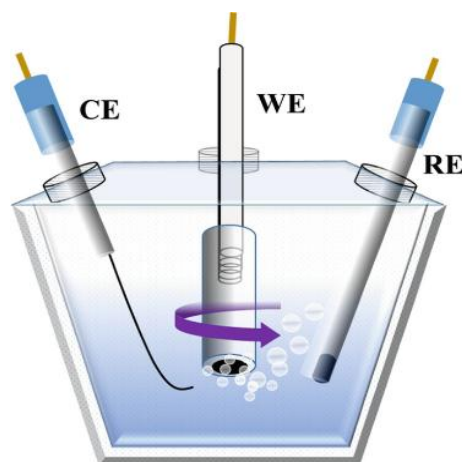


Figure 1.1 A typical three electrode set-up.¹⁶

1.3 Water splitting Reaction

Water is broken down into oxygen and hydrogen gas through a process called electrochemical water splitting, commonly referred to as electrolysis. This released hydrogen gas can be used as fuel to operate a fuel cell. Water is electrolyzed at a minimum applied potential of 1.23 volts and the overall water splitting reaction is presented as below in Figure 1.2.¹⁷

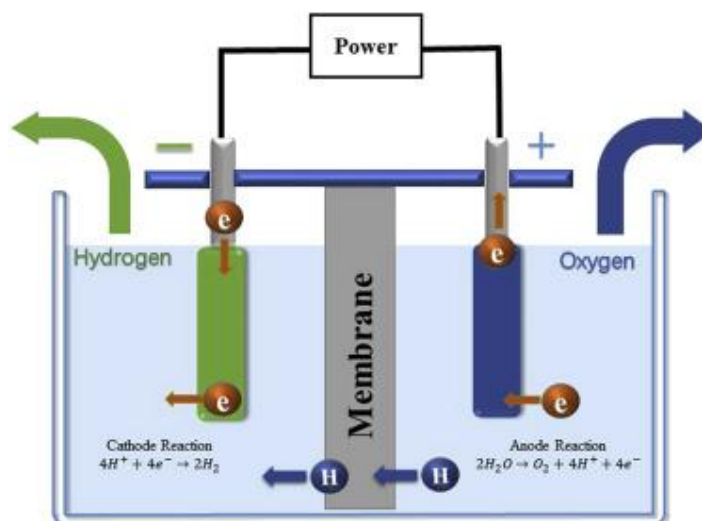
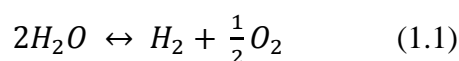


Figure 1.2 Two electrode system showing electrolysis process.¹⁷



For water electrolysis process the active material slurry is prepared by dispersing the active material in a mixed solvent of ethanol and nafion (as a binder) and sonicated to have a uniform dispersion of the active material. The working electrode is prepared by drop casting the homogenous dispersed slurry over a glassy carbon electrode (GCE) or any substrate such as stainless-steel mesh. Similarly, bare platinum rod is used as a counter electrode and Ag/AgCl or Hg/HgO reference electrode is used for complete electrochemical analysis.



Most often chlorine leaching occurs from chlorine containing reference electrode as mentioned in the above reaction, that further improves the catalytic activity of the electrode material. Thus, mercury-mercury oxide (Hg/HgO) type electrode is employed as reference electrode to evaluate the true catalytic performance of the electrode material. For each reference electrode, the obtained potential values for the evolution of renewable (H_2 or O_2) gases are calibrated into RHE (reversible hydrogen electrode) scale through the well-known Nernst equation through water splitting as follows:

For Ag/AgCl reference electrode:

$$E_{RHE} = E_{Ag/AgCl} + E^0_{Ag/AgCl} + 0.059 p^H; E^0_{Ag/AgCl} = 0.21 V$$

For saturated calomel electrode (SCE)

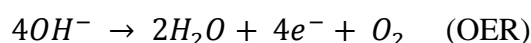
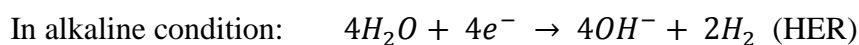
$$E_{RHE} = E_{SCE} + E^0_{SCE} + 0.059 p^H; E^0_{SCE} = 0.24 V$$

For Hg/HgO electrode,

$$E_{RHE} = E_{Hg/HgO} + E^0_{SCE} + 0.059 p^H; E^0_{Hg/HgO} = 0.897 V$$

1.3.1 Types of Water Splitting Reactions

Based upon the electrolytic condition and the presence of active ions the electrochemical water splitting is classified into two types, (i) HER (Hydrogen evolution reaction) and (ii) OER (Oxygen evolution reaction). In acidic media the active ion is H^+ whereas in alkaline media the active ions are OH^- .^{6,18} As presented in Figure 1.2 the hydrogen evolution reaction occurs in the cathode side whereas, in the anodic part oxygen evolution reaction takes place and the water splitting reaction in both acidic and alkaline media is presented below,



The energy required for the breakdown of water molecule for the evolution of hydrogen and oxygen is equivalent to the energy released during the process of formation of water. It is calculated using Gibbs free energy under the usual conditions of standard temperature and pressure.

$$\Delta G^0 = -nFE^0 \quad (1.3)$$

Where, ΔG^0 = Change in standard Gibb's free energy.

n = No. of electrons involved in the electrolysis process.

F = Faraday Constant (96,485 C)

The splitting of water into H_2 and O_2 molecules requires a thermodynamic potential of 1.23 V at standard condition of temperature (25 °C) and pressure (1 atm). However, in practice the sluggish reaction kinetics of water electrolysis requires more potential than that of thermodynamic potential for complete dissociation of water into molecular hydrogen and oxygen.¹⁹ The potential where the electrolysis process just starts is termed

as onset potential and the extra potential required for water electrolysis is called as overpotential.

1.4 Mechanism of Water Splitting Reaction

The water electrolysis process producing H_2 and O_2 is divided into two categories HER and OER respectively and the reaction mechanism of HER and OER both in acidic and alkaline medium are explained.

1.4.1 Mechanism of Hydrogen Evolution Reaction

In an electrolyser hydrogen evolution reaction (HER) occurs at the cathodic part where protons get adsorbed on the electroactive material to generate molecular hydrogen. This HER follows a two-electron transfer pathway and the mechanism depends upon the type of electrolytic condition (either acidic or alkaline).

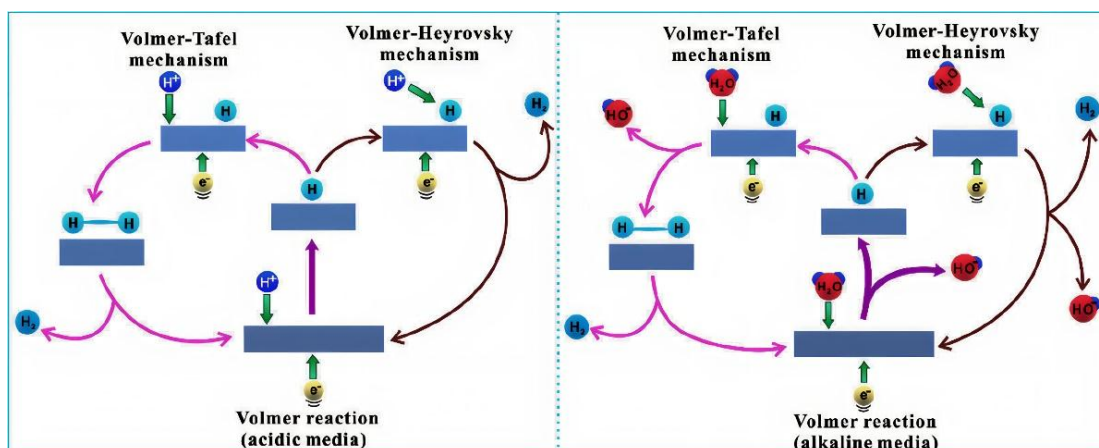


Figure 1.3 Mechanism of hydrogen evolution reaction in acidic and alkaline media.²⁰

In acidic condition HER follows of two steps, either Volmer-Heyrovsky or Volmer-Tafel. In the Volmer step the H^+ ion is adsorbed over the surface of the electrocatalyst and thus, forming an adsorbed hydrogen atom denoted as H_{ads} . After the Volmer step if the reaction goes through the Heyrovsky step, then another electron coupled hydronium ion (H^+) combines with the adsorbed hydrogen generating molecular hydrogen. Whereas, in Tafel step two adsorbed hydrogen atoms are combined forming a hydrogen molecule. The above Figure 1.3 represents the hydrogen evolution reaction.²⁰

In alkaline media, initially electron coupled water molecule discharges a hydroxide ion and hydronium ion. This hydronium ion (H^+) gets adsorbed onto the electroactive

material forming an adsorbed hydrogen H_{ads} species. The hydrogen atom that has been adsorbed then interacted with another electron coupled water molecule to create hydrogen gases in the Heyrovsky step. In the Tafel step, the combination of two H_{ads} atoms to produce H_2 molecule.

1.4.2 Mechanism of Oxygen Evolution Reaction

In the electrolyser the oxidation of water occurs at the anodic part producing O_2 molecule. It follows a four-electron transfer pathway to complete the oxygen evolution process through formation of various transient species (oxide/hydroxide/peroxide). The OER mechanism in both the acidic and alkaline condition is presented in Figure. 1.4.²¹

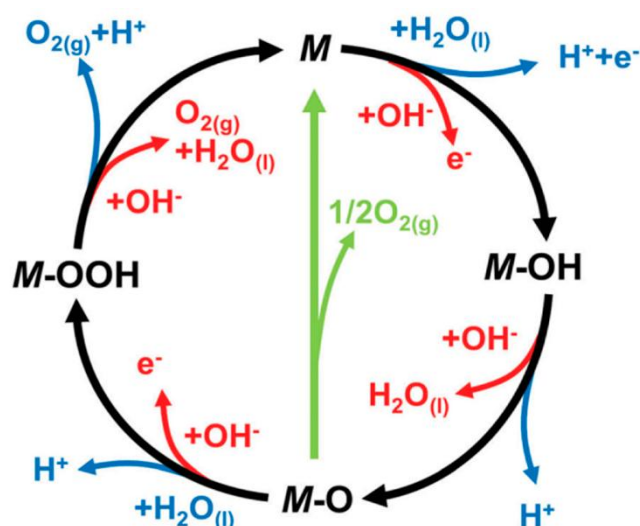


Figure 1.4 Mechanism of OER in both alkaline (red line) and acidic medium (blue line).²¹

Thermodynamically 1.23 V potential is required for the water oxidation but the involvement of these steps makes the kinetics of the process sluggish and hence requires a potential higher than that of thermodynamic one. In alkaline medium the OH^- ions are plentifully available in the electrolytic solution thus adsorbed on the catalytic surface forming a hydroxo species. Then one proton from these hydroxo species is removed by attack of another OH^- ion and forms oxo species. Later, this oxo species combines with another OH^- ion forming a peroxo species and finally this peroxo species attacked by another hydroxide ion and liberates molecular O_2 and water. Thus, it is inferred that four hydroxide molecules and four electrons are used for the formation of a O_2 molecule.

In acidic medium, the water molecule is dissociated into a proton, electron and a hydroxide ion. This hydroxide ion gets adsorbed on the catalyst surface forming hydroxo species and a hydrogen ion is liberated from this forming a metal oxide species. Further another water molecule provides a hydroxide ion by removing a proton and an electron forming a peroxy species. At last, this peroxy species generates a molecular oxygen and a hydronium ion. From this mechanism it is clear that in acidic medium two molecules of water are used to produce a molecular O₂, four electrons and protons.^{22,23} The formation and decomposition of the M-O and M-OOH bond is the sole responsible for the catalytic performance of the active material.^{24,25}

1.5 Basic parameters involved to understand the water splitting process

The electrochemical parameters involved to understand the water splitting process are overpotential, Tafel slope, Nyquist plots, electrochemical active surface area (ECSA) with roughness factor or active sites, mass activity, turn over frequency, faradaic efficiency, and cyclic stability. The reaction mechanism involved in the catalysis process can also be inferred from these mentioned parameters.

1.5.1 Overpotential

Thermodynamically, it requires 1.23 V of potential for OER at anodic counterpart and 0.0 V for HER at cathodic counterpart. However, the practical realisation of water electrolysis reveals that some extra amount of potential is required to overcome the kinetic barrier associated with these reactions (HER and OER). This extra amount of potential with respect to that of thermodynamic potential is termed as overpotential. Thus, the electroactive material showing lesser overpotential value is the main focus of the researchers around the globe. There exist three major factors that increase the gap between thermodynamic potential and experimental potential and accordingly overpotential is classified into three types such as, (i) Activation overpotential, (ii) Concentration overpotential, (iii) the overpotential arising due to the ohmic drop.¹⁹ Activation overpotential is an intrinsic property of the electrode material and can be removed by employing suitable electrocatalyst. The slower rate of charge carrier diffusion at the electrode/electrolyte interface leads to concentration overpotential and can be excluded by constant stirring of the electrolyte solution. Similarly, the overpotential caused by the ohmic drop can be eliminated by iR correction. This ohmic drop (iR) correction can be carried out by multiplying the solution resistance with the

current density obtained from electrochemical impedance spectroscopy and linear sweep voltammetry respectively. This iR value is then further subtracted from the experimentally observed potential to get the intrinsic catalytic activity of the electrocatalyst towards HER/OER.^{26,27} The overpotential is a relative quantity and to achieve a current density of 10 mA/cm^2 the required potential shows the efficacy of the catalyst. This current density value of 10 mA/cm^2 is the obtained current at 1 sun illumination from a solar cell device having 12.3 % efficiency. Hence, lower the overpotential value to achieve this current density higher is the efficiency of the electrocatalyst.

1.5.2 Tafel Slope

The Tafel slope provides an idea on the surface kinetics and reaction mechanism throughout the HER/OER process. The increased efficiency of HER or OER catalyst is shown by an electrocatalyst's lower Tafel slope value, which increases cathodic/anodic current density at a lower overpotential. Typically, the Tafel slope is generated from the Tafel plot's fitted linear region. A profile of the current density $\log(j)$ versus overpotential (η) is used to show the Tafel plot. While the following equation is used to establish the relationship between $\log(j)$ and overpotential (η).^{28,29}

$$\eta = a + b \log(j) \quad (1.4)$$

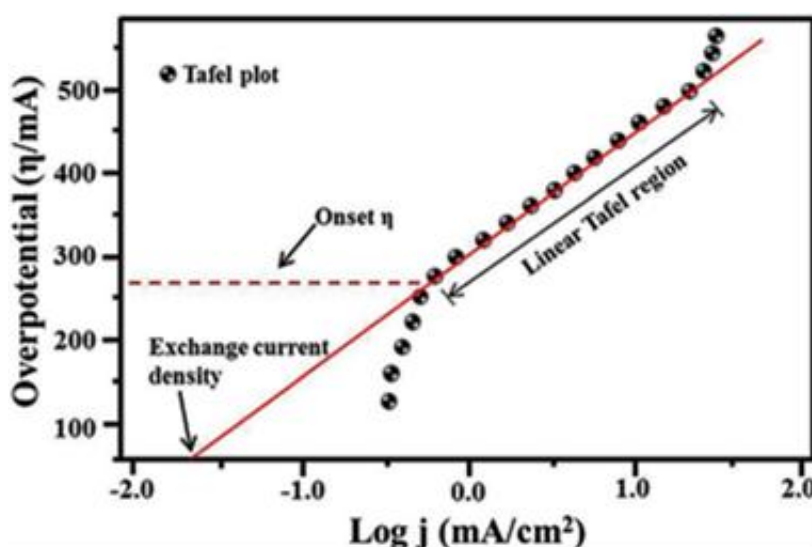


Figure 1.5 Graphical representation of Tafel plot showing linear Tafel region and Exchange current density.¹⁶

In the above equation η is the overpotential, a & b are Tafel constants and j is the current density. Furthermore, the extrapolated Tafel plot intersects X-axis at a particular point and that gives the exchange current density (j_0) value. Higher the value of j_0 suggests the presence of higher number of active sites on the catalyst surface. The Figure 1.5 represents a linear region of Tafel plot and exchange current density value.¹⁶

1.5.3 Electrochemical Active Surface Area (ECSA)

Unlike specific surface area obtained from BET analysis, ECSA provides us an idea of electrochemically active surface area of the catalyst. By extrapolating double-layer capacitance (C_{dl}) from a non-faradic portion of a cyclic voltammetry curve, the ECSA value can be determined. The electrocatalyst's extremely rough and porous surface has a significant impact on the ECSA value. The charge accumulation process corresponding to a charge of layers at the electrode/electrolyte interface without any redox behaviour is the only factor used to estimate the double-layer capacitance. The current (i) in a CV curve increases gradually with increase in the scan rate (v) and the double layer capacitance can be calculated from the equation below,^{30,31}

$$i = vC_{dl} \quad (1.5)$$

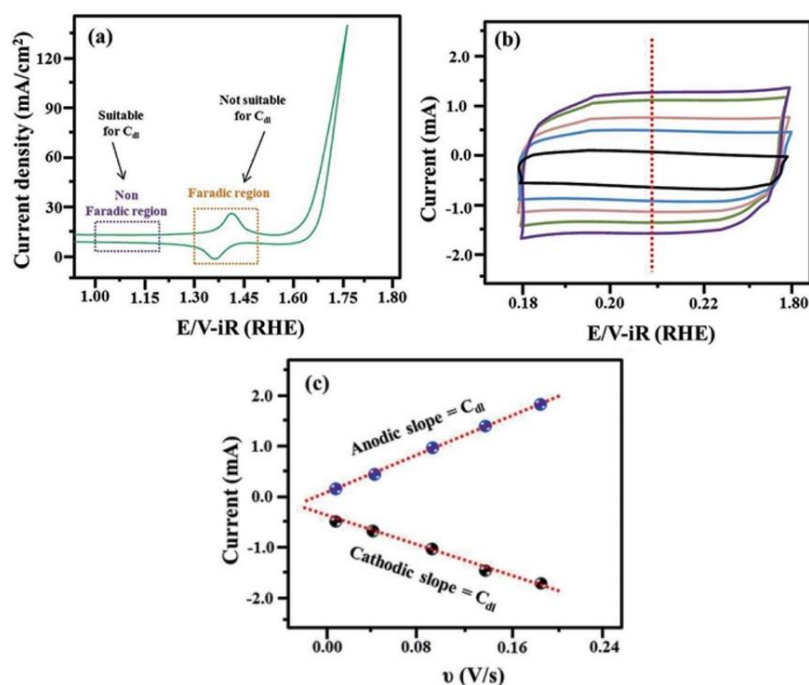


Figure 1.6 (a) CV curve showing Faradaic and non-Faradaic region, (b) Enlarged CV curves in non-Faradaic region, (c) Cathodic and Anodic slope to evaluate C_{dl} .¹⁶

The C_{dl} value is evaluated by plotting a graph between current (i) vs. sweep rate (v) at a particular potential, where the slope of the obtained curve provides the value of C_{dl} .

This observed value of C_{dl} is further employed to evaluate ECSA through following equation,

$$ECSA = \frac{C_{dl}}{C_s} \quad (1.6)$$

C_s is the specific capacitance of atomically smooth catalyst surface and its value is 0.04 mF in alkaline medium and 0.35 mF in acidic medium.^{32–34} Moreover, roughness factor (R_f) is a term that signifies the presence of active sites per unit surface area and evaluated by dividing ECSA with the geometrical surface area of the electrode. The non-Faradaic region of the CV curve and the cathodic and anodic slope is mentioned in Figure 1.6.¹⁶

$$R_f = \frac{ECSA}{S_{geo}} \quad (1.7)$$

1.5.4 Electrochemical Impedance Spectroscopy (EIS)

The solution resistance, charge transfer resistance and mass transfer activity of an electrocatalyst can be investigated by EIS measurements through Nyquist plot analysis. Nyquist plot is a plot between imaginary axis (Z'') vs. real axis (Z'). This Nyquist plot can be obtained by varying the AC-frequency from higher to lower value at a particular potential and amplitude. Impedance is a kind of resistance that either complies with or violates Ohm's law. Each point in the Nyquist plot depicts a certain frequency and provides details about different electronic elements involved in the electrochemical reactions, such as solution resistance, charge transfer resistance, and double-layer capacitance. The combination of the resistance of electrolytic ions, resistance of the electrode and the existing contact resistance between the electrode and active material interface is known as solution resistance.³⁵ Experimentally, R_s is the interception of the Nyquist plot with the real axis (Z') provides the equivalent series resistance ($Z' = R_s, Z'' = 0$) in the Nyquist plot's higher frequency region. Similarly, the R_{ct} (charge transfer resistance) value is determined from the radius of the semicircle from the Nyquist plot.³⁶ Lower the R_{ct} value better is the electrochemical performance of the electrocatalyst as mentioned in the Figure 1.7.³⁷

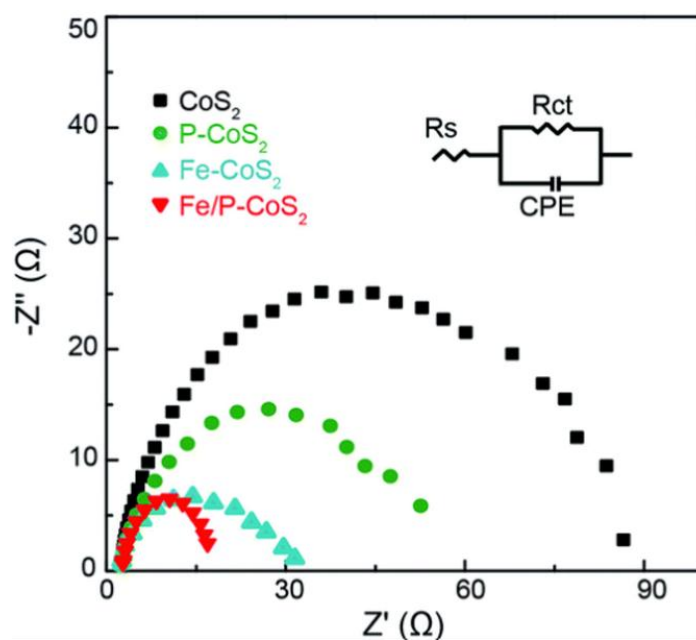


Figure 1.7 Nyquist plot of pristine and Fe/P dual doping CoS₂ polycrystalline nanowire for HER showing EIS.³⁷

The energy storage performance of the electroactive material can be further evaluated from EIS measurements using the following equation,^{38,39}

$$C = \frac{1}{m \times j \times 2\pi f \times Z''} \quad (1.8)$$

Where C , m , j , f , Z'' are the specific capacitance, mass of the active material, frequency and the imaginary part of the impedance test respectively.

1.5.5 Turn over frequency

An electrocatalyst's turnover frequency provides a thorough analysis of the evolution of the number of moles of H₂ or O₂ molecules per unit time.^{40,41} Nonetheless, the following equations can be used to obtain the value of turn over frequency:

$$TOF = \frac{\text{Number of H}_2 \text{ or O}_2 \text{ evolved per unit time}}{\text{Number of active sites}} \quad (1.9)$$

$$\text{Or } TOF = \frac{IN_A}{AF_n\tau} \quad (1.10)$$

Where current, Avogadro's number, geometrical surface area, Faraday constant, no. of electrons is denoted as I , N_A , A , F and n respectively along with τ as the symbol of surface. Two electrons are involved in HER process whereas, four electrons are involved during OER process. Thus, the TOF for HER and OER is expressed as below¹⁶

$$(TOF)_{HER} = \frac{1}{2F_n} \quad (1.11)$$

$$(TOF)_{OER} = \frac{1}{4F_n} \quad (1.12)$$

1.5.6 Faradaic Efficiency

A crucial criterion for evaluating the effectiveness and the ratio of supplied to consumed electrons in an electrochemical reaction is called faradic efficiency. However, in HER/OER, the Faradic efficiency compares the actual amount of hydrogen or oxygen molecules detected to the expected amount of hydrogen and oxygen molecules.^{26,42}

The equation below is used to evaluate the value of Faradaic efficiency

$$\text{Faradaic efficiency} = \frac{I_R \times n_D}{I_D \times n_R \times N_{CL}} \quad (1.13)$$

The ring and disc currents, are identified as I_R and I_D in the equation above, respectively. In the electrochemical analysis as a whole, countable electrons are represented by n_D and n_R .

1.5.7 Cyclic Stability

Similar to that, several active parameters were measured for durability or cyclic stability using chronopotentiometry (change in overpotential seen at sustained current densities of at least 10 mA/cm²). Also, the chronoamperometric approach analyses the observed consistency performances and practical application of the as-prepared active electrode material (at a specific overpotential change in current density). The stability tests, however, were also carried out by repeatedly running the CV cycle between the set potential range at a certain scan value. An electrocatalyst's polarisation curve is typically recorded after a stability test and compared to data from before the test to look for any changes in overpotential that can indicate poor electrochemical performance. In order to establish the effectiveness of the as-prepared active material after continuous electrochemical analysis, additional shifts in the diffraction pattern (phase purity), surface morphology, and elemental composition (XPS spectra) were investigated. Figure 1.8 suggests the long term stability test for GC-CPP sample at 10 mA/cm².⁴³

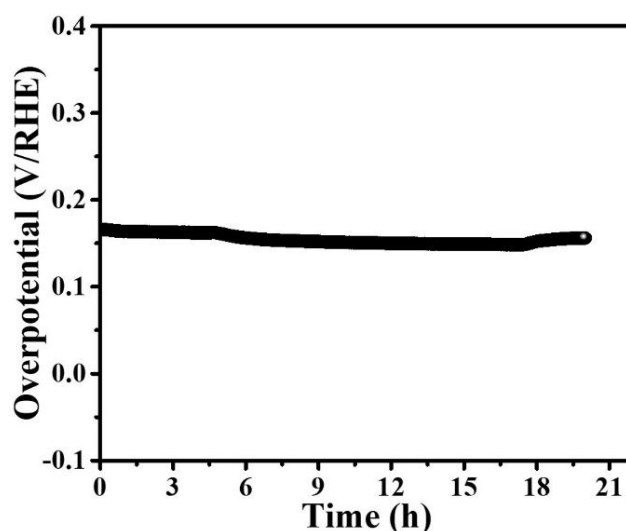


Figure 1.8 long-term stability at 10 mA/cm² current density for graphitized carbon cobalt pyrophosphate (GC-CPP).⁴³

1.6 Materials used for electrolysis process

The different precious and non-precious metals have a significant impact on the electrocatalytic evolution of renewable hydrogen/oxygen molecules. The benchmark catalysts for the electrocatalysis process are noble metals like platinum (Pt) or palladium (Pd), as well as other precious metal oxide-based materials like ruthenium (RuO₂) and iridium oxide (IrO₂). Several more non-precious metal and non-metal based electrocatalysts are used to replace the noble metal-based catalyst in addition to this precious metal-based catalyst. These days, efficient HER/OER electrocatalysts without noble metals have been synthesized by using a variety of novel synthetic processes, and their catalytic activity is analysed and compared with noble metal based electrocatalyst.

1.6.1 Noble metal-based materials

According to the theoretical research, the two- and four-electron reaction mechanisms must operate with the thermodynamic potential of 0 V and 1.23 V (against RHE) in order to produce molecular hydrogen and oxygen gases from the water electrolysis. In order to split the water through electrocatalytic process, requires a high value of overpotential. In general, the noble metals like platinum (Pt), palladium (Pd), oxide of ruthenium (RuO₂), and oxide of iridium (IrO₂) lower the high value of additional potential (overpotential).²⁵ Figure 1.9 displays a profile of the precious metal's HER

activity in terms of free energy change. The benchmark catalyst for the HER process is platinum (Pt) and to achieve a generally recognised current density of 10 mA/cm^2 (as a standard current density value), a lower value of extra potential is needed. Similarly, the oxygen evolution reaction (OER) uses both ruthenium (RuO_2) and iridium oxide (IrO_2) as the reference electrocatalyst in order to increase the activity of oxygen evolution in the supporting electrolytes. Unfortunately, the numerous practical uses are restricted due to its high cost, very less abundancy, and low electrochemical stability.

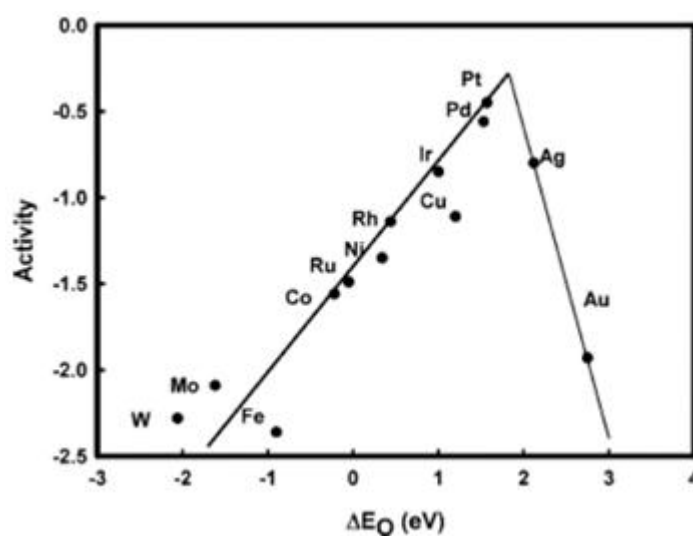


Figure 1.9 For HER activity of electrocatalyst vs. calculated Gibb's free energy.⁴⁴

Thus, researchers putting much effort for the development of electrocatalyst free of noble metal, that can show better electrochemical performance than that of noble metal-based catalyst. Except the better electrochemical performance of non-noble metal-based catalyst, the low cost and high durability is advantageous over the noble-metal based catalyst. Looking into these advantages the pristine and carbon-based hybrids of metal oxide/hydroxide, and metal phosphates as electroactive materials are attractive choice for electrocatalytic applications. Figure 1.9 depicts the HER electrocatalytic activity vs. Gibb's free energy.⁴⁴

1.6.2 Carbon based materials

Activated carbon,^{45–47} carbon nanotubes,⁴⁸ carbon nanofibers,⁴⁹ hetero atom doped carbon,⁵⁰ and carbon aerogels⁵¹ are used as templates or hybrid materials to improve the storage performances and catalytic activity in both the field of energy storage and conversion application. The carbon-based electrode material having 2D layered

analogous corresponding to pristine graphene.⁵² Despite the fact that 2D graphene material is gaining popularity due to its low cost, great natural abundance, superior surface-to-volume ratio, good electrical conductivity, elevated thermal and chemical stability, and ability to operate in a wide temperature range, a material created by functionalizing the surfaces of carbon nanotubes, helps to improve electrocatalytic (HER/OER) and energy storage performances. Beside other carbonaceous materials, the surface functionalized carbon nanotubes improve the electrocatalytic (HER/OER) and storage performance (Supercapacitor) by adjusting pore size, pore volume, and nanostructures. Carbon nanotubes (CNTs) are classified into two types; single walled CNT and multiwalled CNT. Single walled CNT (SWCNT) is formed by wrapping single 2D graphene sheet into cylindrical form thus forming SWCNT, when multiple graphene sheets are wrapped in a cylindrical format produces MWCNTs. CNTs with no edge plane can prevent the irreversible electrochemical reaction to happen.⁵³ Apart from graphene, CNTs are an effective composite material for studying energy conversion and storage because of these distinctive features. However, these carbonaceous materials have certain limitations to hybrids with pseudo material for demonstrating higher HER/OER performances due to the presence of limited accessible surface area and EDLC behaviour.⁵³ In the absence of any hybrids of redox-active material, the hydrogen evolution reaction of pure RGO films was determined from the measured polarisation curve. Doping improves graphene's HER performance over unaltered graphene. Compared to bare graphite and single-doped graphene electrode materials, the dual-doped (N, P) graphene exhibits greater HER activity. Compared to other electrode materials, it required just 420 mV of extra potential to obtain a predetermined current density of 10 mA/cm² with a lower Tafel slope value.⁵⁴ Like graphene, MWCNTs also exhibit poor electrocatalytic activity in the absence of hybridization or doping.⁵⁵

1.6.3 Transition metal oxides and hydroxides

Metal oxide and hydroxide's semiconducting properties make them a strong choice for the HER/OER process and energy storage performance towards supercapacitors (SCs). Non-precious metal hydroxide or oxide has the advantages of a variable oxidation state, greater electrochemical stability, and an electrically conductive character, suggesting a suitable choice for the energy industries.⁵⁶ For improved electrocatalytic performance in the direction of the oxygen evolution reaction, the noble metal oxides of ruthenium

(RuO₂) and iridium (IrO₂) are utilised as standard electrode materials (OER).¹⁰ But its high cost and restricted supply drive our hunt for a noble metal-free electrocatalyst. Surprisingly, Co₃O₄, NiO, and MnO₂ non-precious metal oxides were investigated and taken into consideration as anode materials for overall water splitting. The OER activity for NiO nanofibers was detected in lower overpotential of 322 mV to obtain a standard current density of 10 mA/cm² was reported by Silva et al.⁵⁷ The higher oxygen evolution performances of Co_{3-x}O₄ were also explored, with a lower overpotential of 268 mV and a Tafel value of 38.2 mV/dec, respectively.⁵⁸ In addition to these, the 1D NiCo₂O₄/graphene hybrids' binary metal oxide exhibits superior OER and supercapacitor capabilities. To supply the predetermined current density of 10 mA/cm², the modest overpotential value of 313 mV with a lower Tafel value of 35 mV/dec is required.¹³

1.6.4 Transition metal phosphate-based materials

The water electrolysis process is the combination of HER and OER. Among which the OER process mediate through four electron and four proton transfer pathway making the reaction kinetics sluggish.⁵⁹ Thus, plenty of research work is going on to develop an electrocatalyst that reduces the electric potential required for this half-cell reaction. Noble metal-based catalyst such as Ru and Ir shows efficient catalytic performance but the broad application is inhibited due to its high cost and scarcity.⁶⁰ Whereas, non-noble metal (Fe, Ni, Co) based electrocatalysts having large scale production and low cost suggests its wide spread application. Among them Co-based materials show superior electrocatalytic activity compared to other non-noble metals.⁶¹ Till date various cobalt based materials are reported such as oxides, chalcogenides, nitrides, phosphates, among these cobalt phosphates are of prime interest due to its self-healing property and mild working condition.⁶² Particularly, phosphate-based cobalt nano-structures are in the limelight after the novel work by Nocera and Kanan in 2008.⁶³ Pramanik et.al. synthesized ordered mesoporous cobalt phosphate with crystallized wall delivers an overpotential of 380 mV to achieve a current density of 10 mA/cm² with a Tafel slope of 58.7 mV/dec.⁶⁴ Similarly, pyrophosphates are class of phosphates where two phosphate units share one oxygen atom forming a butterfly type of geometry.⁶⁵ Cobalt pyrophosphate with layered structure shows better magnetic, optical and electrical properties. These unique properties of cobalt pyrophosphates are better than that of cobalt phosphates by virtue of its physicochemical structure.⁶⁶ Du et.al. synthesized a

range of cobalt pyrophosphate nanostructures among which cobalt pyrophosphate nanowires projects an overpotential value of 359 mV at 10 mA/cm² and shows a Tafel slope value of 54.1 mV/dec.⁶⁷ Moreover, through a co-precipitation method, Liu et al. have prepared Co–Fe pyrophosphate and employed it as electrocatalyst for the OER. It catalyses the OER efficiently requiring only 276 mV of overpotential to reach a 10 mA/cm² current density.⁶⁸ In a recent work, carbon-coated cobalt iron pyrophosphates (NCFPO/C NPs) were synthesized via a sol–gel method. The NCFPO/C NPs were found to catalyse the OER showing a lower overpotential of 300 mV to deliver state-of-the-art current density compared to that reported before.⁶⁹ Although several works have been carried out based upon cobalt phosphate and pyrophosphate-based material still much focus need to be poured to achieve still lower overpotential value with high durability.

1.7 Supercapacitors

The gradual increment in the energy demand and rapid industrialization along with growth of population leads to economic and environmental crisis throughout the globe. Thus, scientists around the globe are running behind the development of clean and green energy sources. Most of the renewable energy sources are of intermittent in nature and to avoid this intermittency a successful energy storage device with long cycle life is of prime importance. Supercapacitors (SCs) is a kind of storage system that act as a bridge between batteries and dielectric capacitors, are responsible for delivering energy at higher rates along with retaining specific power for long time. Supercapacitors are also termed as electrochemical capacitors having same type of cell construction as that of dielectric capacitors. In which the metal electrodes are substituted with porous electrode material with high specific surface area and the dielectric material is replaced with suitable electrolyte to selectively pass the ions. This efficient energy storage device supercapacitors can be employed in a broad range of applications, such as portable electronics, electric or hybrid electric vehicles, and smart grids. However, the lower energy density of supercapacitors compared to batteries and fuel cells, is the major drawback need to be focused. Thus, research communities are tirelessly working to improve the energy density of supercapacitors by developing new and efficient electroactive material or by employing different electrolytes. Furthermore, by tuning various components of the supercapacitors can also enhance the supercapacitor performance.

1.7.1 Components of supercapacitor

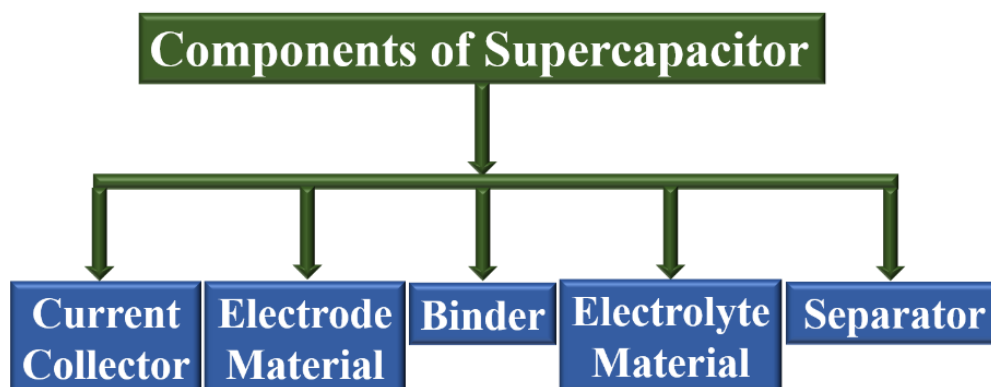


Figure 1.10 Various components of a supercapacitor device.

As presented in Figure 1.10, a typical supercapacitor comprises of five components. A supercapacitor device consists two electrode material (positive and negative) with binder coated over respective current collector. These two electrodes are then separated by an ion-permeable membrane called as separator and an electrolyte. The separator not only behaves as an insulator to avoid short-circuit but also allows the charge-carriers pass through it. Although all these components can affect the electrochemical performance of a supercapacitor, tuning the electrode material to enhance capacitive behaviour of the supercapacitor is our prime focus.

1.7.2 Mechanism of supercapacitors based on electroactive material

Based upon the electrode material the mechanism of the supercapacitors is classified into various types such as (i) Materials showing Electric double layer capacitors (EDLC), (ii) Materials showing Pseudocapacitive behaviour, (iii) Hybrid capacitors.

1.7.2.1 Materials showing EDLC behaviour

Capacitors of the electric double layer (EDL) follows non-faradic reactions. The process by which charge and energy are stored is entirely electrostatic. The idea of an electric double layer refers to the formation of two layers of opposing charge on two interfaces separated by a molecular dielectric at the smallest possible distance. Ion movements or charge accumulation occur on the corresponding electrode with the opposing charge as the voltage is applied. To create an ion-rich environment, an electrolyte is employed. The earliest theoretical representation of the EDL-type

capacitor was put forth by Helmholtz in the 19th century. The inner and outer layers of the Helmholtz plane are formed by the charge accumulation process, which occurs between the surface of the current collector and the electrolyte as presented in Figure 1.11.⁷⁰ The storing of electric charge is directly proportional to the voltage applied in the EDL system. In general, the carbon-based electrode materials (e.g., graphene, activated carbon, carbon nanotubes, etc.) show this type of mechanism as presented in Figure 1.12.⁷¹

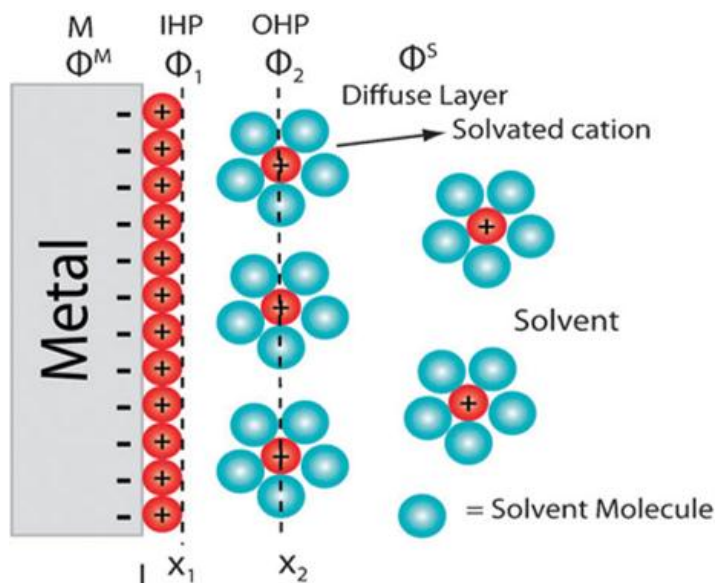


Figure 1.11 Helmholtz model for the electrical double-layers.⁷⁰

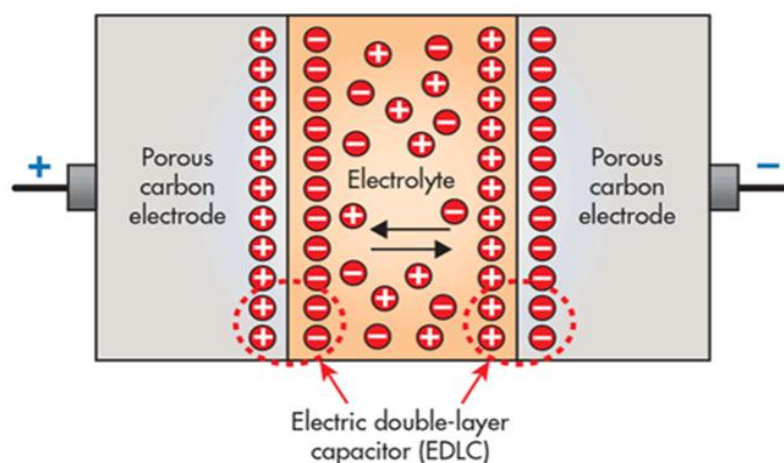


Figure 1.12 Schematic representation showing EDL capacitor.⁷¹

1.7.2.2 Pseudocapacitive Material

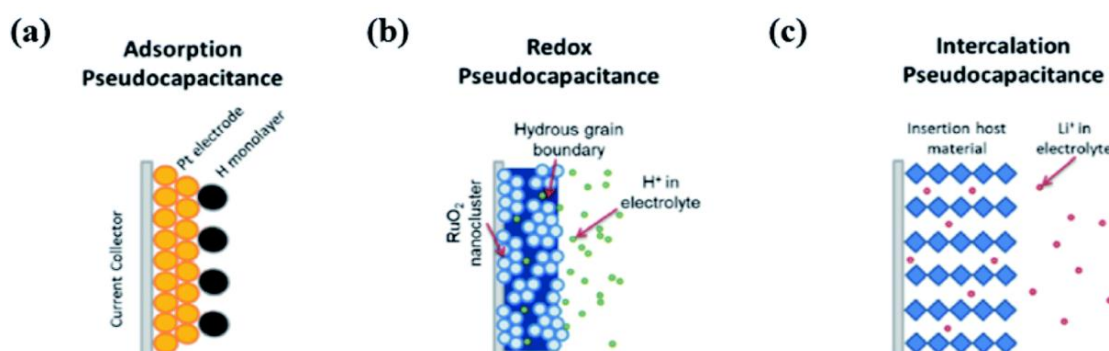


Figure 1.13 Representation of various pseudocapacitive process.⁷⁴

Although there is a tremendous progress in carbonaceous material as EDLC, their lower value of energy density limits its usage in portable electronics and electric vehicle. Unlike EDLC, pseudocapacitors store charge through fast redox process at the surface or near surface of the electrode materials. Based upon faradaic reactions the pseudocapacitive electrode material is categorized into following types such as (i) underpotential deposition, (ii) surface redox pseudocapacitance, (iii) intercalation pseudocapacitance.^{72,73} In case of underpotential deposition is also known as adsorption pseudocapacitance, where a monolayer of metal ions is formed on different types of metal (Ru, Pt, Au and Rh) surfaces due to faradaic adsorption and desorption process as shown in Figure 1.13 (a).⁷⁴ Surface redox pseudocapacitors presented in Figure 1.13 (b) follows a charge transfer process where ions get electrochemically adsorbed onto the or near the surface of electrode material. Redox pseudocapacitance for charge storage is exhibited by a variety of electroactive materials, including conducting polymers like polypyrrole and polyaniline, transition metal oxides like MnO₂ and RuO₂.^{75–77} Similar to other pseudocapacitor charge-transfer mechanism, intercalation pseudocapacitance depicted in Figure 1.13 (c) occurs when ions are reversibly intercalated into and deintercalated from the tunnels or layers of a redox-active material without going through any crystallographic phase change. The majority of electroactive substances in organic electrolytes display intercalation-based pseudocapacitance, including nanostructured TiO₂, Nb₂O₅, and MoO₃.⁷⁸ Due to their distinctive physical processes and various electroactive materials, these three distinct pseudocapacitive mechanisms manifest at the electrode surface. Yet, because of their poor electrical conductivity and low power density, pseudocapacitors usually have short cycle lives.^{79,80}

1.7.2.3 Hybrid capacitor

Combining both the non-faradaic EDLC and faradic pseudocapacitor charge storage methods, hybrid SCs operate on a similar premise. In order to achieve higher electrochemical performance or charge storage performance, a hybrid supercapacitor can attempt to exploit the relative advantages and minimize the respective shortcomings of EDLCs and pseudocapacitors. Compared to EDLCs and pseudocapacitors, hybrid SCs have more energy and power density without sacrificing cycling stability or rate capabilities. The hybrid SCs can be categorised into three groups based on electrode configuration: (i) asymmetric hybrids, (ii) battery-type hybrids, and (iii) composite hybrids.

In order to increase the energy density of the supercapacitor, an asymmetric hybrid supercapacitor can be created by combining an EDLC electrode (typically negative electrode) with a pseudocapacitive electrode (typically positive electrode), which can operate up to a higher potential window than normal symmetric SCs.⁸¹ A different form of energy storage technology that can bridge the energy and power densities of batteries and SCs is the battery-type hybrid supercapacitor. By combining battery-type and capacitive-type electrode materials, the battery-type hybrid supercapacitor improves the overall electrochemical energy performance.^{82,83} By combining carbonaceous materials (EDLC) with pseudocapacitive substances including transition metal oxides, hydroxides, chalcogenides, and conducting polymers, which combine both physical and chemical charge storage mechanisms in a single electrode, composite hybrid SCs can be created. Due to the synergistic interaction of the EDLC and pseudocapacitive charge storage mechanisms, the composite hybrid supercapacitor device exhibits superior electrochemical performance than the parent or bare supercapacitor device.^{84,85}

1.8 Basic parameters involved to understand the activity of supercapacitor

The conventional parameters of specific capacitance or charge storage performance, energy density, power density, and cyclic stability with columbic efficiency are used to assess the supercapacitor performance.

1.8.1 Specific capacitance

The amount of charge stored with a potential change determines the specific capacitance, or C_s , of an electro-active material in its as-prepared state. Also, the

measured capacitance was converted into areal capacitance (F/cm²) for areas and gravimetric capacitance (F/g) for masses, respectively. A mass of sample loaded on the electrode surface, separator, the presence of the electrolytic medium, the thickness, and the dimension of the active material are utilised to monitor the value of specific capacitance for different electrode materials. Both the galvanostatic charge-discharge procedure and the cyclic voltammetry approach have been used to calculate the value of specific capacitance (C_s).⁸⁶ The following equation 1.14 and 1.15 is used to further evaluate the specific capacitance from CV and GCD.^{87,88}

$$C_{sp} = \frac{\int I dV}{[m v (\Delta V)]} \quad (1.14)$$

The above equation is used to calculate the specific capacitance of the electroactive material by using the CV curves. Here, $\int I dV$ is the area under the CV curve, m is the mass of the active material, v is the scan rate and (ΔV) is the operating potential window.

$$C_{sp} = \frac{I \Delta t}{m \Delta V} \quad (1.15)$$

In the above equation I signifies the discharge current, m is the mass of active material, Δt is the discharge time and ΔV is the working potential window.

1.8.2 Energy density and power density

The performance of a supercapacitor can be further defined by two key factors: specific energy or energy density and specific power or power density. With the help of galvanostatic charge-discharge (GCD) techniques, the specific energy and specific power measurements can be carried out by using equation 1.16.^{89,90} The following equation 1.17 was used to calculate the specific power or power density from the GCD data.³⁵ Here, E.D. and P.D. stand for, respectively, energy density (Wh kg⁻¹) and power density (W kg⁻¹). C_{sp} stands for the particular capacitance, V stands for the designated potential window, and v is the scan rate.

$$E. D. = \frac{1}{2} [C_{sp} \times (\Delta V)^2] \quad (1.16)$$

$$P. D. = \frac{E.D. \times 3600}{\Delta t} \quad (1.17)$$

1.8.3 Electrochemical Impedance spectroscopy

The intrinsic parameter of the altered electrode material and the electrolytes are examined using the electrochemical impedance spectrum. Notably, from the impedance spectroscopy analysis equivalent series resistance, charge transfer resistance and Warburg coefficient is evaluated. In an electrolyte solution, the graph typically depicts the imaginary component (Z'') vs the real part (Z'). The equivalent series resistance is the combination of ionic resistance of the electrolyte, inherent resistance of the electroactive material and the contact resistance of active material and current collector. The charge transfer resistance is depicted by the graph's semi-circle area. With a reduction in charge transfer resistance, an active material's specific power or power density rises. The 45° phase angle from the semicircle zone accounts for the ion diffusion that is seen in the Warburg impedance region.⁹¹ The EIS of cobalt nickel phosphate with different ratios is presented in Figure 1.14.⁹²

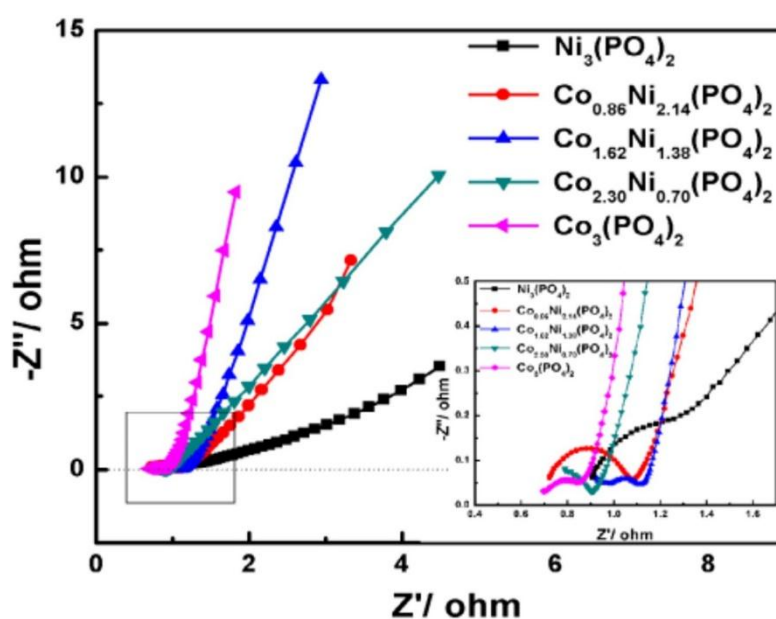


Figure 1.14 EIS of the cobalt nickel phosphate electrodes with different ratios.⁹²

1.8.4 Cyclic stability and coulombic efficiency

Cyclic stability measurements were used to assess the supercapacitor efficiency at a certain scan rate or current density. Moreover, the following equation 1.18 was used to obtain the coulombic efficiency (η):

$$\eta = \frac{t_D}{t_C} \times 100 \quad (1.18)$$

Where η stands for coulombic efficiency, t_D stands for the discharge time in seconds, and t_C stands for the charging time in seconds.

1.9 Metal oxide and phosphate-based supercapacitors

Metal oxides have drawn significant interest among the several nanomaterials used for SCs because of their unique physical and chemical characteristics. Metal oxides are easier to synthesize than metal chalcogenides, more ecologically friendly, chemically stable, and compatible with a wide range of electrolytes, all of which are necessary for the creation of durable and affordable SC devices. Furthermore, due to the combined effects of increased electrode surface area and numerous oxidation states, metal oxides display higher theoretical specific capacitance/capacity, higher energy density, and better electrochemical performance compared to graphene and other 2D materials.^{93,94} A wide variety of metal oxides, including binary metal oxides like RuO₂, MnO₂, TiO₂, NiO, Co₃O₄, V₂O₅, MoO₃, and Cr₂O₃, and ternary metal oxides like CuCo₂O₄, NiCo₂O₄, and ZnCo₂O₄, have been either directly exfoliated from their respective bulk counterparts or successfully assembled from solutions containing salt precursors.⁹⁵ Due to the quick, reversible redox processes of ruthenium oxide (RuO₂) and manganese oxide (MnO₂), for instance, have been widely researched as electrode materials for SCs.^{96,97}

During 1987 to 1990 the research community paid close attention to metal phosphates, especially the layered metal phosphonates and phosphates,⁹⁸ because they exhibit exceptional performance in the fields of materials science, catalysis, ion exchange, proton conductivity, interface chemistry, and photochemistry.^{99–103} Besides above-mentioned properties metal phosphate-based materials are broadly used as pseudocapacitive materials in recent years due to their high conductivity and high electrochemical activity.¹⁰⁴ Varied sources of ammonium solvents were used to synthesize various NH₄CoPO₄·H₂O nano/micro sized hierarchical architectures by Pang et.al. The NH₄CoPO₄·H₂O with the size of 20–30 nm delivers a specific capacitance of 1142.9 F/g at 5 mV/s in 3 M KOH aqueous solution.¹⁰⁵ Wang and co-workers synthesised layered NH₄CoPO₄·H₂O microbundles consisting of 1D layered microrods through a facile hydrothermal method. This 1D layered microbundle electrode delivers a specific capacitance 662 F/g at 1.5 A/g current density. Moreover,

this 1D layered microbundle retains 92.7 % of its initial capacitance after 3000 cycles.¹⁰⁶ Due to the low cost, layered structure, strong reversibility, and high conductivity of metal pyrophosphates, they have recently been used as active electrode materials for catalysis and energy storage applications. The well-connected layered structure of metal pyrophosphates is the reason behind their great electrical conductivity.¹⁰⁷ $\text{Co}_2\text{P}_2\text{O}_7/\text{C}$ hybrid was synthesized through calcination process at 900 °C by Zhang and co-workers. The as synthesized hybrid was further employed as a positive active material and 3D porous graphene as a negative active material to fabricate a supercapacitor device. The device projects a specific capacitance value of 70.1 F/g and energy density of 21.9 Wh/kg at a power density of 375 W/kg.¹⁰⁸ A hydrothermal method followed by calcination at 650 °C was employed by Wei et. al. to synthesize hexagonal plate like porous $\text{Ni}_2\text{P}_2\text{O}_7$. The synthesized $\text{Ni}_2\text{P}_2\text{O}_7$ delivers a specific capacitance of 557.7 F/g at a current density of 1.2 A/g. A solid-state flexible device was fabricated by using Na-doped $\text{Ni}_2\text{P}_2\text{O}_7$ and graphene as positive and negative electroactive material respectively. The as fabricated device projects a highest energy density of 23.4 Wh/kg at a power density of 6.53 kW/kg with a cycling stability of 5000 cycles.¹⁰⁹ The transition metal phosphites have drawn a lot of attention since Attfield and colleagues initially described their synthesis of $\text{M}_{11}(\text{HPO}_3)_8(\text{OH})_6$ (M = Zn, Co, and Ni) in 1993,^{110,111} due to their microporous structure and have potential to show catalytic, electrical, optical and magnetic properties.^{112–115} Mild hydrothermal process was followed by Pang and co-workers for the synthesis of cobalt phosphite microarchitectures. This cobalt phosphite shows a specific capacitance of 312 F/g at 1.25 A/g current density. The above mentioned cobalt phosphite possesses an excellent cycling stability as the material maintains 89.4 % of its initial capacitance after 3000 cycles at 1.25 A/g.¹¹² Wang et. al. produced $\text{NiHPO}_3 \cdot \text{H}_2\text{O}$ through a single step hydrothermal route. The synthesized $\text{NiHPO}_3 \cdot \text{H}_2\text{O}$ was used as a positive active material and porous carbon as negative active material was assembled together to fabricate an asymmetric supercapacitor device that delivers an energy density of 42.6 Wh/kg at a power density of 449.1 W/kg. The device retains 84.7 % of its initial capacitance even after 10,000 cycles.¹¹⁶

1.10 References

- 1 W. Ai, W. Zhou, Z. Du, Y. Du, H. Zhang, X. Jia, L. Xie, M. Yi, T. Yu and W. Huang, *J. Mater. Chem.*, 2012, **22**, 23439.
- 2 T. N. Huan, G. Rousse, S. Zanna, I. T. Lucas, X. Xu, N. Menguy, V. Mougél and M. Fontecave, *Angew. Chemie*, 2017, **129**, 4870–4874.
- 3 J. A. Turner, *Science*, 2004, **305**, 972–974.
- 4 J.-X. Feng, S.-H. Ye, H. Xu, Y.-X. Tong and G.-R. Li, *Adv. Mater.*, 2016, **28**, 4698–4703.
- 5 M. D. Leonard, E. E. Michaelides and D. N. Michaelides, *Renew. Energy*, 2020, **145**, 951–962.
- 6 Y. Jiao, Y. Zheng, M. Jaroniec and S. Z. Qiao, *Chem. Soc. Rev.*, 2015, **44**, 2060–2086.
- 7 X. Wang, Y. Orikasa and Y. Uchimoto, *ACS Catal.*, 2016, **6**, 4195–4198.
- 8 Y. Lee, J. Suntivich, K. J. May, E. E. Perry and Y. Shao-Horn, *J. Phys. Chem. Lett.*, 2012, **3**, 399–404.
- 9 S. M. Alia, S. Shulda, C. Ngo, S. Pylypenko and B. S. Pivovar, *ACS Catal.*, 2018, **8**, 2111–2120.
- 10 N. Mamaca, E. Mayousse, S. Arrii-Clacens, T. W. Napporn, K. Servat, N. Guillet and K. B. Kokoh, *Appl. Catal. B Environ.*, 2012, **111–112**, 376–380.
- 11 N. Cheng, S. Stambula, D. Wang, M. N. Banis, J. Liu, A. Riese, B. Xiao, R. Li, T.-K. Sham, L.-M. Liu, G. A. Botton and X. Sun, *Nat. Commun.*, 2016, **7**, 13638.
- 12 X. Chia, A. Y. S. Eng, A. Ambrosi, S. M. Tan and M. Pumera, *Chem. Rev.*, 2015, **115**, 11941–11966.
- 13 A. K. Samantara, S. Kamila, A. Ghosh and B. K. Jena, *Electrochim. Acta*, 2018, **263**, 147–157.
- 14 J. Zhou, C. Zhang, T. Niu, R. Huang, S. Li, J. Z. Zhang and J. G. Chen, *ACS Appl. Energy Mater.*, 2018, **1**, 4599–4605.
- 15 Y. Pei, Y. Cheng, J. Chen, W. Smith, P. Dong, P. M. Ajayan, M. Ye and J. Shen, *J. Mater. Chem. A*, 2018, **6**, 23220–23243.

- 16 A. K. Samantara and S. Ratha, *Metal Oxides/Chalcogenides and Composites*, Springer International Publishing, Cham, 2019.
- 17 C. Acar and I. Dincer, in *Comprehensive Energy Systems*, Elsevier, 2018, pp. 1–40.
- 18 X. Wang, X. Huang, W. Gao, Y. Tang, P. Jiang, K. Lan, R. Yang, B. Wang and R. Li, *J. Mater. Chem. A*, 2018, **6**, 3684–3691.
- 19 S. Anantharaj, S. R. Ede, K. Sakthikumar, K. Karthick, S. Mishra and S. Kundu, *ACS Catal.*, 2016, **6**, 8069–8097.
- 20 J. Zhu, L. Hu, P. Zhao, L. Y. S. Lee and K.-Y. Wong, *Chem. Rev.*, 2020, **120**, 851–918.
- 21 H. Zhong, C. Campos-Roldán, Y. Zhao, S. Zhang, Y. Feng and N. Alonso-Vante, *Catalysts*, 2018, **8**, 559.
- 22 Z. Pu, T. Liu, G. Zhang, H. Ranganathan, Z. Chen and S. Sun, *ChemSusChem*, 2021, **14**, 4636–4657.
- 23 Q. Liang, G. Brocks and A. Bieberle-Hütter, *J. Phys. Energy*, 2021, **3**, 026001.
- 24 N.-T. Suen, S.-F. Hung, Q. Quan, N. Zhang, Y.-J. Xu and H. M. Chen, *Chem. Soc. Rev.*, 2017, **46**, 337–365.
- 25 M. Zeng and Y. Li, *J. Mater. Chem. A*, 2015, **3**, 14942–14962.
- 26 Y. Shi and B. Zhang, *Chem. Soc. Rev.*, 2016, **45**, 1529–1541.
- 27 K. R. Cooper and M. Smith, *J. Power Sources*, 2006, **160**, 1088–1095.
- 28 E. Fabbri, A. Habereder, K. Waltar, R. Kötz and T. J. Schmidt, *Catal. Sci. Technol.*, 2014, **4**, 3800–3821.
- 29 R. D. L. Smith, M. S. Prévot, R. D. Fagan, S. Trudel and C. P. Berlinguette, *J. Am. Chem. Soc.*, 2013, **135**, 11580–11586.
- 30 J. K. Das, A. K. Samantara, A. K. Nayak, D. Pradhan and J. N. Behera, *Dalt. Trans.*, 2018, **47**, 13792–13799.
- 31 A. Dutta, A. K. Samantara, S. K. Dutta, B. K. Jena and N. Pradhan, *ACS Energy Lett.*, 2016, **1**, 169–174.

- 32 T. Y. Ma, S. Dai, M. Jaroniec and S. Z. Qiao, *J. Am. Chem. Soc.*, 2014, **136**, 13925–13931.
- 33 C. Tang, W. Wang, A. Sun, C. Qi, D. Zhang, Z. Wu and D. Wang, *ACS Catal.*, 2015, **5**, 6956–6963.
- 34 C. Zhang, Y. Huang, Y. Yu, J. Zhang, S. Zhuo and B. Zhang, *Chem. Sci.*, 2017, **8**, 2769–2775.
- 35 J. K. Das, A. Padhy, S. Parida, R. M. Pathi and J. N. Behera, *Dalt. Trans.*, 2022, **51**, 11526–11535.
- 36 H. Jin, J. Wang, D. Su, Z. Wei, Z. Pang and Y. Wang, *J. Am. Chem. Soc.*, 2015, **137**, 2688–2694.
- 37 Y.-Y. Zhang, X. Zhang, Z.-Y. Wu, B.-B. Zhang, Y. Zhang, W.-J. Jiang, Y.-G. Yang, Q.-H. Kong and J.-S. Hu, *J. Mater. Chem. A*, 2019, **7**, 5195–5200.
- 38 J. Zang, S.-J. Bao, C. M. Li, H. Bian, X. Cui, Q. Bao, C. Q. Sun, J. Guo and K. Lian, *J. Phys. Chem. C*, 2008, **112**, 14843–14847.
- 39 Y.-Y. Liang, H. L. Li and X.-G. Zhang, *J. Power Sources*, 2007, **173**, 599–605.
- 40 G. Zhao, K. Rui, S. X. Dou and W. Sun, *Adv. Funct. Mater.*, 2018, **28**, 1803291.
- 41 C. Costentin, S. Drouet, M. Robert and J.-M. Savéant, *J. Am. Chem. Soc.*, 2012, **134**, 11235–11242.
- 42 X. Zou and Y. Zhang, *Chem. Soc. Rev.*, 2015, **44**, 5148–5180.
- 43 A. Padhy, A. K. Samantara and J. N. Behera, *Sustain. Energy Fuels*, 2021, **5**, 3729–3736.
- 44 J. J. Lingane, *J. Electroanal. Chem.*, 1961, **2**, 296–309.
- 45 M. Endo, T. Maeda, T. Takeda, Y. J. Kim, K. Koshiba, H. Hara and M. S. Dresselhaus, *J. Electrochem. Soc.*, 2001, **148**, A910.
- 46 E. Raymundo-Piñero, K. Kierzek, J. Machnikowski and F. Béguin, *Carbon N. Y.*, 2006, **44**, 2498–2507.
- 47 D. Qu and H. Shi, *J. Power Sources*, 1998, **74**, 99–107.
- 48 S. Shiraishi, H. Kurihara, K. Okabe, D. Hulicova and A. Oya, *Electrochem. commun.*, 2002, **4**, 593–598.

- 49 B. Xu, F. Wu, R. Chen, G. Cao, S. Chen, Z. Zhou and Y. Yang, *Electrochem. commun.*, 2008, **10**, 795–797.
- 50 J. Lee, J. Kim and T. Hyeon, *Adv. Mater.*, 2006, **18**, 2073–2094.
- 51 B. Fang and L. Binder, *J. Power Sources*, 2006, **163**, 616–622.
- 52 Q. Tang and Z. Zhou, *Prog. Mater. Sci.*, 2013, **58**, 1244–1315.
- 53 M. Inagaki, H. Konno and O. Tanaike, *J. Power Sources*, 2010, **195**, 7880–7903.
- 54 Y. Zheng, Y. Jiao, L. H. Li, T. Xing, Y. Chen, M. Jaroniec and S. Z. Qiao, *ACS Nano*, 2014, **8**, 5290–5296.
- 55 J. K. Kim, G. D. Park, J. H. Kim, S.-K. Park and Y. C. Kang, *Small*, 2017, **13**, 1700068.
- 56 D.-D. Zhao, S.-J. Bao, W.-J. Zhou and H.-L. Li, *Electrochem. commun.*, 2007, **9**, 869–874.
- 57 V. D. Silva, T. A. Simões, J. P. F. Grilo, E. S. Medeiros and D. A. Macedo, *J. Mater. Sci.*, 2020, **55**, 6648–6659.
- 58 R. Zhang, Y.-C. Zhang, L. Pan, G.-Q. Shen, N. Mahmood, Y.-H. Ma, Y. Shi, W. Jia, L. Wang, X. Zhang, W. Xu and J.-J. Zou, *ACS Catal.*, 2018, **8**, 3803–3811.
- 59 B. R. Wygant, K. Kawashima and C. B. Mullins, *ACS Energy Lett.*, 2018, **3**, 2956–2966.
- 60 A. Sivanantham, P. Ganesan and S. Shanmugam, *Adv. Funct. Mater.*, 2016, **26**, 4661–4672.
- 61 J. Wang, W. Cui, Q. Liu, Z. Xing, A. M. Asiri and X. Sun, *Adv. Mater.*, 2016, **28**, 215–230.
- 62 D. A. Lutterman, Y. Surendranath and D. G. Nocera, *J. Am. Chem. Soc.*, 2009, **131**, 3838–3839.
- 63 M. W. Kanan and D. G. Nocera, *Science (80-.)*, 2008, **321**, 1072–1075.
- 64 M. Pramanik, C. Li, M. Imura, V. Malgras, Y.-M. Kang and Y. Yamauchi, *Small*, 2016, **12**, 1709–1715.
- 65 K. M. S. Etheredge and S. J. Hwu, *Inorg. Chem.*, 1995, **34**, 1495–1499.

- 66 Y. Chang, N. E. Shi, S. Zhao, D. Xu, C. Liu, Y. J. Tang, Z. Dai, Y. Q. Lan, M. Han and J. Bao, *ACS Appl. Mater. Interfaces*, 2016, **8**, 22534–22544.
- 67 H. Du, W. Ai, Z. L. Zhao, Y. Chen, X. Xu, C. Zou, L. Wu, L. Su, K. Nan, T. Yu and C. M. Li, *Small*, 2018, **14**, 1801068.
- 68 M. Liu, Z. Qu, D. Yin, X. Chen, Y. Zhang, Y. Guo and D. Xiao, *ChemElectroChem*, 2018, **5**, 36–43.
- 69 H. J. Song, H. Yoon, B. Ju, D. Y. Lee and D. W. Kim, *ACS Catal.*, 2020, **10**, 702–709.
- 70 H. Du, X. Lin, Z. Xu and D. Chu, *J. Mater. Sci.*, 2015, **50**, 5641–5673.
- 71 M. Faisal, M. A. Hannan, P. J. Ker, A. Hussain, M. Bin Mansor and F. Blaabjerg, *IEEE Access*, 2018, **6**, 35143–35164.
- 72 V. Augustyn, P. Simon and B. Dunn, *Energy Environ. Sci.*, 2014, **7**, 1597.
- 73 X. Yu, S. Yun, J. S. Yeon, P. Bhattacharya, L. Wang, S. W. Lee, X. Hu and H. S. Park, *Adv. Energy Mater.*, 2018, **8**, 1702930.
- 74 E. Herrero, L. J. Buller and H. D. Abruña, *Chem. Rev.*, 2001, **101**, 1897–1930.
- 75 R. Warren, F. Sammoura, F. Tounsi, M. Sanghadasa and L. Lin, *J. Mater. Chem. A*, 2015, **3**, 15568–15575.
- 76 D. Wu, S. Xu, M. Li, C. Zhang, Y. Zhu, Y. Xu, W. Zhang, R. Huang, R. Qi, L. Wang and P. K. Chu, *J. Mater. Chem. A*, 2015, **3**, 16695–16707.
- 77 S. He, X. Hu, S. Chen, H. Hu, M. Hanif and H. Hou, *J. Mater. Chem.*, 2012, **22**, 5114.
- 78 Z. Wu, L. Li, J. Yan and X. Zhang, *Adv. Sci.*, 2017, **4**, 1600382.
- 79 Q. Lu, J. G. Chen and J. Q. Xiao, *Angew. Chemie Int. Ed.*, 2013, **52**, 1882–1889.
- 80 X. Hu, W. Zhang, X. Liu, Y. Mei and Y. Huang, *Chem. Soc. Rev.*, 2015, **44**, 2376–2404.
- 81 Y. Shao, M. F. El-Kady, J. Sun, Y. Li, Q. Zhang, M. Zhu, H. Wang, B. Dunn and R. B. Kaner, *Chem. Rev.*, 2018, **118**, 9233–9280.
- 82 Y. Chikaoka, E. Iwama, S. Seto, Y. Okuno, T. Shirane, T. Ueda, W. Naoi, M. T. H. Reid and K. Naoi, *Electrochim. Acta*, 2021, **368**, 137619.

- 83 P. Yin and B. You, *Mater. Today Energy*, 2021, **19**, 100586.
- 84 A. Borenstein, O. Hanna, R. Attias, S. Luski, T. Brousse and D. Aurbach, *J. Mater. Chem. A*, 2017, **5**, 12653–12672.
- 85 M. Zhi, C. Xiang, J. Li, M. Li and N. Wu, *Nanoscale*, 2013, **5**, 72–88.
- 86 S. Ratha and C. S. Rout, *ACS Appl. Mater. Interfaces*, 2013, **5**, 11427–11433.
- 87 H. Li, J. Wang, Q. Chu, Z. Wang, F. Zhang and S. Wang, *J. Power Sources*, 2009, **190**, 578–586.
- 88 N. Wang, J. Liu, Y. Zhao, M. Hu and G. Shan, *Nanotechnology*, 2019, **30**, 235403.
- 89 J. K. Das, A. K. Samantara, S. Satyarthi, C. S. Rout and J. N. Behera, *RSC Adv.*, 2020, **10**, 4650–4656.
- 90 A. Padhy, R. Kumar and J. N. Behera, *Dalt. Trans.*, 2022, **51**, 16256–16265.
- 91 G. Wang, L. Zhang and J. Zhang, *Chem. Soc. Rev.*, 2012, **41**, 797–828.
- 92 Y. Tang, Z. Liu, W. Guo, T. Chen, Y. Qiao, S. Mu, Y. Zhao and F. Gao, *Electrochim. Acta*, 2016, **190**, 118–125.
- 93 H. T. Tan, W. Sun, L. Wang and Q. Yan, *ChemNanoMat*, 2016, **2**, 562–577.
- 94 L. P. R. Moraes, J. Mei, F. C. Fonseca and Z. Sun, in *2D Nanomaterials for Energy Applications*, Elsevier, 2020, pp. 39–72.
- 95 H. Jin, C. Guo, X. Liu, J. Liu, A. Vasileff, Y. Jiao, Y. Zheng and S.-Z. Qiao, *Chem. Rev.*, 2018, **118**, 6337–6408.
- 96 S. Lee, X. Jin, I. Y. Kim, T.-H. Gu, J.-W. Choi, S. Nahm and S.-J. Hwang, *J. Phys. Chem. C*, 2016, **120**, 11786–11796.
- 97 A. Xia, W. Yu, J. Yi, G. Tan, H. Ren and C. Liu, *J. Electroanal. Chem.*, 2019, **839**, 25–31.
- 98 O. Diaz-Morales, I. Ledezma-Yanez, M. T. M. Koper and F. Calle-Vallejo, *ACS Catal.*, 2015, **5**, 5380–5387.
- 99 H. Jiang, T. Zhao, C. Li and J. Ma, *J. Mater. Chem.*, 2011, **21**, 3818.
- 100 S. Zheng, H. Xue and H. Pang, *Coord. Chem. Rev.*, 2018, **373**, 2–21.
- 101 C. Chen, W. Chen, J. Lu, D. Chu, Z. Huo, Q. Peng and Y. Li, *Angew. Chemie*,

- 2009, **121**, 4910–4913.
- 102 X. Xiao, S. Zheng, X. Li, G. Zhang, X. Guo, H. Xue and H. Pang, *J. Mater. Chem. B*, 2017, **5**, 5234–5239.
- 103 D. Xu and D. Xue, *J. Cryst. Growth*, 2006, **286**, 108–113.
- 104 H. Pang, S. Wang, W. Shao, S. Zhao, B. Yan, X. Li, S. Li, J. Chen and W. Du, *Nanoscale*, 2013, **5**, 5752.
- 105 H. Pang, Z. Yan, W. Wang, J. Chen, J. Zhang and H. Zheng, *Nanoscale*, 2012, **4**, 5946.
- 106 S. Wang, H. Pang, S. Zhao, W. Shao, N. Zhang, J. Zhang, J. Chen and S. Li, *RSC Adv.*, 2014, **4**, 340–347.
- 107 H. Pang, Y. Z. Zhang, Z. Run, W. Y. Lai and W. Huang, *Nano Energy*, 2015, **17**, 339–347.
- 108 J. Zhang, P. Liu, R. Bu, H. Zhang, Q. Zhang, K. Liu, Y. Liu, Z. Xiao and L. Wang, *New J. Chem.*, 2020, **44**, 12514–12521.
- 109 C. Wei, C. Cheng, S. Wang, Y. Xu, J. Wang and H. Pang, *Chem. - An Asian J.*, 2015, **10**, 1731–1737.
- 110 M. D. Marcos, P. Amoros and A. Le Bail, *J. Solid State Chem.*, 1993, **107**, 250–257.
- 111 M. D. Marcos, P. Amoros, A. Beltran-Porter, R. Martinez-Manez and J. P. Attfield, *Chem. Mater.*, 1993, **5**, 121–128.
- 112 H. Pang, Y. Liu, J. Li, Y. Ma, G. Li, Y. Ai, J. Chen, J. Zhang and H. Zheng, *Nanoscale*, 2013, **5**, 503–507.
- 113 K. Liao and Y. Ni, *Mater. Res. Bull.*, 2010, **45**, 205–209.
- 114 Y. Ni, K. Liao, J. Hong and X. Wei, *CrystEngComm*, 2009, **11**, 570.
- 115 R. C. Che, L.-M. Peng and W. Z. Zhou, *Appl. Phys. Lett.*, 2005, **87**, 173122.
- 116 Y. Wang, J. Liu, M. Xie, Y. Zhang, J. Chen, C. Du and L. Wan, *J. Alloys Compd.*, 2020, **843**, 155921.

CHAPTER-2

Cobalt pyrophosphate ($\text{Co}_2\text{P}_2\text{O}_7$) a durable electroactive material for electrochemical energy conversion application.

1.1 Abstract

1.2 Introduction

1.3 Experimental Section

1.3.1 Materials

1.3.2 Synthesis of $(\text{H}_3\text{O})_2 \cdot [\text{Co}_8(\text{HPO}_3)_9(\text{CH}_3\text{OH})_3] \cdot 2\text{H}_2\text{O}$ as a single source precursor for $\text{Co}_2\text{P}_2\text{O}_7$

1.3.3 Synthesis of Cobalt Pyrophosphate

1.4 Characterization techniques

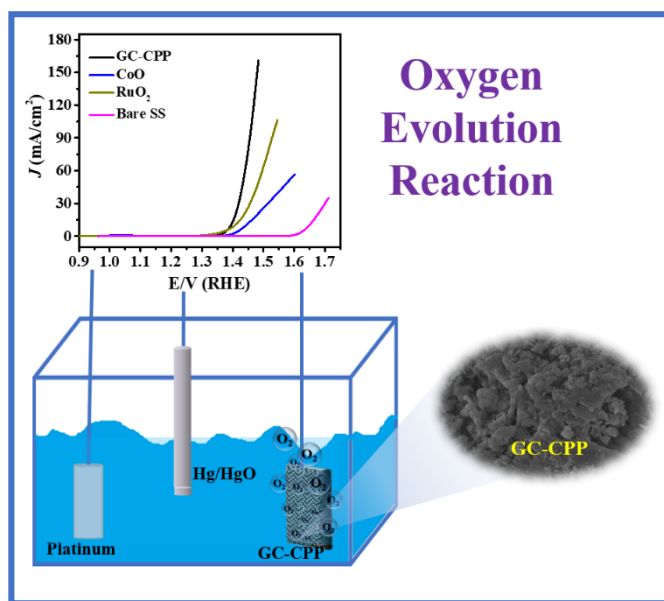
1.5 Electrode preparation and electrochemical measurements

1.6 Results and Discussions

1.7 Conclusion

1.8 References

2.1 Abstract



Graphical Abstract

Water splitting is an assuring method of qualitative as well as quantitative oxygen production to support future energy conversion systems and strictly depends on the nature of the electrocatalyst. Likewise, the electrochemical energy storage system particularly supercapacitor has of importance for future sustainability. Therefore, finding of an efficient high performance electrode material with both the electrocatalytic and electrochemical energy storage activity remained an emerging task for sustainability. In view of this challenge, we have derived a composite of partially graphitized carbon with $\text{Co}_2\text{P}_2\text{O}_7$ (GC-CPP), a non-noble metal, low-cost electroactive material from the open-framework Cobalt Phosphite. The crystal structure, surface morphology and elemental composition of the sample has been analyzed by using PXRD, Raman, FESEM, HRTEM and X-ray photoelectron spectroscopy. More importantly, the electrochemical performances have been accessed by using cyclic voltammetry, linear sweep voltammetry, galvanostatic charge-discharge and electrochemical impedance spectroscopic methods. In alkaline electrolyte, the GC-CPP catalyze the OER requiring only 165 mV overpotential to reach 10 mA/cm^2 current density with lower Tafel slope (41 $\text{mV}/\text{dec.}$). This strategy to derive highly active electrode material from open frameworks provide an opportunity to design efficient and cost-effective electrode material for renewable energy technologies.

2.2 Introduction

Water splitting technology proven to be a suitable method for the renewable energy conversion and storage i.e., alternative to the traditional fossil fuels. In particular, more focus is given to the electrochemical water splitting where catalyst plays the key role to determine efficiency. Generally, the electrocatalysts need to operate close to the Nernstian potential (E) for both the cathodic (H₂O/H₂; HER) and anodic (H₂O/O₂; OER) half reactions. The extra potential to E is termed as the overpotential (η). Out of these two half reactions, OER is relatively complex and associates with more value of overpotential.¹ It requires four electrons to break two molecules of H₂O by releasing four protons thereby forming a relatively weak oxygen to oxygen linkage (O=O).^{2,3} This is why the OER electrocatalysts need additional potential (overpotential) to the Nernstian potential and experimentally lowering of this potential remains substantially challenging. Further, to execute this proton coupled electron transfer process, the electrocatalyst need to expose prolonged oxidative reaction conditions. Even at the thermodynamic limit, the oxygen evolution reaction requires an oxidizing potential that degrade most of the functional entities of the catalyst surface. In many instances, the surface transformation to their corresponding oxides/hydroxides has been realized proving the instability of the electrocatalyst.⁴⁻⁶ Therefore, designing of an electrocatalyst with better catalytic efficacy as well as durability remains indispensable for sustainability.

Among recent developments, the noble metal based (Ir and Ru) oxides/hydroxide occupies the dominant role as OER electrocatalyst but their high cost and poor catalytic durability restricts their commercial production and application.⁷⁻¹⁰ However, the oxides/hydroxides, sulphides, nitrides, and phosphides of first row transition metals were well documented as the efficient OER electrocatalysts in terms of their low cost and ease of synthesis.^{4,11-14} Particularly, the phosphate based cobalt nanostructures are in the lime light just after the novel work by Nocera and Kanan's work in 2008.² Due to the unique layered structure and improved optical, magnetic & electrical property, the cobalt pyrophosphates are broadly used in many of the advanced applications.¹⁵⁻¹⁷ Specifically, the improved performance of cobalt pyrophosphate-based materials is ascribed to their structural rigidity, which in turn resulted from the butterfly type geometry of pyrophosphate unit.¹⁸ Therefore, efforts have been made and various

synthesis protocols have been designed to synthesize the cobalt-based pyrophosphates. In a particular work, Chang et al., have prepared coralloid type Co₂P₂O₇@C following a two-step method; preparation of polymer gel followed by high temperature annealing.¹⁵ In alkaline electrolytic condition, the Co₂P₂O₇@C catalyze the OER requiring 397 mV of overpotential to reach 10 mA/cm² current density. By following hydrothermal method, Li et al., have synthesized Co₂P₂O₇ with various surface morphologies.¹⁹ Among them, the Co₂P₂O₇ nanowires showed better OER catalytic activity requiring 359 mV of overpotential. In a recent work, carbon coated cobalt iron pyrophosphates (NCFPO/C NPs) were synthesized via a sol-gel method. The NCFPO/C NPs found to catalyze the OER showing a lower overpotential of 300 mV to deliver the state-of-the-art current density compared to that reported before.²⁰ In another report, by following a hydrothermal method, Yang's group have synthesized flake like layered potassium cobalt pyrophosphate dihydrate (K₂Co₃(P₂O₇)₂.2H₂O) that reach the 10 mA/cm² current density at only 296 mV of overpotential in 1.0 M KOH electrolyte.²¹ Through a co-precipitation method, Liu et al. have prepared Co-Fe pyrophosphate and employed as electrocatalysts for OER. It catalyzes the OER efficiently requiring only 276 mV of overpotential to reach the 10 mA/cm² current density. Although an ample of work have been performed but still more effort need to devote to deduce facile synthesis protocol for the scalable preparation of cobalt pyrophosphates having lower overpotential to deliver the benchmarked current density.

In this work, we have derived a hybrid structure of partially graphitized carbon/cobalt pyrophosphate (GC-CPP) from an inorganic open-framework Cobalt Phosphite by annealing at an optimized temperature under inert atmosphere. On employing as anode electrocatalyst, the GC-CPP catalyzes the OER efficiently which needs only 165 mV of overpotential to reach 10 mA/cm² current density. Also, it executes the catalysis process with favorable kinetics showing a Tafel slope of 41 mV/dec and robust durability (only increase of 10 mV overpotential after 20 hours of electrolysis) with an unaltered crystallinity as well as surface morphology.

2.3 Experimental Section

2.3.1 Materials

CoCl₂.6H₂O, Phosphorous acid (H₃PO₃), Ethylene glycol (EG) and diethylenetriamine

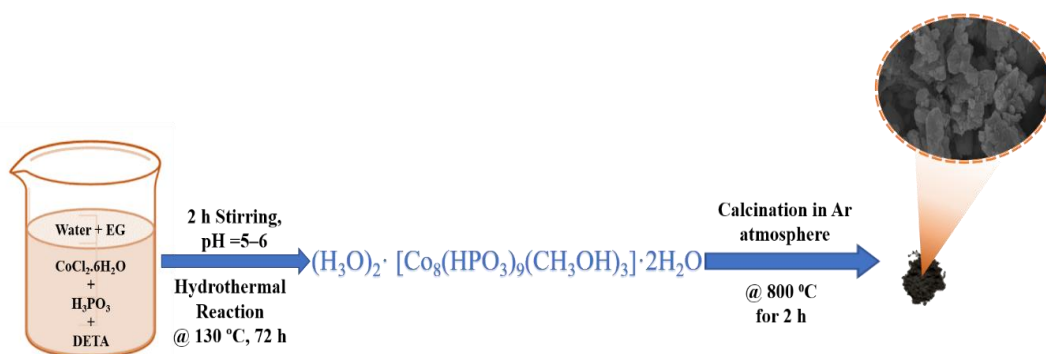
(DETA) was procured from Sigma Aldrich and used as received without further purification. Deionized water is used during the synthesis and electrochemical characterizations.

2.3.2 Synthesis of $(\text{H}_3\text{O})_2 \cdot [\text{Co}_8(\text{HPO}_3)_9(\text{CH}_3\text{OH})_3] \cdot 2\text{H}_2\text{O}$ as a single source precursor for $\text{Co}_2\text{P}_2\text{O}_7$

$(\text{H}_3\text{O})_2 \cdot [\text{Co}_8(\text{HPO}_3)_9(\text{CH}_3\text{OH})_3] \cdot 2\text{H}_2\text{O}$ abbreviated as CoHPO–CJ2 was synthesized by single step solvothermal method as per the report published elsewhere.²² In detail, 0.238 g of $\text{CoCl}_2 \cdot 6\text{H}_2\text{O}$ was added to a mixture of H_2O (1 mL) and EG (7 mL) followed by addition of 0.164 g of H_3PO_3 under constant stirring. The pH of the mixture was maintained between 5–6 by adding 0.08 mL of DETA and continued to stir for next two hours. The homogenous gel thus obtained was transferred to a Teflon lined stainless steel autoclave and placed in a preheated hot air oven at 130 °C for 3 days. After cool down, the crystals thus obtained were separated from the mother liquor, washed repeatedly with deionized water and stored in desiccator for further use.

2.3.3 Synthesis of Cobalt Pyrophosphate

The cobalt pyrophosphate was synthesized by calcining the precursor (CoHPO–CJ2) at 800 °C for two hours in argon atmosphere in a tube furnace. Here the calcining temperature was determined from the thermogravimetric analysis of precursor (CoHPO–CJ2).



Scheme 2.1 Schematic representation for the synthesis of cobalt pyrophosphate (GC-CPP)

2.4 Characterization techniques

The crystallinity of the as synthesized sample was verified by the Powder X-ray diffraction pattern using Bruker D8 advance diffractometer with Cu K α radiation ($\lambda = 1.5418 \text{ \AA}$). The morphological study of Co₂(P₂O₇) was performed using field emission scanning electron microscope (FESEM Merlin Compact with a GEMINI-I electron column, Zeiss Pvt. Ltd, Germany) and Transmission electron microscope (HRTEM, JEOL 2100F, operated at 200 kV). TEM samples were prepared with very dilute dispersion of the material in deionized water and drop casted over carbon coated Cu–grid having 200 mesh and dried under xenon lamp prior to analysis. Further the surface functionalities of the sample were analyzed by using FTIR spectrophotometer (Thermo fisher Scientific) using KBr pellet method, which is further confirmed by Raman Spectroscopy (Horiba Scientific) with a laser having wavelength of 532 nm. The porosity, pore volume and specific surface area of the samples were determined by using the Brunauer-Emmett-Teller (BET) nitrogen adsorption/desorption and Barrett-Joyner-Halenda (BJH) method at 77 K using Quanta Chrome Instruments (version 5.21).

2.5 Electrode preparation and Electrochemical Measurements

All the electrochemical measurements were performed in a three-electrode electrochemical cell containing stain less steel mesh modified sample, platinum wire and alkaline Hg/HgO as working, auxiliary and reference electrode. Here, 1.0 M and 5.0 M aqueous KOH was used as the supporting electrolyte for the OER and supercapacitor measurement. In particular, 0.5 mg of sample (cobalt pyrophosphate, CoO_x or RuO₂) added to a mixture of absolute ethanol (95 μ l) and Nafion (5 μ l of 5% Nafion solution) and mixed properly using bath sonicator. Thereafter the whole dispersion was drop casted on a precleaned stainless steel mesh (1 cm² dimension) and dried properly in a vacuum desiccator prior to use. The mass loading of 0.5 mg/cm² was maintained throughout the measurement. For OER, the linear sweep voltammogram (LSV) and cyclic voltammograms (CVs) and electrochemical impedance spectroscopy (EIS) has been performed in Biologic electrochemical work station (SP-200). All the measurements were performed with Hg/HgO reference electrode and the data are presented here in reversible hydrogen electrode (RHE) scale as per the following equation,^{23,24}

$$E_{RHE} = E_{Hg/HgO} + E_{Hg/HgO}^0 + 0.059 \text{ pH} \quad (2.1)$$

Here, $E_{Hg/HgO}$, $E_{Hg/HgO}^0$ is the observed potential with respect to the Hg/HgO reference electrode and standard potential for Hg/HgO reference electrode respectively. The electrochemical impedance spectra (EIS) were measured in a frequency range of 100 kHz to 0.1 Hz by applying an AC voltage of 5 mV amplitude and in form of Nyquist impedance (plot of imaginary impedance vs. real impedance). For supercapacitor measurement, the CVs and galvanostatic charge-discharge (GCD) profiles are recorded at different sweep rate and applied current densities respectively. Further the catalytic as well as charge storage durability of the cobalt pyrophosphate has been examined using the chronopotentiometry (at 10 mA/cm² current density) and repeated GCD profiles at an applied current density of 10 A/g.

2.6 Results and Discussions

The synthesis of cobalt pyrophosphate was carried out by a two-step method. At first, an inorganic open-framework cobalt phosphite has been synthesized using CoCl₂·6H₂O as metal source, H₃PO₃ (as phosphate source) and diethylenetriamine (DETA) as structure directing agent via a solvothermal method. The diffraction pattern completely matches with the simulated patterns as reported previously conforming the formation of the framework.²² In the second step, the cobalt pyrophosphate [CPP; Co₂(P₂O₇)] was prepared by annealing the framework at 800 °C for 2 hours under continuous flow of argon. The synthesis process is illustrated schematically in Scheme 2.1.

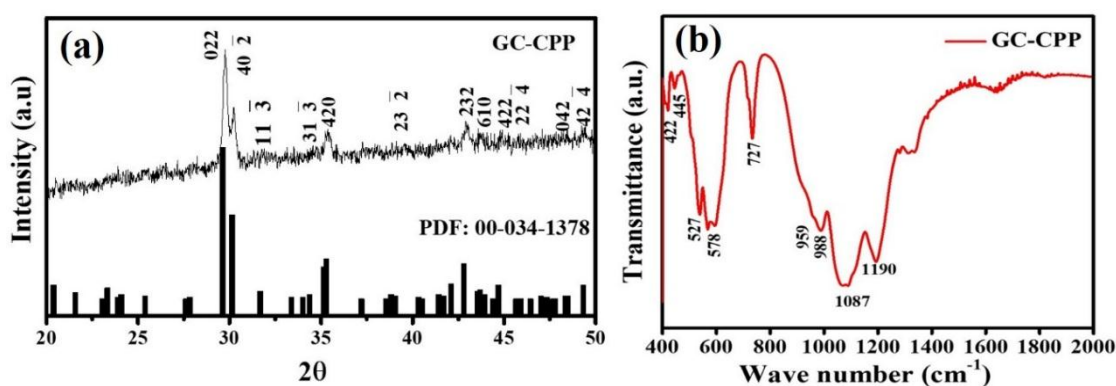


Figure 2.1 (a) XRD and (b) IR spectra of synthesized GC-CPP

The phase purity and crystallinity of the calcined framework was examined by using powder X-ray diffraction and Raman spectrophotometer. The PXRD pattern as shown in Figure 2.1 (a), conforms the formation of monoclinic Co₂P₂O₇ with space group of B21/c (JCPDS no. 00-034-1378). Here, two well defined peaks at 2θ of 29.71 (022) and 30.21 (40 $\bar{2}$) are observed along with less intense peaks at 31.86, 34.47, 35.41, 39.56, 43.03, 43.97, 44.91, 45.93, 48.23 and 49.4 assigned to the corresponding Miller indices of (11 $\bar{3}$), (31 $\bar{3}$), (420), (23 $\bar{2}$), (232), (610), (422), (22 $\bar{4}$), (042) and (42 $\bar{4}$) of the facets of Co₂P₂O₇ respectively. Further the presence of P₂O₇⁴⁻ anion in the cobalt pyrophosphate unit was confirmed from the infrared spectroscopic analysis (Fig. 2.1 (b)).^{25,26} The vibrations corresponding to the anion i.e., P₂O₇⁴⁻ are observed in the frequency range of 400-1400 cm⁻¹.²⁷ As per the vibrational stretching and bending modes, the anion constitutes PO₂²⁻ radical and P-O-P bridge.²⁸ In P-O-P bridge, the P-O strength is comparatively weaker than the PO₂²⁻ radical, thereby showing stretching/bending vibrations at higher frequencies compared to that of P-O-P bridge.²⁸ Further, the asymmetric and symmetric stretching vibrations take place in the frequencies of 1100-1000 and 1000-900 cm⁻¹ respectively, while the bending vibrations for PO₂²⁻ radical shows in the region of 600-500 cm⁻¹. The asymmetric vibrations for the P-O-P bridge and P-O-P deformations as well as torsional/external modes are observed at 727 cm⁻¹ and 580-420 cm⁻¹.²⁸

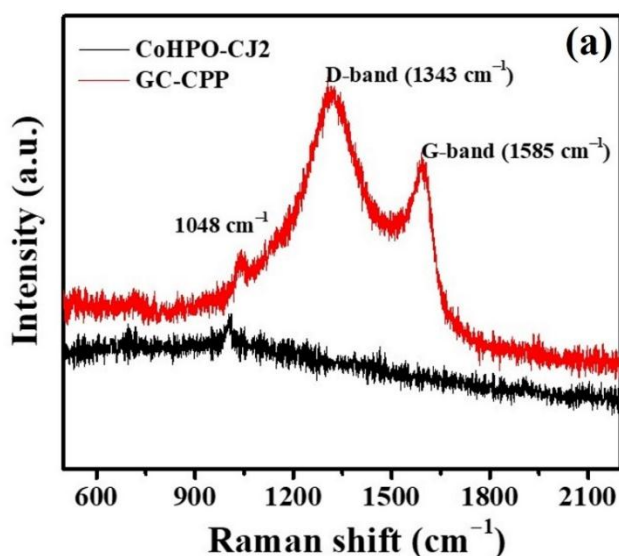


Figure 2.2 (a) Raman spectra of CoHPO-CJ2 & GC-CPP

The Raman spectrum of the cobalt phosphite framework shows a single peak at 1000 cm^{-1} assigned to the P-O-P linkage which is shifted to 1048 cm^{-1} after annealing (in case of CPP) that is assigned to the phosphate moieties in the as prepared cobalt pyrophosphate (Fig. 2.2(a)). In addition to this, a pair of distinguished peaks at 1343 cm^{-1} and 1585 cm^{-1} were observed in the post annealed pyrophosphate sample assigned to the D- and G-band of graphitic carbon network proving the partial graphitization of the trapped CH_3OH during the course of the heat treatment.²⁹ Therefore, the as prepared cobalt pyrophosphate is named as partially graphitized carbon coated cobalt pyrophosphate (GC-CPP). The surface morphology of the GC-CPP has been studied by field emission scanning electron and high-resolution transmission electron microscopy. In spite of a defined morphology, the GC-CPP shows agglomerated structure which might be due to the graphitization of the ligands during the course of calcination (Fig. 2.3 (a)). Similar morphology has also been conferred from the TEM images (Fig. 2.3 (b-c)). Further, the well distinguished fringes (4.3 \AA and 3.01 \AA assigned 002 and 022 planes) and dot like SAED pattern showed the corresponding planes at [(002), (400), (022), ($44\bar{2}$), 234, ($23\bar{2}$)] of cobalt pyrophosphate completely corroborating with that observed from the PXRD Fig. 2.3 (d)).

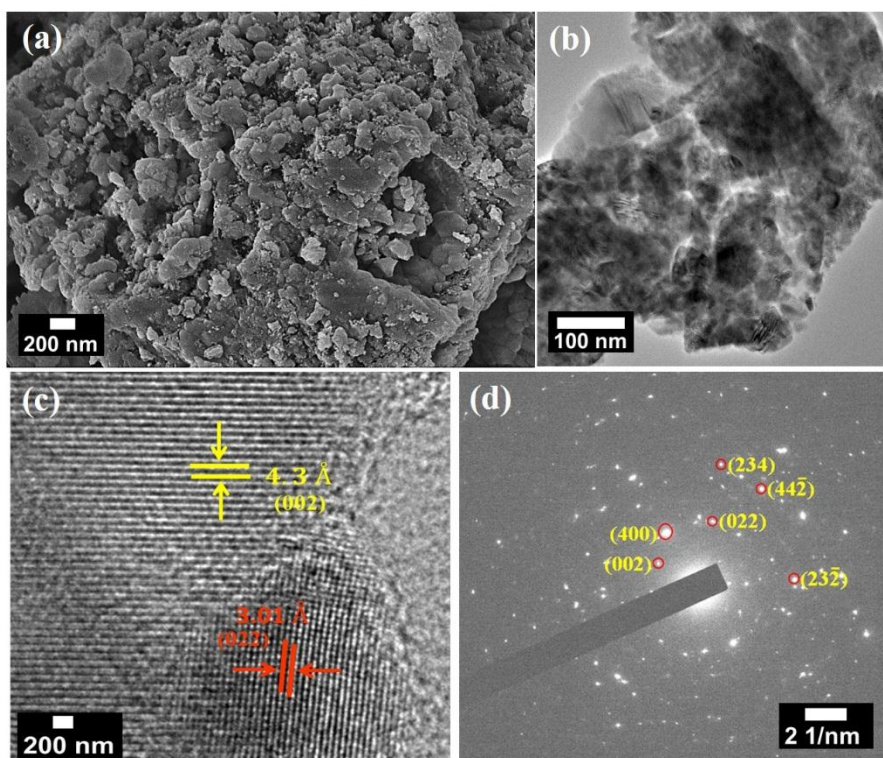


Figure 2.3 (a) FESEM, (b-c) HRTEM and (d) SAED pattern of GC-CPP.

To further ascertain the elemental composition, X-ray photoelectron spectroscopy of the GC-CPP was performed. The survey spectrum conforms the presence of cobalt, phosphorous, oxygen and carbon (Fig. 2.4 (a)). The high-resolution spectrum of Co 2p found to splits forming a doublet assigned to Co 2p 1/2 (798.3 eV) and Co 2p 3/2 (782.02 eV) respectively accompanying with two satellite peaks (786.5 and 803.4 eV) confirming the presence of Co in +2 oxidation state (Fig. 2.4 (b)).^{30,31} The peak at 133.2 eV is assigned to the P 2p energy levels of the phosphorous (Fig. 2.4 (c)).³² The O 1s deconvoluted into two peaks as shown in (Fig. 2.4 (d)). The peak centred at 533.1 eV and 531.5 eV are assigned to the P-O-P and P=O linkage of Co-pyrophosphate.³³ The partial graphitization of trapped methanol during the annealing is also supported by the C 1s peak at 284.5 eV (for C=C bond) (Fig. 2.4 (e)).²⁹

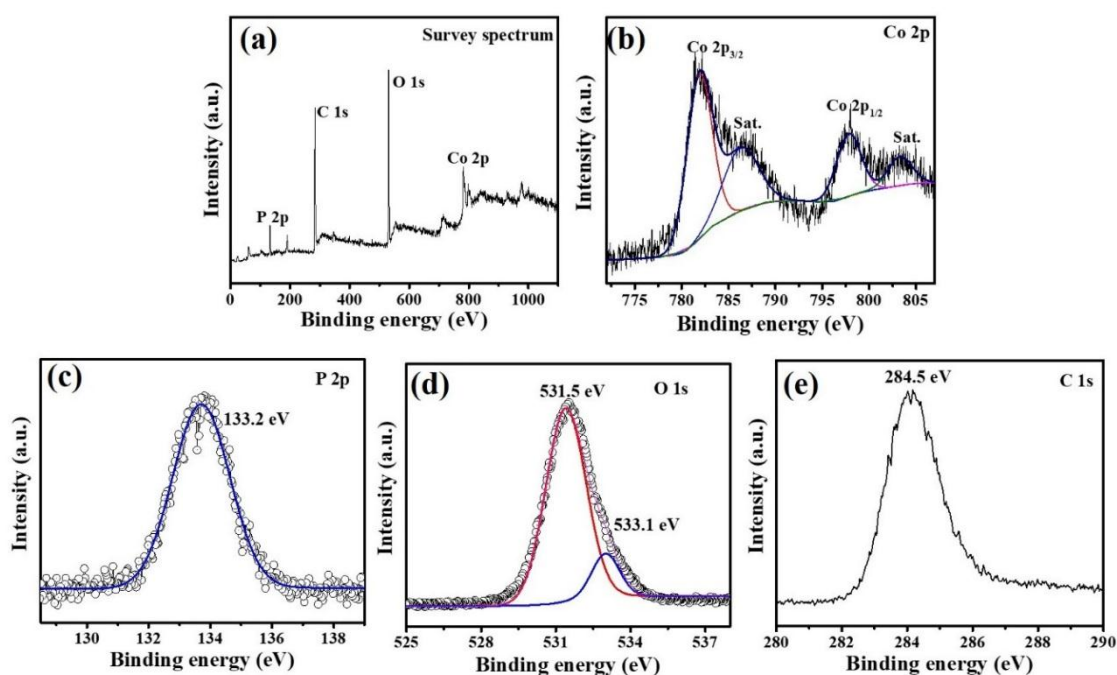


Figure 2.4 (a) Survey and high-resolution X-ray photoelectron spectrum of (b) Co 2p, (c) P 2p, (d) O 1s and (e) C 1s of GC-CPP.

After synthesis and systematic characterization, the electrocatalytic activity of the GC-CPP sample towards oxygen evolution reaction was examined in a three-electrode electrochemical cell. Here, the sample casted in stainless-steel mesh, bare platinum wire and alkaline Hg/HgO are taken as working, counter and reference electrode respectively and all the measurements were carried out using 1 M KOH electrolyte. At first the

electrode was cycled three times and the third cycle was considered to study the electrocatalytic activity. Figure 2.5 (a) illustrates the *iR*-compensated linear sweep voltammograms of GC-CPP, bare stainless-steel mesh, CoO and RuO₂ at a sweep rate of 5 mV/s. It has been observed that the GC-CPP modified electrode shows highest OER current density at 1.6 V and require only 165 mV overpotential to achieve the standard metric current density (10 mA/cm²). This value is not only lower than the commercial RuO₂ (178 mV) and CoO (213 mV) but also surpasses many of the cobalt based electrocatalysts (the detail comparison with other reported materials is presented in (Table 2.1). Further, the OER kinetics of all the samples were studied by Tafel plots (plot of log of current density against overpotential) obtained from the corresponding LSVs. As shown in Figure 2.5 (b), the Tafel slope for GC-CPP is only 41 mV/dec, which is significantly lower than that of RuO₂ (78 mV/dec.), commercial CoO (50 mV/dec.) and many of the reported electrocatalysts. The lower overpotential and Tafel slope values clearly justifies the dominant electrocatalytic OER activities of the as prepared GC-CPP.

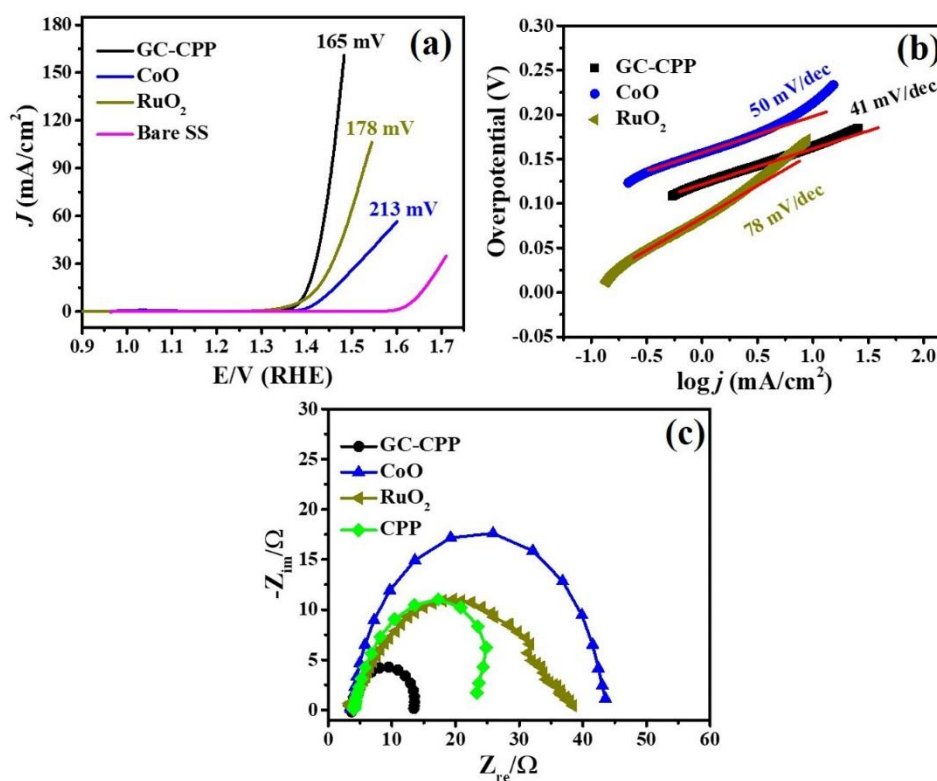


Figure 2.5 (a) Linear sweep voltammogram, (b) Tafel plot, (c) Nyquist impedance spectrum

Further, the rate of electron transfer on the electrode reaction has been accessed from the charge transfer resistance (R_{CT}), which was calculated by using Randles equation from the obtained Nyquist (plot of imaginary impedance against real impedance) impedance spectrum (EIS). Generally, lower R_{CT} values demonstrate better charge transfer and higher conductivity of the electrode material. As presented in Figure 2.5 (c), the GC-CPP shows lower charge transfer resistance compared to that of RuO₂ and commercial CoO suggesting the faster electron/mass transfer rate in the OER process among other catalysts demonstrating better electrocatalytic activity. Further the contribution of graphitized carbon content as conducting additive in the GC-CPP is verified by comparing the EIS of carbon free cobalt pyrophosphate (CPP). For this purpose, TGA of GC-CPP has been performed in air and the carbon content get removed leaving behind the carbon free CPP. As can be seen from Figure 2.5 (c), the CPP shows nearly two times higher R_{CT} value compared to that of GC-CPP. Therefore, we presumed that the presence of graphitized carbon increases the conductivity of the GC-CPP thereby increasing the electrochemical activities.

Moreover, the electrochemical accessible surface area of the samples has been calculated from the C_{dl} values. Since the C_{dl} has a good correlation with the sweep rate and peak current density, and can be obtained from the slope of the plot of sweep rate (ϑ) and current (i) at a particular potential value as per the equation presented in the supporting information. Figure 2.6 are the CVs in non-Faradaic region and C_{dl} for all the samples studied here. Among them the GC-CPP shows higher C_{dl} and thus higher ECSA (13.52 cm²) compared to commercial RuO₂ (9.25 cm²) and CoO (1.31 cm²). Not only the ECSA but also the GC-CPP shows higher values of roughness factor (R_f) signifying the availability of more electrolyte surface area and exposed electrochemically active centers facilitating the OER electrocatalytic process.

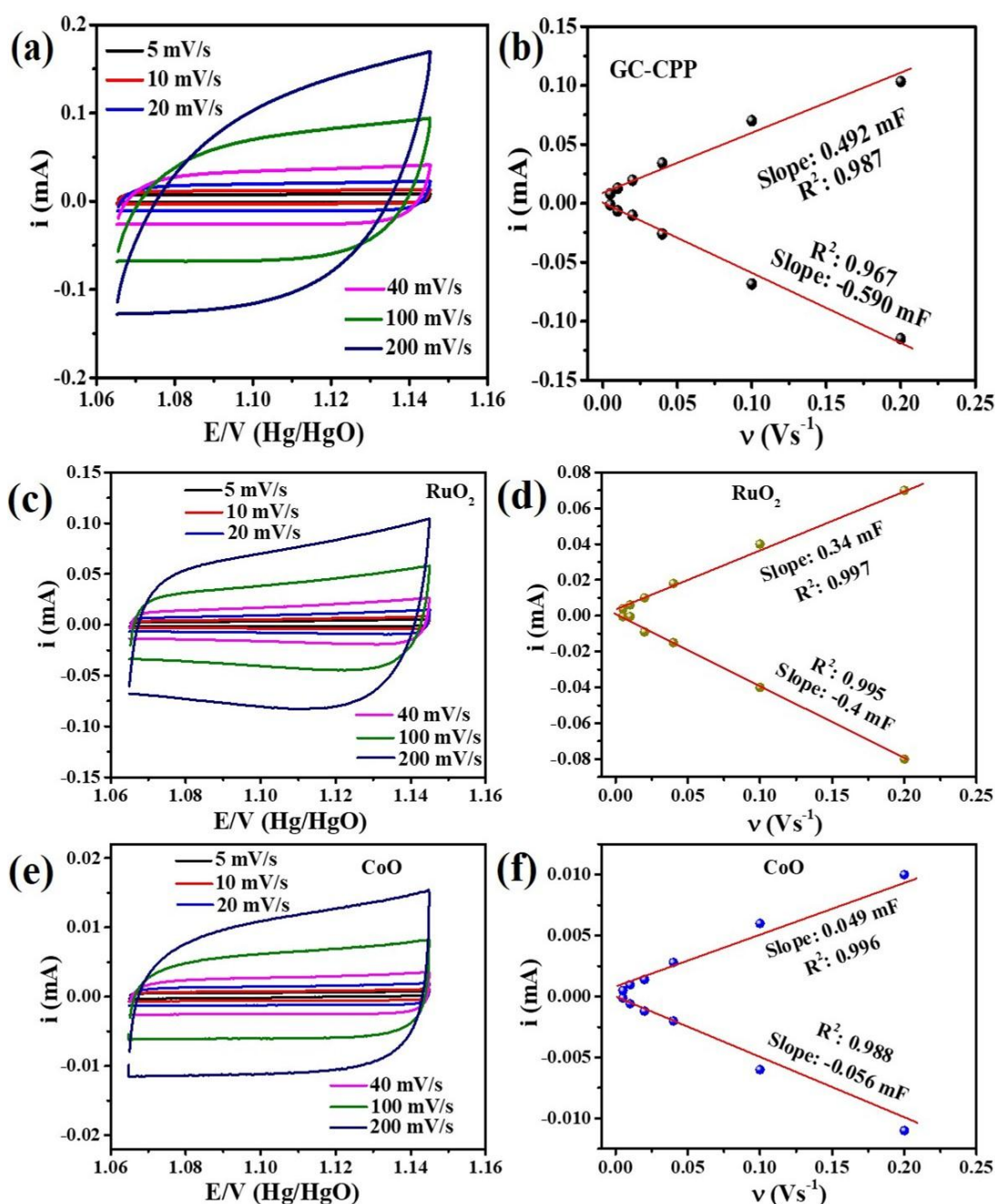


Figure 2.6 (a), (c) & (e) Cyclic voltammograms at different sweep rate in non-Faradic potential window, (b), (d) & (f) plot of cathodic and anodic current against sweep rate for GC-CPP, RuO₂ and CoO respectively.

The catalytic stability as well as transformation of the catalyst surface is an important parameter to propose the durability of an electrocatalyst. Therefore, the electrocatalytic stability for the cobalt pyrophosphate modified electrode was performed using the chronopotentiometry technique at 10 mA/cm² current density. Interestingly, a

negligible increase in overpotential (of about 10 mV) after 20 hours of electrolysis was observed demonstrating the excellent catalytic durability (Fig. 2.7 (a)). Which is also supported by comparing the LSV curve after 20 hours of electrolysis with the initial one (Fig. 2.7 (b)).

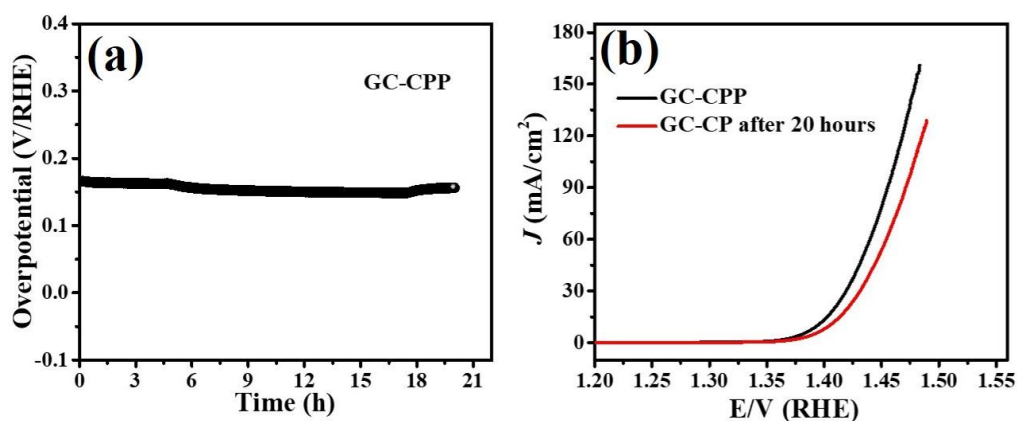


Figure 2.7 (a) Long term stability at 10 mA/cm² current density for GC-CPP, (b) LSV before and after 20 hours of stability test.

Further to support this observation, the post catalytic sample was collected and their crystallinity, surface morphology and elemental composition was analyzed by PXRD, FESEM and X-ray photoelectron spectroscopy. A similar diffraction pattern as that of the pristine GC-CPP along with some unidentified peaks were observed. This demonstrates the intactness of crystal structure with formation of some other components during continuous electrolysis for 20 hours (Fig. 2.8 (a)). Likewise, no significant change in surface morphology has been noticed in case of the post OER sample (Fig. 2.8 (b)).

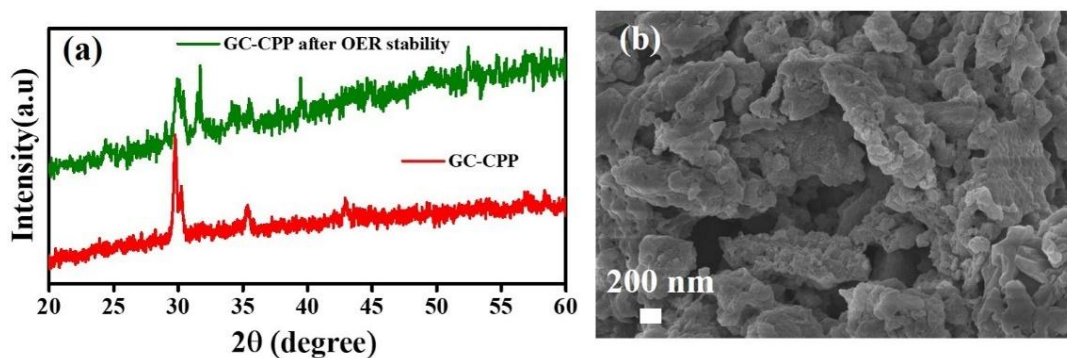


Figure 2.8 (a) PXRD and (b) FESEM of GC-CPP post OER

The full survey X-ray photoelectron spectrum illustrates the existence of Co, P, O and C. Like the pristine GC-CPP, the deconvoluted high resolution Co 2p spectrum of post OER sample shows Co 2p_{1/2} and Co 2p_{3/2} along with two shake up satellites (Fig. 2.9). Also, no change in the binding energy for the P 2p peak observed revealing an unaltered surface composition of the pyrophosphate after the OER stability test. The post stability GC-CPP demonstrates the structural as well as compositional robustness even in such harsh alkaline electrolytic condition. The ease of synthesis and excellency in electrocatalytic behavior proven the beneficial of the as synthesized sample as a suitable and efficient OER electrocatalyst for future electrolyser.

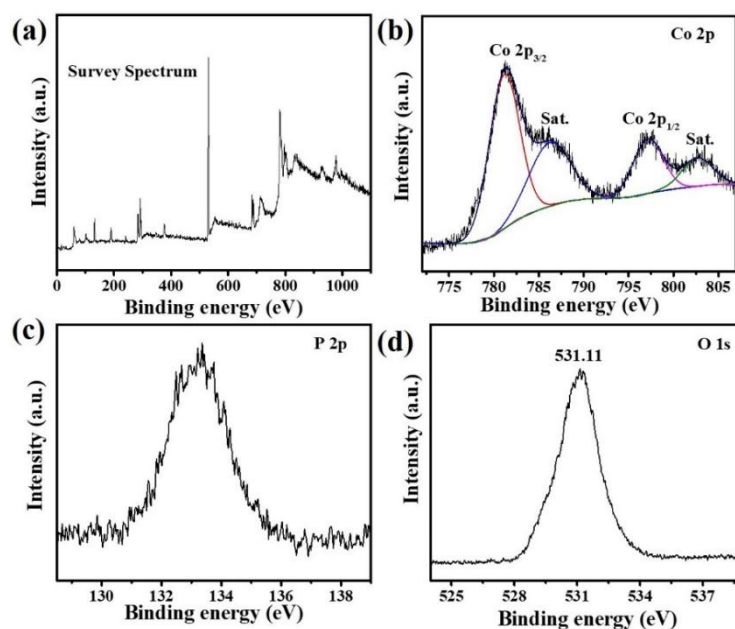


Figure 2.9 (a) Survey and high-resolution X-ray photoelectron spectrum of (b) Co 2p, (c) P 2p, and (d) O 1s of GC-CPP after OER stability measurement.

Table 2.1 OER performance comparison of GC –CPP with reported materials

Sample	Loading (mg/cm ²)	Tafel slope (mV/dec)	Overpotential (V) @ 10 mA/cm ²	Electrolyte (M)	References
Ultrafine CoP-CNT	0.28	50	0.330	0.1 (NaOH)	<i>ACS Appl. Mater. Interfaces</i> , 2018, 10 , 28412–28419.
CoP NRs/C	0.71	71	0.32	1 M KOH	<i>ACS Catal.</i> , 2015, 5 , 6874–6878.
CoP NPs/C	0.71	99	0.34	1	
CoMnP	0.28	61	0.33	1	<i>J. Am. Chem. Soc.</i> , 2016, 138 , 4006–4009.
Co ₂ P	0.28	128	0.37	1	
Co ₂ P (Nanoneedles)	0.2	50	0.31	1	<i>ACS Energy Lett.</i> , 2016, 1 , 169–174.
Co ₃ (PO ₄) ₃ @N-C	0.20.2	62	0.317	1	<i>J. Mater. Chem. A</i> , 2016, 4 , 8155–8160.
CoFePi	0.25	33	0.315	0.1	<i>Small</i> , 2018, 14 , 1704403
CoFePi	0.25	31	0.277	1	
CoPi	0.25	61	0.388	0.1	
FePi + CoPi	0.25	51	0.355	0.1	
CoNiPi	0.25	87	0.402	0.1	
CoCePi	0.25	75	0.374	0.1	
CoFeNiPi	0.25	51	0.309	0.1	
NCoM-SS-Ar	0.14	76	0.340	1	<i>Angew. Chemie</i> , 2019, 31 , 8418-8423.
Mesoporous CoPi-1	0.2	58.7	0.380	1	<i>Small</i> , 2016, 12 , 1709–1715.
Hollow Co ₃ (PO ₄) ₂	0.12	84	N.A.	1	<i>J. Mater. Chem. A</i> , 2014, 2 , 20182–20188.
Co ₃ (OH) ₂ (HPO ₄) ₂ /NF	2 on NF	69	0.240	1	<i>Adv. Funct. Mater.</i> , 2019, 29 , 1808632.
Co ₂ P ₂ O ₇	0.5	54.1	0.359	1	<i>Small</i> , 2018, 14 ,

					1801068.
Na ₂ Co _{0.75} Fe _{0.25} P ₂ O ₇ /C NPs	-	47	0.300	0.1	<i>ACS Catal.</i> , 2020, 10 , 702–709.
Co ₂ (P ₂ O ₇)	0.5	41	0.165	1	Present work

2.7 Conclusion

In this work, we have derived a composite of partially graphitized carbon with cobalt pyrophosphate (GC-CPP) from an open-framework Cobalt Phosphite (CoHPO–CJ2) and explored its electrocatalytic performance in alkaline medium. The GC-CPP shows an overpotential of 165 mV to reach the state-of-the-art current density of 10 mA/cm². Because of the higher crystallinity, availability of more accessible surface area and number of electrocatalytic active centers, the GC-CPP shows high electrocatalytic activity for OER compared to the previously reported cobalt based electrocatalysts. Interestingly, the crystallinity, surface morphology and composition of GC-CPP remains unaltered after 20 hours of electrolysis proving the robustness of the material. We strongly believe that the synthesis strategy of GC-CPP will open new routes for the fabrication of electrodes for the future energy conversion system.

2.8 References

- 1 T. A. Betley, Q. Wu, T. Van Voorhis and D. G. Nocera, *Inorg. Chem.*, 2008, 47, 1849–1861.
- 2 M. W. Kanan and D. G. Nocera, *Science*, 2008, 321, 1072–1075.
- 3 R. Elsenberg and H. B. Gray, *Inorg. Chem.*, 2008, 47, 1697–1699.
- 4 A. Dutta, A. K. Samantara, S. K. Dutta, B. K. Jena and N. Pradhan, *ACS Energy Lett.*, 2016, 1, 169–174.
- 5 J. Chang, Y. Xiao, M. Xiao, J. Ge, C. Liu and W. Xing, *ACS Catal.*, 2015, 5, 6874–6878.
- 6 L. A. Stern, L. Feng, F. Song and X. Hu, *Energy Environ. Sci.*, 2015, 8, 2347–

- 2351.
- 7 P. Li, Z. Jin and D. Xiao, *J. Mater. Chem. A*, 2014, 2, 18420–18427.
 - 8 H. S. Ahn and T. D. Tilley, *Adv. Funct. Mater.*, 2013, 23, 227–233.
 - 9 J. D. Blakemore, N. D. Schley, D. Balcells, J. F. Hull, G. W. Olack, C. D. Incarvito, O. Eisenstein, G. W. Brudvig and R. H. Crabtree, *J. Am. Chem. Soc.*, 2010, 132, 16017–16029.
 - 10 R. Liu, Y. Wang, D. Liu, Y. Zou and S. Wang, *Adv. Mater.*, 2017, 29, 1701546.
 - 11 S. Ratha, A. K. Samantara, K. K. Singha, A. S. Gangan, B. Chakraborty, B. K. Jena and C. S. Rout, *ACS Appl. Mater. Interfaces*, 2017, 9, 9640–9653.
 - 12 A. K. Samantara, S. Kamila, A. Ghosh and B. K. Jena, *Electrochim. Acta*, 2018, 263, 147–157.
 - 13 Y. Hua, Q. Xu, Y. Hu, H. Jiang and C. Li, *J. Energy Chem.*, 2019, 37, 1–6.
 - 14 D. Liang, C. Lian, Q. Xu, M. Liu, H. Liu, H. Jiang and C. Li, *Appl. Catal. B Environ.*, 2020, 268, 118417.
 - 15 Y. Chang, N. E. Shi, S. Zhao, D. Xu, C. Liu, Y. J. Tang, Z. Dai, Y. Q. Lan, M. Han and J. Bao, *ACS Appl. Mater. Interfaces*, 2016, 8, 22534–22544.
 - 16 P. Barpanda, M. Avdeev, C. D. Ling, J. Lu and A. Yamada, *Inorg. Chem.*, 2013, 52, 395–401.
 - 17 C. Chen, N. Zhang, Y. He, B. Liang, R. Ma and X. Liu, *ACS Appl. Mater. Interfaces*, 2016, 8, 23114–23121.
 - 18 K. M. S. Etheredge and S. J. Hwu, *Inorg. Chem.*, 1995, 34, 1495–1499.
 - 19 H. Du, W. Ai, Z. L. Zhao, Y. Chen, X. Xu, C. Zou, L. Wu, L. Su, K. Nan, T. Yu and C. M. Li, *Small*, 2018, 14, 1801068.
 - 20 H. J. Song, H. Yoon, B. Ju, D. Y. Lee and D. W. Kim, *ACS Catal.*, 2020, 10, 702–709.
 - 21 Q. Che, Q. Ma, J. Wang, Y. Zhu, R. Shi and P. Yang, *Mater. Lett.*, 2020, 272, 127877.
 - 22 L. Zhao, J. Li, P. Chen, G. Li, J. Yu and R. Xu, *Chem. Mater.*, 2008, 20, 17–19.
 - 23 M. K. Sahoo, A. K. Samantara and J. N. Behera, *Inorg. Chem.*, 2020, 59, 12252–

- 12262.
- 24 R. K. Tripathy, A. K. Samantara and J. N. Behera, *Sustain. Energy Fuels*, 2021, 5, 1184–1193.
- 25 M. Baril, H. Assaaoudi and I. S. Butler, *J. Mol. Struct.*, 2005, 751, 168–171.
- 26 E. Steger and B. Käßner, *Spectrochim. Acta Part A Mol. Spectrosc.*, 1968, 24, 447–456.
- 27 B. Li, R. Zhu, H. Xue, Q. Xu and H. Pang, *J. Colloid Interface Sci.*, 2020, 563, 328–335.
- 28 B. Boonchom and N. Phuvongpha, *Mater. Lett.*, 2009, 63, 1709–1711.
- 29 A. K. Samantara, S. Chandra Sahu, A. Ghosh and B. K. Jena, *J. Mater. Chem. A*, 2015, 3, 16961–16970.
- 30 M. A. Sayeed, T. Herd and A. P. O’Mullane, *J. Mater. Chem. A*, 2016, 4, 991–999.
- 31 L. Xu, Q. Jiang, Z. Xiao, X. Li, J. Huo, S. Wang and L. Dai, *Angew. Chemie*, 2016, 128, 5363–5367.
- 32 M. Liu, Z. Qu, D. Yin, X. Chen, Y. Zhang, Y. Guo and D. Xiao, *ChemElectroChem*, 2018, 5, 36–43.
- 33 M. T. Rinke and H. Eckert, *Phys. Chem. Chem. Phys.*, 2011, 13, 6552–6565.
- 34 H. Li, H. Yu, J. Zhai, L. Sun, H. Yang and S. Xie, *Mater. Lett.*, 2015, 152, 25–28.
- 35 H. Pang, Z. Yan, Y. Ma, G. Li, J. Chen, J. Zhang, W. Du and S. Li, *J. Solid State Electrochem.*, 2013, 17, 1383–1391.
- 36 H. Pang, S. Wang, W. Shao, S. Zhao, B. Yan, X. Li, S. Li, J. Chen and W. Du, *Nanoscale*, 2013, 5, 5752–5757.
- 37 Z. Khan, B. Senthilkumar, S. Lim, R. Shanker, Y. Kim and H. Ko, *Adv. Mater. Interfaces*, 2017, 4, 1700059.
- 38 R. Gond, D. K. Singh, M. Eswaramoorthy and P. Barpanda, *Angew. Chemie*, 2019, 58, 8330–8335.

CHAPTER-3

Boron doped carbon/cobalt pyrophosphate hybrid for high-performance all solid-state asymmetric supercapacitor device.

1.1 Abstract

1.2 Introduction

1.3 Experimental Section

1.3.1 Materials

1.3.2 Synthesis of Boron doped carbon/cobalt pyrophosphate hybrid (B-GC@CPP)

1.3.3 Synthesis of MXene

1.4 Characterization techniques

1.5 Electrode preparation and electrochemical measurements

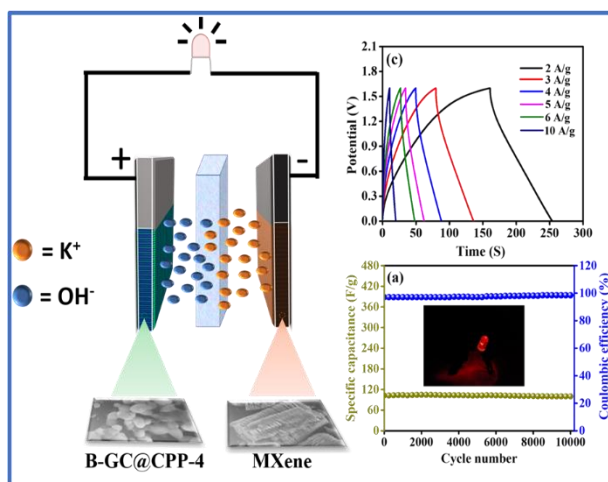
1.6 Fabrication of asymmetric supercapacitor cell

1.7 Results and Discussions

1.8 Conclusion

1.9 References

3.1 Abstract



Graphical Abstract

Incorporation of boron into the carbon matrix makes it an efficient candidate for supercapacitor application. Furthermore, excellent stability of cobalt pyrophosphate and the inherent redox behavior of cobalt provides an opportunity to synthesize boron doped carbon/cobalt pyrophosphate hybrid material. Herein, a two-step process is followed for the synthesis of boron doped carbon/cobalt pyrophosphate hybrid. Through appropriate adjustment of the amount of boron during synthesis, the electrochemical performance of a set of material were studied. The material synthesized with 4 mg of boron (B-GC@CPP-4) exhibits a specific capacitance of 395.1 F/g at 1.5 A/g mass normalized current density. However, the intrinsic hydrophilicity and metallic conductivity of MXene, makes it an eminent electroactive material to be used as a negative electrode. Owing to the above properties, all-solid-state asymmetric supercapacitor cell (ASC) was fabricated [B-GC@CPP-4//MXene] that exhibits a specific capacitance of 125 F/g with an energy density of 45 Wh/kg at a power density of 1735 W/kg at 2 A/g current density. The ASC device possesses an excellent coulombic efficiency of 98.5 % and capacitance retention of 96 % after 10000 consecutive charge/discharge cycles. The study reveals B-GC@CPP-4// MXene to be a promising set-up for energy storage devices.

3.2 Introduction

With the closer view to the world's ever-growing population and industrialisation, researchers throughout the globe are highly intended towards clean, renewable, green and sustainable energy sources.^{1,2} In addition to environmental pollution thriving dependency on pocket-sized and flexible devices for our comfortable life-style, batteries and supercapacitor-based devices are on huge demand. Supercapacitors bridging between batteries and dielectric capacitor, are responsible for delivering energy at higher rates along with retaining its specific power for long duration.^{3,4} Thus, knowledge of charge storage, electron and ion transport pathways provide an opportunity to enhance electrochemical active sites, conductivity and electrolyte accessible surface area of the materials which in turn make them feasible for practical applications.⁵

For several years RuO₂ used as an eminent supercapacitive material because of its large operating potential window and good reversibility, but the high cost and toxic nature hinders its wide practical application.^{6,7} Therefore alternative low-cost materials like MnO₂, Co₃O₄, Ni(OH)₂, Co(OH)₂, Co₉S₈, MoS₂, Ni₂P, NiB, etc. are preferred for encouraging electrochemical performance.⁸⁻¹⁵ Though these materials exhibit high specific capacitance, the intrinsic insulating behaviour results in low-rate capability and durability.^{16,17} In such a scenario, transition metal pyrophosphates have attracted substantial consideration as an electroactive material for electrochemical charge storage device due to their reversible redox behaviour, broad operating potential window and rigid layered structure.¹⁸ The rigid layered structure of transition metal pyrophosphate-based material is the reason behind the better rate capability and durability in harsh alkaline condition.¹⁹ Out of all these transition metal pyrophosphates, cobalt pyrophosphates having high theoretical capacitance of 1322 F g⁻¹ in 1 V potential window gained massive attention towards electrochemical storage devices. Pang *et al.* follows a simple two-step process; chemical precipitation along with calcination to synthesize Co₂P₂O₇. The as-synthesized Co₂P₂O₇ nano and microstructures projected a

specific capacitance of 367 F g^{-1} at a current density of 0.625 A/g in 0.4 V potential window.²⁰ Another group of researchers studied the effect of calcination temperature on the electrochemical performance of $\text{Co}_2\text{P}_2\text{O}_7/\text{C}$ hybrid and found that the material formed at a calcination temperature of $900 \text{ }^\circ\text{C}$ showed better cycling performance with a specific capacitance value of 349.6 F g^{-1} at a current density of 1 A/g in $0-0.5 \text{ V}$ potential window. An asymmetric supercapacitor cell (ASC) $3\text{DPG}/\text{Co}_2\text{P}_2\text{O}_7/\text{C}$ provides a specific capacitance of 70.1 F/g at 0.5 A/g current density. Furthermore, the ASC exhibit an energy density of 21.9 Wh/kg at the power density of 375 W/kg .²¹ A different approach, by taking $0.1 \text{ M } [\text{K}_3\text{Fe}(\text{CN})_6]$ as an electrolyte additive, Hyunhyub Ko *et al.* reported a specific capacitance value of 580 F/g at 1A/g current density for $\text{Co}_2\text{P}_2\text{O}_7$ nanosheet. Furthermore, the operating potential window for this system was 0.68 V and retention in specific capacitance was found out to be 96% after 5000 cycles of charge-discharge at 10 A/g current density.²² Liu *et al.* synthesised amorphous Co-Ni pyrophosphate which was used as a positive electrode and activated carbon as negative electrode for the fabrication of ASC. The as-fabricated ASC provides a followed to increase the conductivity along with the charge storage performance in a large potential window. Boron with an empty p-orbital makes a home for storing more charges. Additionally, boron is the nearest neighbour of carbon with almost comparable atomic radii and electronegativity, paves an obvious path for the formation of B-doped carbon with enhanced electrochemical activity.²⁴ There were several reports where incorporation of foreign element like boron enhances the electrochemical properties of carbonaceous materials. Rao *et al.* synthesised boron doped carbon nanotubes and graphene, which makes it p-type material.²⁵ This is because the band gap is apparently closed in boron doped carbonaceous material which develops a prominent acceptor like behaviour on the valence band side close to Fermi level.²⁶ Although various reports with the capacitive behaviour of the boron doped carbon-based materials were thoroughly studied,²⁷ but to the best of our knowledge there are no such reports where enhanced supercapacitive performance of the boron doped carbon/cobalt pyrophosphate hybrid is studied.

The supercapacitive performance of cobalt pyrophosphate in a large potential window a simple two-step synthetic process is proposed here, where boron doped partially graphitized carbon/cobalt pyrophosphate hybrid (B-GC@CPP) was successfully synthesized. The material formed with optimum quantity of boron powder, shows an excellent supercapacitive behaviour in comparison with the pristine GC-CPP. Furthermore, MXene (Ti_3C_2) as a negative electrode is used for the fabrication of MXene//B-GC@CPP-4 ASC. The high metallic conductivity along with the hydrophilicity of the MXene makes it an appropriate choice to be used as a negative electroactive material in ASCs.²⁸

Owing to the inherent properties of MXene and superior performance of the B-GC@CPP-4 all-solid-state asymmetric supercapacitor cells were fabricated using B-GC@CPP-4 as positive electrode and MXene (Ti_3C_2) as negative electrode. The fabricated ASCs exhibit a favourable specific capacitance 125 F/g along with superior cycling stability for its practical application. A facile two-step process is followed to synthesize the B-GC@CPP shows a superior supercapacitive performance in both three-electrode setup and as all-solid-state ASCs.

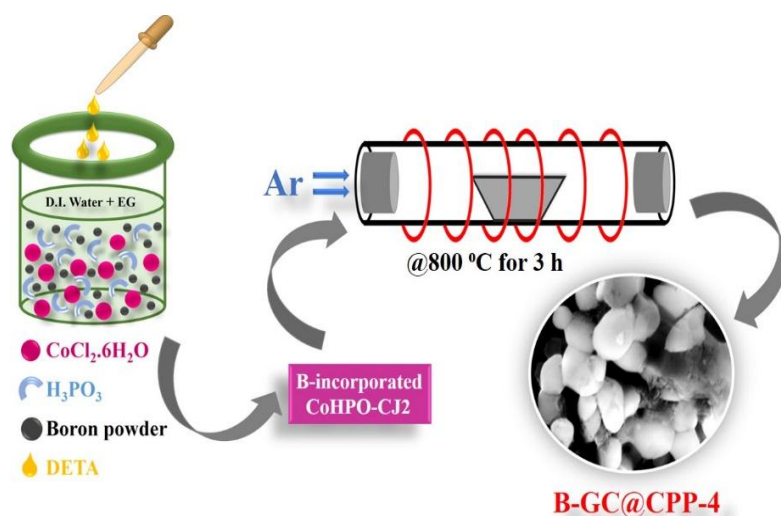
3.3 Experimental Section

3.3.1 Materials

$\text{CoCl}_2 \cdot 6\text{H}_2\text{O}$, phosphorous acid (H_3PO_3), ethylene glycol (EG), boron powder, dimethylformamide (DMF) and diethylenetriamine (DETA) were procured from Sigma- Aldrich, India and used as received. Ti_3AlC_2 (MAX phase) was purchased from carbon India, for the synthesis of Ti_3C_2 (MXene). Deionised water was used throughout all the synthetic pathway. The electrochemical analyses were carried out with freshly prepared electrolyte in deionised water.

3.3.2 Synthesis of Boron doped carbon/cobalt pyrophosphate hybrid (B-GC@CPP)

The synthesis of B-GC@CPP hybrid was carried out by a simple reaction pathway consisting of two steps. In the first step 0.238 g of $\text{CoCl}_2 \cdot 6\text{H}_2\text{O}$ was added to a mixture of solvents containing 1 ml of deionised water and 7 ml of ethylene glycol. To this mixture 0.164 g of phosphorous acid, boron powder was added. Then finally 0.1 ml of DETA (diethylenetriamine) was added to adjust the pH of the reaction in between 4-5. The reaction mixture was then agitated by vigorously stirring for 3 h at room temperature. The mixture was then transferred to a Teflon-lined stainless-steel autoclave and kept in an electric oven at $130\text{ }^\circ\text{C}$ for 72 h to form the precursor composite for the synthesis of B-GC@CPP hybrid. The composite produced in the first step was thoroughly washed with distilled water and dried in a vacuum oven for overnight. In the second step the products were calcined at $800\text{ }^\circ\text{C}$ in an inert atmosphere for 3 h to synthesize the desired B-GC (boron doped partially graphitized carbon) CPP (cobalt pyrophosphate) hybrid material, denoted as B-GC@CPP. The quantity of boron powder was also varied as 2, 4 and 8 mg during synthesis, those are denoted as B-GC@CPP-2, B-GC@CPP-4 and B-GC@CPP-8 respectively. The material without boron was also synthesized by utilizing the same synthetic protocol. Without boron the material formed in the first step was $(\text{H}_3\text{O})_2 \cdot [\text{Co}_8(\text{HPO}_3)_9(\text{CH}_3\text{OH})_3] \cdot 2\text{H}_2\text{O}$ open-framework²⁹ and then calcined at $800\text{ }^\circ\text{C}$ in inert atmosphere to produce GC@CPP as presented in scheme 3.1.



Scheme 3.1 Schematic representation for the synthesis of B-GC@CPP

3.3.3 Synthesis of MXene

A simple aluminium etching process in MAX (Ti_3AlC_2) was followed to synthesize MXene as per a published report.³⁰ 0.5 g of MAX powder was gradually added to 10 ml of 30 % HF at room temperature with constant stirring. Stirring was continued for 10 h for complete etching of Al. The sample obtained after 10 h of constant stirring was centrifuged repeatedly till the pH of the supernatant becomes neutral. Then the obtained powder was dried at 70 °C for further use. The morphology of MAX and MXene (after aluminium etching) can be clearly observed from Figure 3.1.

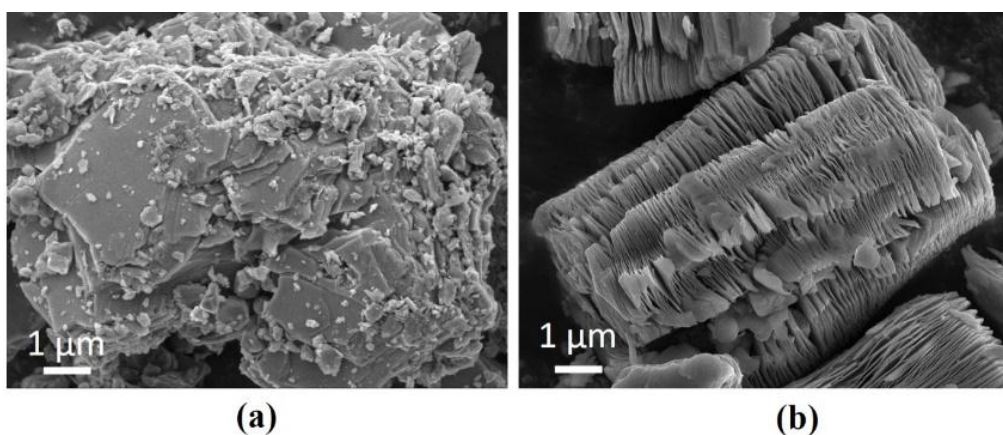


Figure 3.1 FESEM images of (a) MAX (Ti_3AlC_2) and (b) MXene (Ti_3C_2).

3.4 Characterization Techniques

Bruker D8 Advance diffractometer was employed to obtain powder XRD data, in order to explore the phase purity, crystallinity and presence of dopant molecule in the samples. The diffractometer is equipped with Cu K_α radiation with wavelength (λ) 1.5418 Å and a diffractometer monochromator operated at a voltage of 40 kV and a current of 40 mA. Raman analyser (Horiba Scientific) with laser wavelength of 532 nm used to record Raman spectrum that enables us to know about nature of the carbon before and after boron incorporation. The morphological examination was carried out by FESEM (Merlin Compact with GEMINI-I electron column, Zeiss Pvt. Ltd., Germany), TEM and HRTEM (HRTEM, JEOL JEM 2100F, with an accelerating voltage of 200 kV). For transmission electron microscopy analysis of the material, a carbon coated copper grid was drop casted with the well dispersed sample in deionized

water and was thoroughly dried under xenon lamp prior to microscopic study. The weight % of boron present in the synthesized compound is verified by using an inductively coupled plasma optical emission spectrophotometer (iCAP 7000 ICP-OES). The nature bonding in $\text{Co}_2\text{P}_2\text{O}_7$, surface analysis of elements and elemental composition of the samples were analysed by X-ray photoelectron spectroscopy (PHI Versa Probe II).

3.5 Electrode preparation and electrochemical measurements

The electroactive working electrode was prepared by thoroughly mixing the synthesised material (GC@CPP, B-GC@CPP-2, B-GC@CPP-4 or B-GC@CPP-8), acetylene black (as conductive additive) and PVDF as binder in weight % ratio of 80:10:10 respectively. These materials were intensively ground with the help of a mortar pestle with a minimum quantity of DMF to have a thick slurry. Graphite sheet having dimension $1\text{ cm} \times 1\text{ cm}$ was coated with the as prepared slurry using a doctor blade and the active material loading was found out to be 1.7 mg/cm^2 , which was further used during electrochemical study. All the electrochemical analyses (e.g., CV, charge-discharge, cyclic performance, cycle stability, electrochemical impedance spectroscopy) of the half-cell were carried out with Biologic - SP200 potentiostat using Pt wire as counter electrode, Hg/HgO as reference electrode and the as prepared graphite sheet-based electrode (with dimension $1\text{ cm} \times 1\text{ cm}$) as working electrode. The half-cell electrochemical studies were carried out in freshly prepared 3 M KOH, due to the reason that size of K^+ and OH^- in aqueous medium is 3.31 \AA and 3.0 \AA . Moreover, K^+ with the highest ionic conductivity among all cations after H_3O^+ and OH^- having the highest ionic conductivity among all anions.³¹

3.6 Fabrication of asymmetric supercapacitor cell

The ASCs was fabricated by taking B-GC@CPP-4 as positive electrode, as-prepared MXene used as negative electrode and a Whatmann filter paper was used as a separator. The electrochemical analysis of the ASCs was carried out by using PVA/KOH gel

electrolyte (for all solid-state ASCs). Charge balance (i.e., $q^+ = q^-$) of both the electrodes were essential to get best performance out of the ASC device, hence the active material loading on both the electrodes were calculated as per the equation; $m^+/m^- = (C^- \times \Delta V^-)/(C^+ \times \Delta V^+)$ and mass ratio was found out to be 0.88. C^- and C^+ are the specific capacitance of MXene and B-GC@CPP-4 at 40 mV/s whereas ΔV^- and ΔV^+ are the operating potential window for MXene and B-GC@CPP-4.

3.7 Results and discussions

Figure 3.2 (a) represents the typical Raman spectra of the sample before and after boron incorporation. The Raman shift value for both GC@CPP B-GC@CPP-4 at the wavenumber 1040.3 cm^{-1} and 723.2 cm^{-1} is observed due to the strong symmetric vibrations of the PO_3 group and P-O-P bridge respectively.¹⁹ The D-band and G-band are located at 1347 cm^{-1} and 1589 cm^{-1} signifies the presence of disordered and graphitic characteristics of the carbonaceous material.³² The degree of disorder ness in the graphitic structure of the carbonaceous materials is evaluated form the intensity ratio of D-band and G-band (I_D/I_G) ratio. In this work the ratio (I_D/I_G) is found out to be 1.04 suggesting the presence of partially graphitized carbon.³³ As D-band is sensitive to doping [shown in Figure 3.2 (a)], intensity of the D-band of B-GC@CPP is slightly higher than that of GC@CPP.²⁶ The phase purity and presence of B-GC@CPP-4 was inferred from the powder XRD pattern Figure 3.2 (b). The sharp reflections completely match with the PDF file no. 00-034-1378. The XRD pattern reveals the monoclinic phase of the as synthesised material with lattice parameter $a = 13.248 \text{ \AA}$, $b = 8.345 \text{ \AA}$, $c = 9.004 \text{ \AA}$ and P21/c space group. The position of the two intense peaks at 29.73° and 30.22° corresponding to the lattice planes (022) and $(40\bar{2})$ respectively remains same for both GC@CPP and B-GC@CPP-4. The position of other less intense peaks corresponds to $(11\bar{3})$, (420), (232), $(42\bar{4})$ also remain intact after incorporation of boron into the carbon lattice.

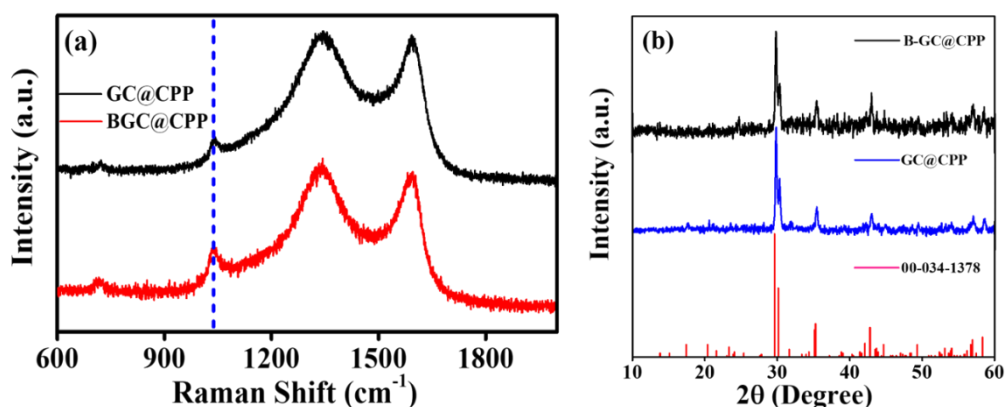


Figure 3.2 (a) Raman spectra (b) PXRD patterns of GC@CPP and B-GC@CPP-4

XPS was carried out to further analyse the chemical composition and explore the chemical bonding state of the elements present in the as synthesised material. Nature of boron i.e., it's interaction with carbon in the B-GC@CPP-4 was also analysed by XPS. XPS survey spectra in Figure 3.3 (a) provides the information related to presence of boron (190.8 eV) signifying the successful incorporation of boron atom inside carbon lattice. Except these the prominent peaks at 283.7 eV and 531.4 eV describes the presence of carbon and oxygen.³⁴ Fine spectra of the elements present in the active material were clearly shown in Figure 3.3 (b-f). The fine spectra for B 1s shown in Figure 3.3 (b) describes three peaks centred at 189.9, 191.5 and 193.1 eV correspond to the BCO_2 , BC_2O and BC_3 respectively. Boron atoms observed in the form of BCO_2 , BC_2O , BC_3 by substituting a carbon atom by a boron atom without damaging the carbon skeleton.³⁵ The peak centred at 284.8 eV in Figure 3.3 (c) is due to the presence of $\text{C}=\text{C}$ of partially graphitized sp^2 carbon. Except that the position of peak at 283.3 eV describes the presence $\text{C}-\text{B}$ bond and the peak positioned at 287.4 eV due to the presence of $\text{C}=\text{O}$ bond in the carbon layer.³⁶ In Figure 3.3 (d) the peaks at 782.3 and 798 denote the characteristic peaks for $\text{Co } 2p_{3/2}$ and $\text{Co } 2p_{1/2}$, were accompanied by two satellites at 785.4 eV and 802.4 eV respectively. The binding energy 133.8 and 134.7 eV in Figure 3.3 (e) correspond to the $\text{P}=\text{O}$ and $\text{P}-\text{O}$ in $\text{Co}_2\text{P}_2\text{O}_7$. Similarly, in Figure 3.3 (f) O1s XPS spectra, the peaks cantered at 531.8 correspond to the presence of $\text{P}=\text{O}$ or $\text{C}=\text{O}$ bonds. Along with this the peak at 533.6 signifies the presence of $\text{P}-\text{O}-\text{P}$ symmetric bridging oxygen.^{21,37-39}

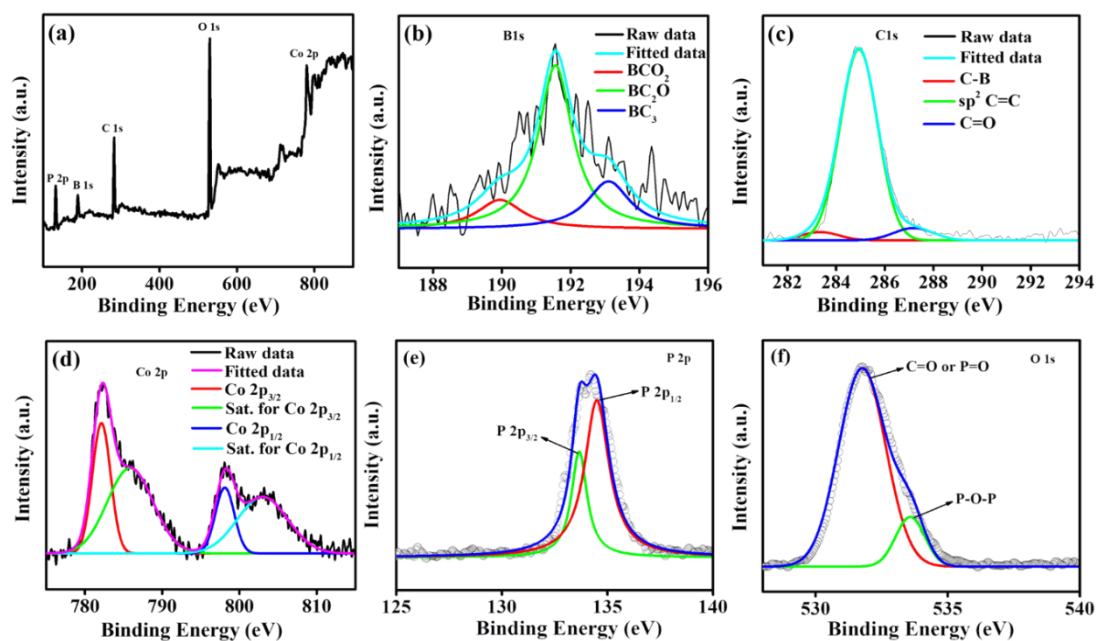


Figure 3.3 (a) Full-range survey spectra of B-C@CPP-4. (b)–(f) Fine spectra of B 1s, C 1s, Co 2p, P 2p and O 1s, respectively.

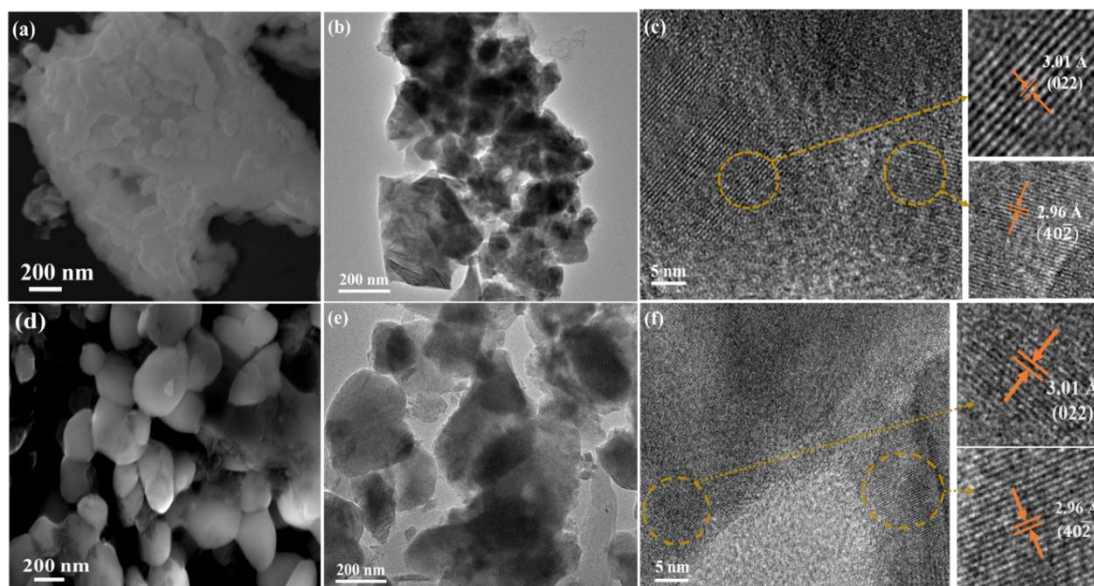


Figure 3.4 (a) and (d) FESEM, (b), (e) and (c), (f) TEM and HRTEM images of GC@CPP and B-GC@CPP-4 respectively.

SEM images at lower magnification in Figure 3.4 (a) showed irregular distribution and agglomerated morphologies of the GC@CPP. The agglomeration might arise due to high temperature calcination of the precursors. The agglomeration was reduced up to some extent with boron incorporation within the carbon network as presented in Figure 3.4 (d). Figure 3.5 represents the gradual reduction in agglomeration with increase in boron quantity. Figure 3.4 (b) and (e) represents the TEM images of GC@CPP and B-GC@CPP-4 respectively, which were in good agreement with the SEM images of the as synthesised materials. The HRTEM images in Figure 3 (c) and (f) were used to calculate the fringe width of the designated material and was found out to be 3.01 Å along (022) plane and 2.96 Å along (40 $\bar{2}$) plane for both GC@CPP and B-GC@CPP.

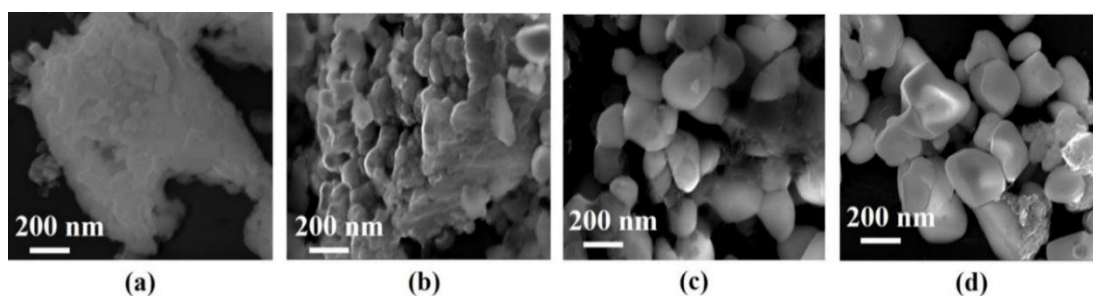
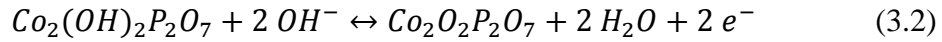
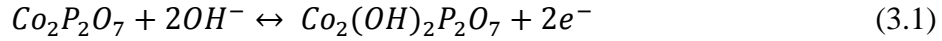


Figure 3.5 SEM images of B-GC@CPP with varying boron quantity from 0 to 8 mg (0, 2, 4, 8mg)

GC@CPP selected as active material, coated over graphite sheet was designated as working electrode. The capacitive behaviour of the active material was explored in 3 M KOH and within a potential window of 0.75 V (-0.20 to 0.55 V) with respect to Hg/HgO reference electrode. Nature of GC@CPP towards supercapacitive activity was examined from CV curves at various scan rates (Fig. 3.6 (a)). Shape of the CV curves along with prominent redox peaks represent the existence of both EDLC and pseudocapacitive behaviour owing to the presence of partially graphitized carbon and CPP respectively. With increase in the scan rate, cyclic voltammograms exhibit an increase in redox current along with peak shifts. This indicates that rapid transport of electron and ion occur at higher scan rate.⁴⁰ The current response in the CV curve with respect to the scan rate were addressed to its kinetic limitations, as at higher scan rate there occurs only surface electrochemical reaction whereas at lower scan rate results in bulk electrochemical reaction. Thus, electrolyte access to the interior of the material is

diminished at higher scan rate due to insufficient interaction time. Two noticeable redox peaks are due to the reversible reaction of Co(II) \leftrightarrow Co(III) and Co(III) \leftrightarrow Co(IV).⁴¹ The Faradaic reaction for Co₂P₂O₇ can be expressed by the following plausible reaction mechanism.



Charge storage mechanism is calculated quantitatively by the following relation between current (i) and scan rate (v).

$$i = av^b \quad (3.3)$$

In this relation a and b are constants, can be evaluated from the plot between $\log(i)$ vs. $\log(v)$. The slope from this plot gives the value of b which usually 0.5 or 1.0. Value of $b = 0.5$ represents the charge storage mechanism goes through diffusion-controlled process, whereas when the value of $b = 1.0$, the charge storage mechanism is surface controlled.^{42,43} The cathodic peaks were considered to study the plot between $\log(i)$ vs. $\log(v)$ shown in Figure 3.6 (b). The b value for this particular material is found out to be 0.75 inclined towards 1.0 suggests that the mechanism of charge storage is surface controlled not diffusion controlled.

Galvanostatic charge-discharge was carried out at different mass normalized current densities from 1.5 A/g to 9.0 A/g for all the materials in three electrode set-ups. The following equation is used to evaluate the specific capacitance value of the material.⁴⁴⁻

46

$$C_{sp} = I_m / (dV/dt) \quad (3.4)$$

The symbols I_m and dV/dt refers to the mass normalized current density (applied current / mass of the active material) and slope of the discharge curve at a particular current density respectively. Figure 3.6 (c) represents the charge–discharge curve within 1.5 to 7.5 A/g current density range. The specific capacitance value of 230 F/g at 1.5 A/g was calculated using equation (3.4). At different current densities the specific capacitance values were calculated in 0.75 V potential window [shown in Fig. 3.6 (d)].

The value of specific energy and specific power was calculated from the obtained specific capacitance. In three electrode system GC@CPP delivers a specific energy of 17.18 Wh/kg at a specific power of 801.2 W/kg, was calculated utilizing the following equations³¹ (3.5) and (3.6).

$$\text{Energy density (E.D)} = C_{sp} \times (\Delta V)^2 / 7.2 \quad (3.5)$$

$$\text{Power density (P.D)} = (E.D \times 3600) / \Delta t \quad (3.6)$$

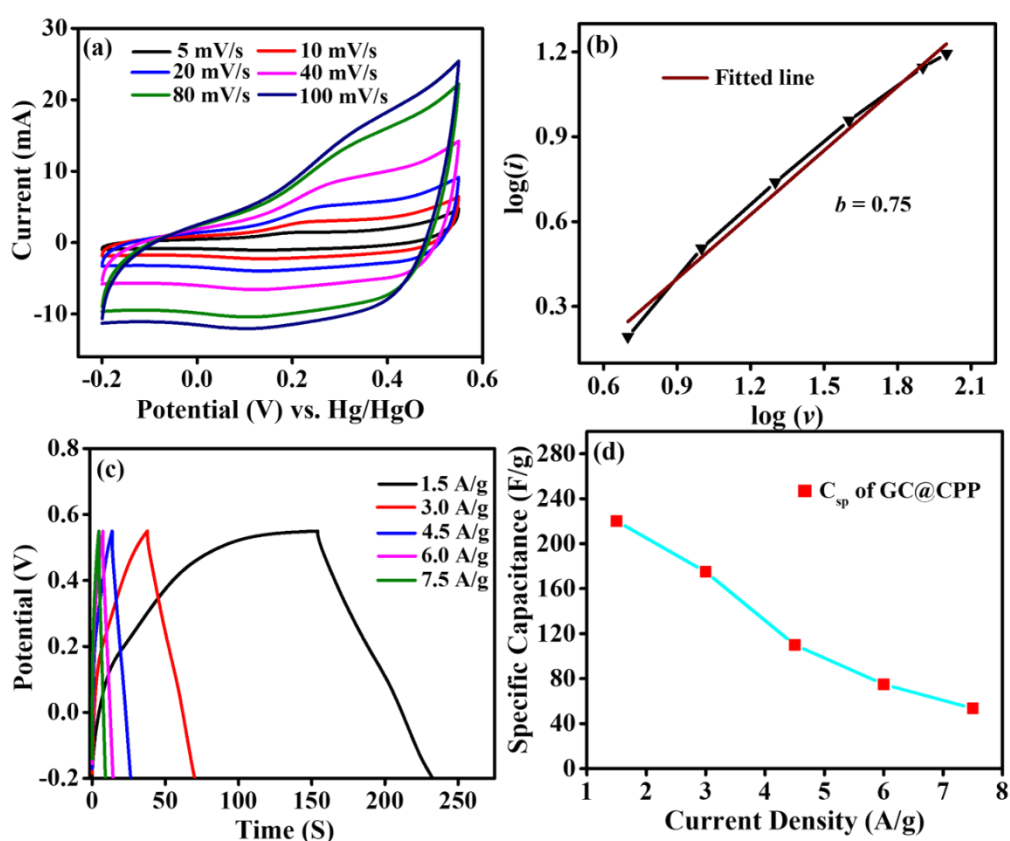


Figure 3.6 (a) CVs at different scan rates, (b) $\log(i)$ vs. $\log(v)$, (c) GCD curves at different current densities. (d) C_{sp} at various current densities.

Although the GC@CPP provides an appreciable specific capacitance and cycling stability by virtue of its rigid layered structure and reversible redox behaviour but the low specific capacitance, energy density and power density need to be addressed. Presence of boron in the carbon matrix leads to fast electron acceptance rate thereby showing ultrafast charge storage kinetics.³⁵ Boron having one electron less than carbon introduces a hole charge carrier after incorporated into the carbon lattice, further enhances the EDLC behaviour in the carbonaceous material by increasing charge

density and DOS (density of states).⁴⁷ Formation of boron doped carbon/cobalt pyrophosphate hybrid is a novel approach to further enhance the pseudocapacitive behaviour of cobalt pyrophosphate. As represented in Figure 3.7 (a) firstly, the electrochemical performance was studied at 5 mV/s for all the three (B-GC@CPP-2, B-GC@CPP-4 and B-GC@CPP-8) materials. Among these B-GC@CPP-4 formed with 4 mg of boron powder having largest CV area illustrates the highest electrochemical capacitance value. In all the CV curves, small but broad redox peaks were observed at ≈ 0.010 V, due to the presence of boron in the carbon skeleton. The capacitive performance of all the above mentioned three materials was evaluated from the GCD curves in Figure 3.7 (b) operated at a current density of 1.5 A/g within a potential window 0.75 V (-0.2 to 0.55). The specific capacitance values obtained from GCD curves operated at 1.5 A/g were shown in Figure 3.7 (c). Specific capacitance values of 312, 395.1 and 344 F/g obtained for B-GC@CPP-2, B-GC@CPP-4 and B-GC@CPP-8 respectively. B-GC@CPP-4 shows highest specific capacitance compared to B-GC@CPP-2 and B-GC@CPP-8. Additionally, the actual content of boron present in the compound is calculated using inductively coupled plasma optical emission spectroscopy (ICP-OES) measurements. The weight percentage of boron in B-GC@CPP-2, B-GC@CPP-4 and B-GC@CPP-8 varies in between 3.8 to 9.6 weight % with varying the quantity of boron powder during synthesis. It can be inferred that the material with 6.4 weight % of boron in the hybrid (B-GC@CPP-4), possess superior electrochemical activity.

To find out the plausible explanation, the electrochemical impedance spectroscopy for all the samples were carried out within an AC frequency range of 100 kHz to 100 mHz with an AC amplitude of 5 mV at completely discharged state (Fig. 3.7 (d)). The slope of the impedance plot of B-GC@CPP-4 at low frequency region shows a much steeper rise than that of the other materials corresponding to the better capacitive behaviour of the B-GC@CPP-4. On the other hand, the equivalent series resistance (R_s) was found out to be 1.84, 2.38, 1.72 and 2.08 Ω for GC@CPP, B-GC@CPP-2, B-GC@CPP-4 and B-GC@CPP-8 respectively. The least R_s value (1.72 Ω) of the B-GC@CPP-4 suggests the favourable path for fastest ion diffusion and transport. These studies support the tuned capacitive performance of the rationally designed material (B-GC@CPP).

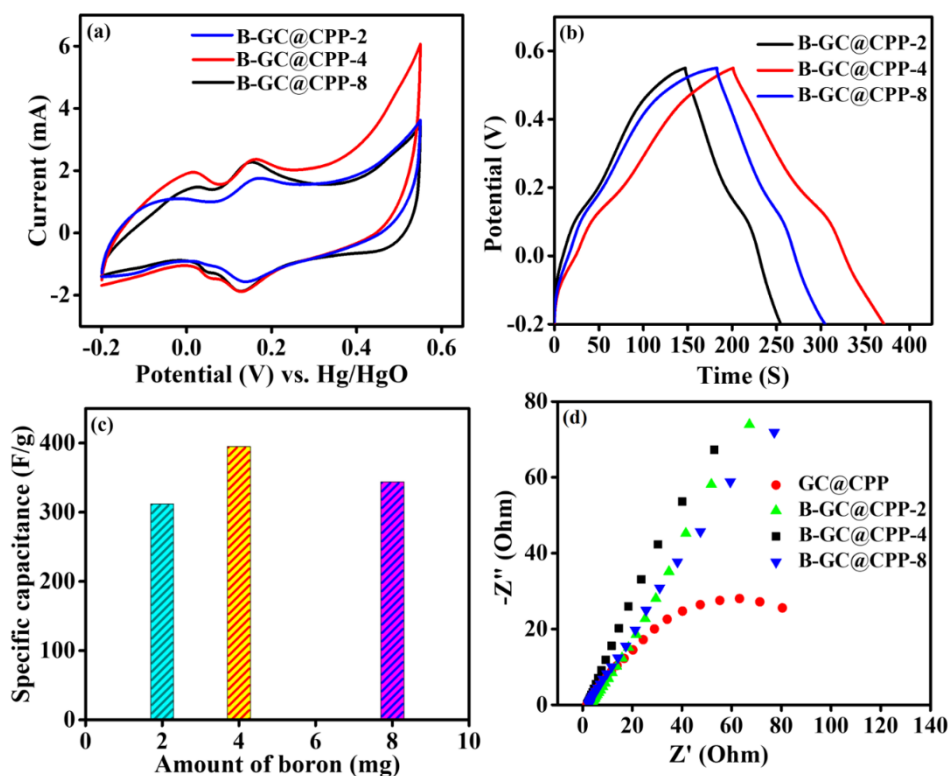


Figure 3.7 (a) CV at 5 mV/s and (b) GCD at 1.5 A/g for B-GC@CPP with varying Boron quantity (c) C_{sp} values at 1.5 A/g with varying boron quantities, (d) EIS

The CV curves for B-GC@CPP-4 with a scan rate ranging from 5 to 100 mV/s in 0.75 V potential window (-0.2 V to 0.55 V) were shown in Figure 3.8 (a). Expansion in the CV curves were observed with increase in scan rate. However, the redox peaks for cobalt pyrophosphate are still prominent with slight shift in the oxidation and reduction peak position towards more positive and negative potentials suggesting the stability of the material with higher scan rate. The mechanism of charge storage was further evaluated from the cathodic peak values at a particular potential. The slope (provides the value of b) of the plot between $\log(i)$ Vs. $\log(v)$ in Figure 3.8 (b) was found out to be 0.83 for B-GC@CPP-4 that is more than that of pristine GC@CPP. This indicates the dominance of surface-controlled process due to incorporation of boron. These analyses clearly imply the performance has been improved by utilization of optimized amount of boron powder addition during synthesis.

A set of mass normalized current densities ranging from 1.5 A/g to 9 A/g applied to get the desired GCD curves. These GCD profiles represented in Figure 3.8 (c) is for B-

GC@CPP-4. Almost symmetric nature of the curves for all the GCD profiles representing the redox capacitive behaviour of the materials. A curve between Specific capacitance values vs. current density for B-GC@CPP-4 were represented in Figure 3.8 (d).

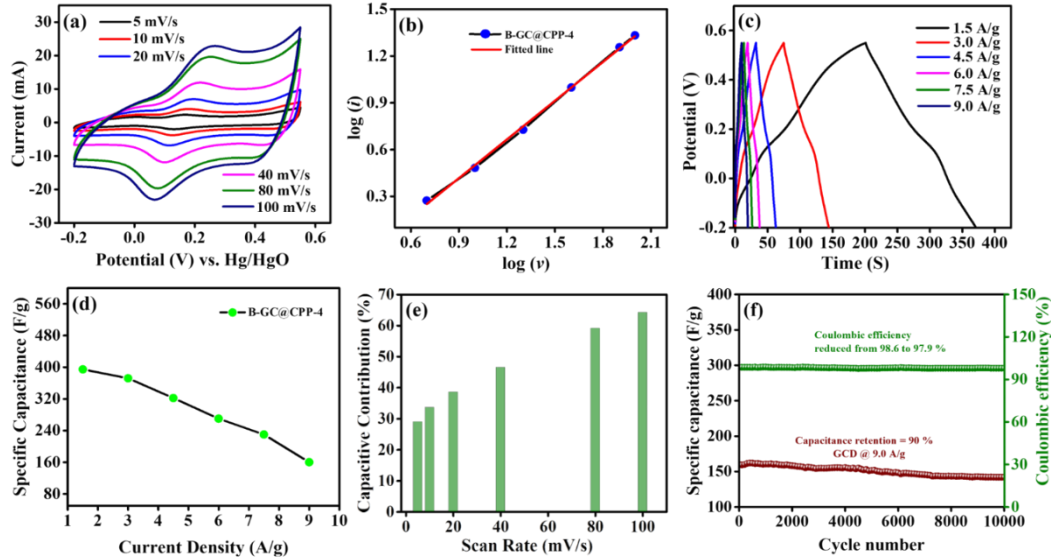


Figure 3.8 (a) CV, (b) $\log(i)$ vs. $\log(v)$, (c) GCD, (d) C_{sp} values, (e) capacitive contribution, (f) stability & coulombic efficiency

A specific capacitance value of 395.1 F/g was evaluated at a current density of 1.5 A/g which is further reduced to 160.8 F/g at 9.0 A/g with a rate capability of 41%. With increase in current density there occurs an obvious decrease in specific capacitance value as at high current density electrolyte ions have very short time for diffusion. Hence only surface electrochemical reaction occurs at high current density resulting in lower value of specific capacitance. Whereas, at lower current density electrolyte ions have much more time to diffuse into the inner part of the active material. Thus, the entire electroactive material takes part in electrochemical reaction providing higher specific capacitance values.^{50,51} Furthermore, the current response at a particular scan rate is employed for the quantitative analysis of the charge storage contribution using the following equation.^{52,53}

$$i(V) = k_1v + k_2v^{1/2} \quad (3.7)$$

k_1v and $k_2v^{1/2}$ correspond to the current contributions from the surface capacitive effects and the diffusion-controlled process, respectively. Figure 3.8 (e) represents the surface capacitive current contribution calculated using the above equation. The surface

capacitive contribution is predominated at higher scan rate whereas diffusion-controlled process is predominated at lower scan rate. At high scan rate of 100 mV/s the surface capacitive contribution is around 63 % whereas at lower scan rate of 5 mV/s the surface capacitive contribution is only 29 %.

Cyclic stability of the material was carried out at 9.0 A/g and the specific capacitance retention was calculated as 90 % whereas the retention in coulombic efficiency was found out to be 97.9 % after 10000 charge–discharge cycles as shown in Figure 3.8 (f). By virtue of rigid layered structure and self-healing behaviour of $\text{Co}_2\text{P}_2\text{O}_7$ provides high stability when operated in alkaline media for a long duration of time. Furthermore, the presence of boron that alters the electronic structure of carbon introducing defect in the carbon lattice and causes faster charge transportation. Both these effects synergistically affect the electrochemical performance of B-GC@CPP-4 in terms of excellent cyclic stability.^{35,54} This small decay in the specific capacitance and coulombic efficiency, suggests no parasitic reaction during the electrochemical process.

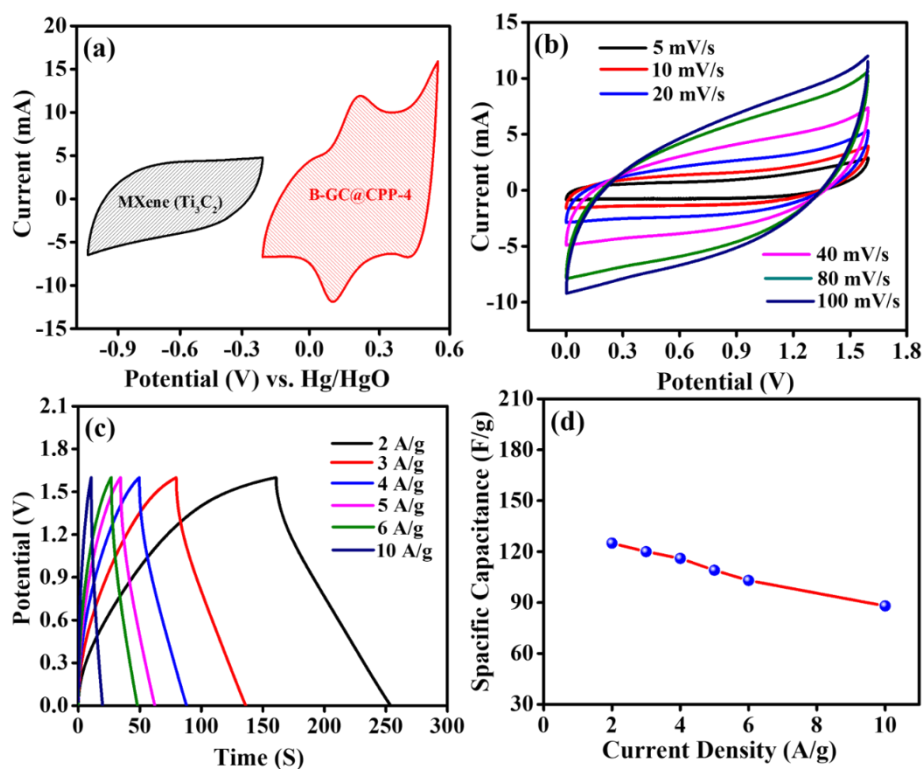
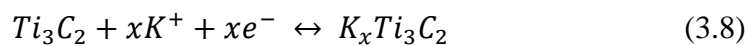


Figure 3.9 (a) CV of MXene and B-GC@CPP-4 at 40 mV s⁻¹ (b) CV and (c) GCD curves of ASC device (d) C_{sp} values at different current densities.

The above results of B-GC@CPP-4 are beneficial for the fabrication of an asymmetric device with higher specific capacitance (gravimetric), energy density and power density

reported till date for cobalt pyrophosphate-based material. The ASCs was fabricated by taking B-GC@CPP-4 as positive electrode, the as synthesized MXene (Ti_3C_2) as negative electrode and a Whatmann filter paper was used as a separator. MXenes possess high metallic conductivity, packing density and redox chemistry.⁵⁵ Along with this the excellent electrical conductivity, surface hydrophilicity, electrochemical stability and reversible intercalation of cations (such as H^+ , Li^+ , Na^+ , K^+ , and Mg^{2+}) makes it an attractive choice to be used as a negative electro active material for the fabrication of high performance asymmetric device.⁵⁶ The reversible intercalation/deintercalation of cations during the charge/discharge process in the layered MXene is represented as the following reaction.^{57,58}



The electrochemical analysis of the asymmetric device was carried out by using gel electrolyte (for all solid-state ASCs). Combined CV profiles of MXene (-1.05V to -0.2V) and B-GC@CPP-4 (-0.2V to 0.55V) at 40 mV/s shown in Figure 3.9 (a) generate a large potential window of 1.6 V. The CV profiles of ASC device were recorded in 0 to 1.6 V potential at a scan rate from 5 mV/s to 100 mV/s. There occurs no notable change in the CV curves with increasing the scan rate from 5 mV/s to 100 mV/s as can be seen in Figure 3.9 (b). This indicates the appreciable reversibility and outstanding rate capability of the fabricated ASC device. The GCD profiles operated from 2 A/g to 10 A/g in Figure 3.9 (c) were used to calculate the gravimetric specific capacitance of the ASC device. The specific capacitance value of 125 F/g was obtained at a current density of 2 A/g which was gradually decreased to 88 F/g at a current density of 10 A/g. Specific capacitance vs. current density curve in Figure 3.9 (d) illustrates the values of specific capacitances at different current densities of the all-solid-state asymmetric device.

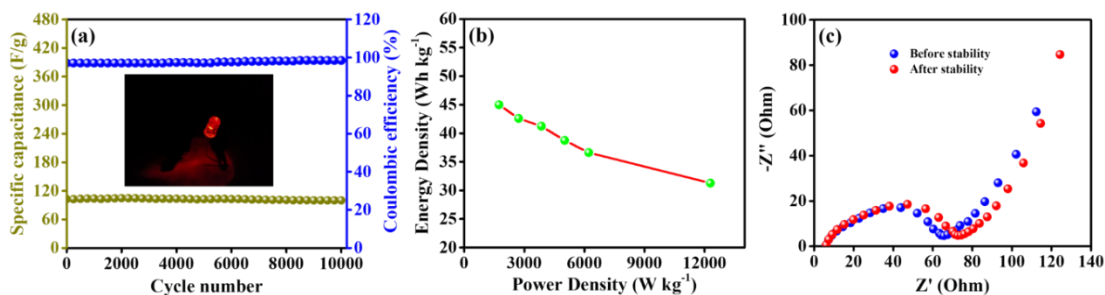


Figure 3.10 (a) Cyclic stability of the ASCs, (b) Ragone of the ASC device. (c) EIS of the ASC before and after stability

Cycling performance of the all-solid-state asymmetric device was carried out at a current density of 6 A/g was shown in Figure 3.10 (a). It was evaluated that after 10,000 cycles of constant galvanostatic charge-discharge, the retention in specific capacitance is almost 96 % and coulombic efficiency was retained almost 98.5 %, indicating excellent stability of the ASC. The specific energy and power were evaluated by using equation (3.5) and (3.6) and represented by Ragone plot in Figure 3.10 (b). An energy density of 45 Wh kg^{-1} at a power density of 1735 W kg^{-1} was evaluated at 2 A/g current density. With increase in current density value upto 10 A/g, the value of specific energy was reduced whereas a consistent increment in the value of power density was observed. At 10 A/g mass normalized current density the specific energy of the material still maintained 31.3 Wh kg^{-1} at a power density of $12,293 \text{ W kg}^{-1}$. Figure 3.10 (c) represents the impedance spectroscopy curve of the device before and after 10,000 GCD cycles. After cycling stability of the ASCs there is a negligible increase in both the equivalent series resistance and charge transfer resistance of the material. These small change in the impedance value indicates the good stability and enhanced electrochemical performance of the device. Comparatively, electrochemical performance of the ASC was superior to the previously reported cobalt phosphate-based materials, listed in Table 3.1. Potential application of this all-solid-state ASCs was demonstrated by using this ASC to lighten up a light emitting diode (LED) shown in the inset of Figure 3.10 (a). The GCD profile and SEM images before and after 10,000 GCD cycles was mentioned in Figure 3.11 suggesting the slight increase in IR drop and minimal decrease in specific capacitance value due to surface etching of the material in alkaline media. Looking into the electrochemical performances studied above, MXene//B-GC@CPP-4 is an ideal choice to fabricate a considerable low cost and stable energy storage device.

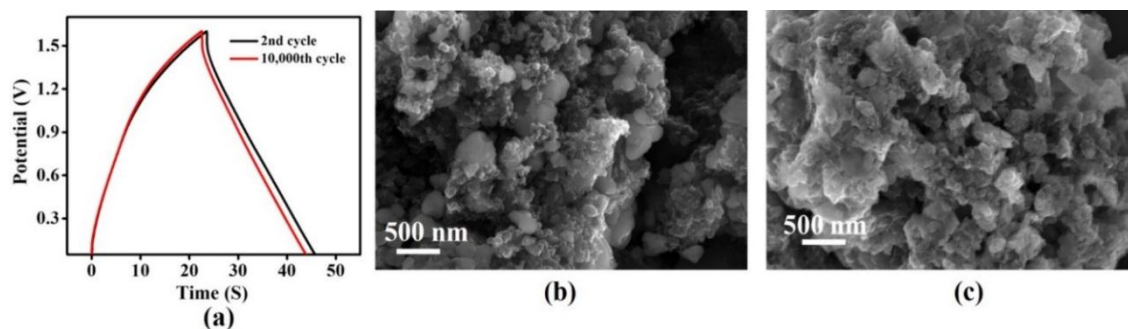


Figure 3.11 (a) GCD profiles of the ASC before and after 10,000th cycle, SEM image of B-GC@CPP-4 along-with acetylene black and PVDF (b) before cycling (c) after cycling.

3.8 Conclusion

In a nutshell, the boron doped carbon/cobalt pyrophosphate was successfully synthesized through facile hydrothermal followed by calcination at high temperature. Variable quantity of boron powder was used during hydrothermal process and the compound formed with 6.4 weight % of boron (B-GC@CPP-4) reveals superior electrochemical capacitive behaviour. B-GC@CPP-4 provides a specific capacitance value of 395.1 F/g at 1.5 A/g current density in 0.75 V potential window and showed a specific capacitance retention of 90 % after 10,000 GCD cycles in three electrode system. The MXene//B-GC@CPP-4 ASC device provides a specific capacitance value of 125 F/g at mass normalized current density of 2 A/g. This device maintained a maximum energy density of 45 Wh kg⁻¹ and power density of 12,293 W kg⁻¹. Retention in specific capacitance and coulombic efficiency of the device was evaluated to be 96 % and 98.5 % respectively after 10,000 consecutive galvanostatic charge-discharge cycles. The admirable capacitive performance of the device is mainly due to synergistic effect of boron doped carbon/cobalt pyrophosphate hybrid as positive active material and Ti₃C₂ (MXene) as negative active material, that greatly enhances charge storage performance of the device. The above study paves a path for the construction of a potentially reliable transition metal pyrophosphate based all-solid-state asymmetric supercapacitor device.

Table 3.1 Comparison table for phosphate-based material showing supercapacitor behaviour

Name	Specific Capacitance	Potential window	Sp. cap. of ASC	Energy density	Power density	Capacitance retention & Cycle No.s	Ref.
Flower like 3D Co ₃ (PO ₄) ₂ .8H ₂ O	350 F/g at 1A/g (3 M KOH)	0 – 0.42 V	-	-	-	102% retention after 1000 cycles	<i>Mater. Lett.</i> , 2015, 152 , 25–28
Binder free 1D Co ₃ (PO ₄) ₂ nanograss	12,285 mF/cm ² at 5 mV/s (1 M KOH)	0 – 0.7 V	85 F/g at 1A/g	26.66 Wh/kg	750 W/kg	80% retention after 6000 cycles (Device)	<i>J. Power Sources</i> , 2018, 373 , 211–219.
Co ₂ P ₂ O ₇ nano/microstructu	367.2 F/g at 0.625	0 – 0.4 V	-	-	-	96.2% retention	<i>J. Solid State Electroche</i>

res	A/g (3 M KOH)					after 3000 cycles	<i>m.</i> , 2013, 17 , 1383–1391.
CoHPO ₄ .3H ₂ O ultrathin nanosheets	413 F/g at 1.5 A/g (3 M KOH)	0 – 0.45 V	-	-	-	>85.1% retention after 3000 cycles	<i>Nanoscale</i> , 2013, 5 , 5752–5757.
1D Co ₂ P ₂ O ₇ nanorods	483 F/g at 1 A/g (3 M KOH)	-0.1 – 0.45 V	-	-	-	90% retention after 3000 cycles	<i>RSC Adv.</i> , 2013, 3 , 21558–21562.
Amorphous Co _{0.2} Ni _{0.8} polyphosphate	1259 F/g at 1.5 A/g (3 M KOH)	0 – 0.55 V	119 F/g at 1 A/g	42.4 Wh/kg	800 W/kg	80% retention after 2000 cycles (Device)	<i>ACS Appl. Mater. Interfaces</i> , 2016, 8 , 23114–23121.
Ni ₃ P ₂ O ₈ - Co ₃ P ₂ O ₈ .8H ₂ O	1974 F/g at 0.5 A/g (6 M KOH)	0 – 0.4 V	94 F/g at 0.5 A/g	33.4 Wh/kg	399 W/kg	83% retention after 5000 cycles (Device)	<i>Electrochim. Acta</i> , 2016, 201 , 142–150.
Co ₂ P ₂ O ₇ Nanosheets	580 F/g at 1 A/g in 0.1 M KFC (K ₃ Fe(CN) ₆) in 3 M KOH	-0.2 – 0.48 V	-	-	-	96% retention upto 5000 cycles	<i>Adv. Mater. Interfaces</i> , 2017, 4 , 1700059.
Nanoporous Nickel phosphate	265 F/g at 20 mV/s (3 M KOH)	0 – 0.5 V	-	-	-	97% retention after 1000 cycles	<i>ACS Appl. Mater. Interfaces</i> , 2016, 8 , 9790–9797.
Co _{0.4} Ni _{1.6} P ₂ O ₇ /N-doped graphene (NG) composites	1473 F/g at 1 A/g (3 M KOH)	0 – 0.55 V	-	34.9 Wh/kg	800 W/kg	70% retention after 5000 cycles (device)	<i>J. Alloys Compd.</i> , 2018, 750 , 607–616.
sodium doped Ni ₂ P ₂ O ₇ -Co ₂ P ₂ O ₇	295.2 Cg ⁻¹ at 2 A/g (3 M KOH)	0 – 0.45 V	-	54.1 Wh kg ⁻¹	1700 W kg ⁻¹	95% retention after 2000 cycles (device)	<i>Appl. Surf. Sci.</i> , 2019, 465 , 763–771.
Boron doped carbon/cobalt pyrophosphate hybrid	395.1 F/g at 1.5 A/g (3 M KOH)	-0.2 – 0.55 V	125 F/g at 2 A/g	45 Wh/kg	1735 W/kg	96% retention after 10,000 cycles (device)	This work

3.9 References

- 1 R. M. Dell and D. A. J. Rand, *J. Power Sources*, 2001, **100**, 2–17.
- 2 PATRICE SIMON AND YURY GOGOTSI, *Nat. Mater.*, 2008, **7**, 845–854.
- 3 A. Chu and P. Braatz, *J. Power Sources*, 2002, **112**, 236–246.
- 4 A. Jänes, J. Eskusson, L. Mattisen and E. Lust, *J. Solid State Electrochem.*, 2015, **19**, 769–783.
- 5 R. Bendi, V. Kumar, V. Bhavanasi, K. Parida and P. S. Lee, *Adv. Energy Mater.*, 2016, **6**, 1–6.
- 6 W. Sugimoto, H. Iwata, Y. Yasunaga, Y. Murakami and Y. Takasu, *Angew. Chemie - Int. Ed.*, 2003, **42**, 4092–4096.
- 7 C. Yuan, L. Chen, B. Gao, L. Su and X. Zhang, *J. Mater. Chem.*, 2009, **19**, 246–252.
- 8 C. S. R. R. Samal, M. Kandasamy, B. Chakraborty, *Int. J. Hydrogen Energy*, 2021, **46**, 28028–28042.
- 9 R. Samal, S. Mondal, A. S. Gangan, B. Chakraborty and C. S. Rout, *Phys. Chem. Chem. Phys.*, 2020, **22**, 7903–7911.
- 10 Z. Tang, C. H. Tang and H. Gong, *Adv. Funct. Mater.*, 2012, **22**, 1272–1278.
- 11 L. Cao, F. Xu, Y. Y. Liang and H. L. Li, *Adv. Mater.*, 2004, **16**, 1853–1857.
- 12 J. Xu, Q. Wang, X. Wang, Q. Xiang, B. Liang, D. Chen and G. Shen, *ACS Nano*, 2013, **7**, 5453–5462.
- 13 T. N. Y. Khawula, K. Raju, P. J. Franklyn, I. Sigalas and K. I. Ozoemena, *J. Mater. Chem. A*, 2016, **4**, 6411–6425.
- 14 D. Wang, L. Bin Kong, M. C. Liu, Y. C. Luo and L. Kang, *Chem. - A Eur. J.*, 2015, **21**, 17897–17903.
- 15 R. K. Tripathy, A. K. Samantara and J. N. Behera, *Sustain. Energy Fuels*, 2021, **5**, 1184–1193.
- 16 M. Shao, R. Zhang, Z. Li, M. Wei, D. G. Evans and X. Duan, *Chem. Commun.*, 2015, **51**, 15880–15893.

- 17 X. Wu, L. Jiang, C. Long, T. Wei and Z. Fan, *Adv. Funct. Mater.*, 2015, **25**, 1648–1655.
- 18 H. Pang, Y. Z. Zhang, Z. Run, W. Y. Lai and W. Huang, *Nano Energy*, 2015, **17**, 339–347.
- 19 H. Du, W. Ai, Z. L. Zhao, Y. Chen, X. Xu, C. Zou, L. Wu, L. Su, K. Nan, T. Yu and C. M. Li, *Small*, 2018, **14**, 1801068.
- 20 H. Pang, Z. Yan, Y. Ma, G. Li, J. Chen, J. Zhang, W. Du and S. Li, *J. Solid State Electrochem.*, 2013, **17**, 1383–1391.
- 21 J. Zhang, P. Liu, R. Bu, H. Zhang, Q. Zhang, K. Liu, Y. Liu, Z. Xiao and L. Wang, *New J. Chem.*, 2020, **44**, 12514–12521.
- 22 Z. Khan, B. Senthilkumar, S. Lim, R. Shanker, Y. Kim and H. Ko, *Adv. Mater. Interfaces*, 2017, **4**, 1700059.
- 23 C. Chen, N. Zhang, Y. He, B. Liang, R. Ma and X. Liu, *ACS Appl. Mater. Interfaces*, 2016, **8**, 23114–23121.
- 24 A. K. Thakur, M. Majumder, R. B. Choudhary and S. B. Singh, *J. Power Sources*, 2018, **402**, 163–173.
- 25 C. N. R. Rao, K. Gopalakrishnan and A. Govindaraj, *Nano Today*, 2014, **9**, 324–343.
- 26 L. S. Panchakarla, A. Govindaraj and C. N. R. Rao, *Inorganica Chim. Acta*, 2010, **363**, 4163–4174.
- 27 J. Gao, X. Wang, Y. Zhang, J. Liu, Q. Lu and M. Liu, *Electrochim. Acta*, 2016, **207**, 266–274.
- 28 Q. Jiang, N. Kurra, M. Alhabeb, Y. Gogotsi and H. N. Alshareef, *Adv. Energy Mater.*, 2018, **8**, 1–10.
- 29 L. Zhao, J. Li, P. Chen, G. Li, J. Yu and R. Xu, *Chem. Mater.*, 2008, **20**, 17–19.
- 30 M. Alhabeb, K. Maleski, B. Anasori, P. Lelyukh, L. Clark, S. Sin and Y. Gogotsi, *Chem. Mater.*, 2017, **29**, 7633–7644.
- 31 M. U. Rani, V. Naresh, D. Damodar, S. Muduli, S. K. Martha and A. S. Deshpande, *Electrochim. Acta*, 2021, **365**, 137284.

-
- 32 R. Gond, D. K. Singh, M. Eswaramoorthy and P. Barpanda, *Angew. Chemie - Int. Ed.*, 2019, **58**, 8330–8335.
- 33 F. K. and Q.-H. Y. Ling Ye, Qinghua Liang, Zheng-Hong Huang, Yu Lei, Changzhen Zhan, Yu Bai, Huan Li, *J. Mater. Chem. A*, 2015, **3**, 18860–18866.
- 34 Z. H. Sheng, H. L. Gao, W. J. Bao, F. Bin Wang and X. H. Xia, *J. Mater. Chem.*, 2012, **22**, 390–395.
- 35 D. Y. Shin, K. W. Sung and H. J. Ahn, *Appl. Surf. Sci.*, 2019, **478**, 499–504.
- 36 B. N. Yun, H. L. Du, J. Y. Hwang, H. G. Jung and Y. K. Sun, *J. Mater. Chem. A*, 2017, **5**, 2802–2810.
- 37 M. Liu, J. Li, W. Han and L. Kang, *J. Energy Chem.*, 2016, **25**, 601–608.
- 38 Y. Chang, N. E. Shi, S. Zhao, D. Xu, C. Liu, Y. J. Tang, Z. Dai, Y. Q. Lan, M. Han and J. Bao, *ACS Appl. Mater. Interfaces*, 2016, **8**, 22534–22544.
- 39 M. T. Rinke and H. Eckert, *Phys. Chem. Chem. Phys.*, 2011, **13**, 6552–6565.
- 40 L. Q. Mai, F. Yang, Y. L. Zhao, X. Xu, L. Xu and Y. Z. Luo, *Nat. Commun.*, DOI:10.1038/ncomms1387.
- 41 L. Hou, L. Lian, D. Li, J. Lin, G. Pan, L. Zhang, X. Zhang, Q. Zhang and C. Yuan, *RSC Adv.*, 2013, **3**, 21558–21562.
- 42 Y. Wang, Y. Song and Y. Xia, *Chem. Soc. Rev.*, 2016, **45**, 5925–5950.
- 43 G. A. Muller, J. B. Cook, H. S. Kim, S. H. Tolbert and B. Dunn, *Nano Lett.*, 2015, **15**, 1911–1917.
- 44 H. Li, J. Wang, Q. Chu, Z. Wang, F. Zhang and S. Wang, *J. Power Sources*, 2009, **190**, 578–586.
- 45 X. Zheng, L. Yao, Y. Qiu, S. Wang and K. Zhang, *ACS Appl. Energy Mater.*, 2019, **2**, 4335–4344.
- 46 G. S. Wang, Na, Jinzhang Liu, Yi Zhao, Mingjun Hu, *Nanotechnology*, 2019, **30**, 235403.
- 47 D. W. Wang, F. Li, Z. G. Chen, G. Q. Lu and H. M. Cheng, *Chem. Mater.*, 2008, **20**, 7195–7200.
-

-
- 48 Y. Li, X. Shang, C. Song, J. Chen, Y. Li, M. Huang and F. Meng, *Microporous Mesoporous Mater.*, 2020, **309**, 110535.
- 49 T. Kshetri, D. T. Tran, D. C. Nguyen, N. H. Kim, K. tak Lau and J. H. Lee, *Chem. Eng. J.*, 2020, **380**, 122543.
- 50 N. R. Chodankar, D. P. Dubal, S. H. Ji and D. H. Kim, *Small*, 2019, **15**, 1–11.
- 51 S. Sun, S. Wang, S. Li, Y. Li, Y. Zhang, J. Chen, Z. Zhang, S. Fang and P. Wang, *J. Mater. Chem. A*, 2016, **4**, 18646–18653.
- 52 J. Wang, J. Polleux, J. Lim and B. Dunn, *J. Phys. Chem. C*, 2007, **111**, 14925–14931.
- 53 S. J. Patil, N. R. Chodankar, R. B. Pujari, Y. K. Han and D. W. Lee, *J. Power Sources*, 2020, **466**, 228286.
- 54 D. Kim, J. Kang, B. Yan, K. dong Seong and Y. Piao, *ACS Sustain. Chem. Eng.*, 2020, **8**, 2843–2853.
- 55 X. Sang, Y. Xie, M. W. Lin, M. Alhabeb, K. L. Van Aken, Y. Gogotsi, P. R. C. Kent, K. Xiao and R. R. Unocic, *ACS Nano*, 2016, **10**, 9193–9200.
- 56 Y. Luo, C. Yang, Y. Tian, Y. Tang, X. Yin and W. Que, *J. Power Sources*, 2020, **450**, 227694.
- 57 S. Y. Lin and X. Zhang, *J. Power Sources*, 2015, **294**, 354–359.
- 58 C. Yang, W. Que, X. Yin, Y. Tian, Y. Yang and M. Que, *Electrochim. Acta*, 2017, **225**, 416–424.

CHAPTER-4

4.1 Abstract

4.2 Introduction

4.3 Experimental Section

4.3.1 Materials

4.3.2 Synthesis of Manganese phosphite [Mn₁₁(HPO₃)₈(OH)₆]

4.3.3 Synthesis of graphene oxide (GO)

4.3.4 Synthesis of Manganese phosphite/RGO hybrid

4.3.5 Preparation of Ti₃C₂T_x MXene

4.4 Characterization Techniques

4.5 Electrode Fabrication and Electrochemical Measurements

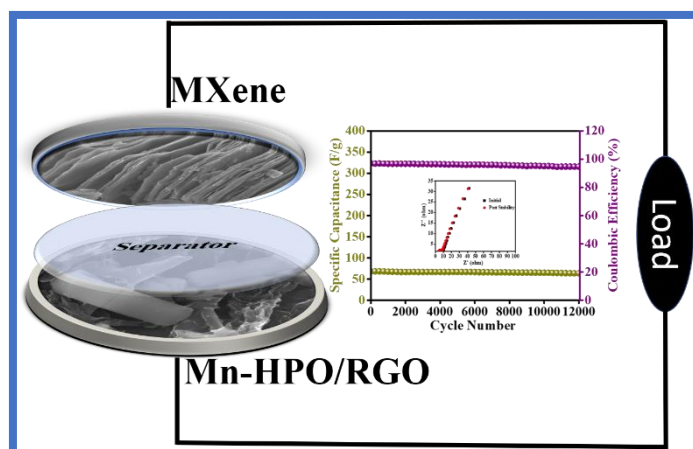
4.6 Fabrication of Asymmetric supercapacitor (ASC)

4.7 Results and Discussions

4.8 Conclusion

4.9 References

4.1 Abstract



Graphical Abstract

Transition metal phosphorous-based materials are considered as ideal candidate for energy storage due to their robustness and durability. In this report, we present manganese phosphite, $\text{Mn}_{11}(\text{HPO}_3)_8(\text{OH})_6$, an interesting inorganic material with spectacular structural features. A single step hydrothermal synthetic route was employed for the fabrication of manganese phosphite/RGO (Mn-HPO/RGO) hybrid. The as synthesized hybrid delivers a specific capacitance of 770 F/g when operated at 1 A/g current density in three electrode set-up with rate capability of 66 %. To broaden the practical applicability of Mn-HPO/RGO hybrid, an asymmetric supercapacitor (ASC) device was fabricated with MXene (Ti_3C_2) as negative electroactive material and Mn-HPO/RGO hybrid as positive active material. The as fabricated device projects a specific capacitance of 108 F/g with an energy density of 34 Wh/kg along with a power density of 508 W/kg. Moreover, the ASC device retains a specific capacitance of 94 % after 12000 constant charge and discharge cycles suggesting the excellent durability of the ASC device. These systematic investigations illustrate that the Mn-HPO/RGO hybrid is a potential choice for high-performance energy storage devices.

4.2 Introduction

The continuous growth of population and pollution around the globe leads to dependency of the non-renewable energy sources such as solar, tidal, wind power etc.¹⁻³ But the inconsistency in the energy generation of these renewable sources provokes the development of various energy storage technologies like fuel cells, supercapacitor and batteries (Li-ion and Na-ion).⁴⁻⁷ In contrast to the current Li-ion and Na-ion batteries, supercapacitors have a high-power density, require less maintenance, are less toxic, and have good cycling stability, making them a reliable energy storage device.⁸ Because of this spectacular behaviour, supercapacitors are currently used in a wide variety of cutting-edge electronic products, from pocket-sized and flexible devices to hybrid electronic vehicles.^{9,10} Henceforth research community all around the world making enormous effort to improve the electrochemical performance of the supercapacitors.

In general, SCs are divided into two categories of capacitors based on the charge storage mechanism: electrochemical double-layer capacitors (EDLC) and pseudocapacitors.¹¹ Pseudocapacitors possess high specific capacitance compared to double layer capacitors.¹² Bio-inspired transition metal chalcogenide such as Ni@NiCo₂S₄/Ni₃S₂ is successfully synthesized by Tong et al. delivers a specific capacitance of 16.9 F cm⁻² at a current density of 10.33 mA cm⁻².¹³ Moreover, Transition metal oxides (RuO₂, MnO₂, NiO and Co₃O₄) are one of the best alternatives as pseudocapacitive material due to presence of variable oxidation state on the metal centre and high specific capacitance.¹⁴ However, the high cost and the toxic nature of ruthenium is the major limitation for its wide applicability. Whereas, the excellent theoretical capacitance of 1370 F/g, low cost and eco-friendly nature of MnO₂ makes it an attractive choice to be used as electroactive material for supercapacitor application.^{15,16} But practical realisation of this theoretical value is hard to achieve because of slow ion transport rate and poor conductivity of MnO₂.¹⁷⁻¹⁹ The issue related to conductivity can be resolved by developing MnO₂/carbon hybrid. But still the low-rate capability and poor cycling stability prevents the manganese oxide-based materials for practical application up to some extent.

On the contrary, transition metal phosphates having good structural stability and versatility in adopting different structures, makes it an appropriate candidate in the field

of catalysis, solar cell, lithium-ion batteries and supercapacitor.^{20–22} In general, Cobalt phosphates serve as a positive active material for rechargeable batteries, heterogenous catalyst, ion exchangers and magnetic materials due to interconnected CoO_x and PO_4 polyhedra forming zeolite type structure.²³ Kim et al. grown cobalt phosphate carbon composite over carbon cloth with the assistance of phytic acid. A layer of nanoparticles along with the phytic acid derived sheet like structure were attached to the surface of the carbon fibre. The supercapacitive performance of the synthesized cobalt phosphate was studied by fabricating a symmetrical supercapacitor device. The device delivers an energy density of 31.1 Wh/kg at a power density of 476 W/kg.²⁴ Marje and co-workers synthesized nickel cobalt phosphate with micro-sheet like architecture. The as synthesized nickel cobalt phosphate was used as cathode and rGO as anode to assemble a solid-state asymmetric device. The assembled solid state device projects a specific capacitance of 102 F/g with an energy density of 36.2 Wh/kg at a power density of 160 W/kg and retains a specific capacitance of 87.3 % after 4000 GCD cycles.²⁵ Furthermore, Werner Massa et al. synthesized manganese orthophosphate in which MnO_5 polyhedra and MnO_6 octahedra shares common edges to form an alternating chain along (110) direction.²⁶ A simple hydrothermal method is employed by Mirghni et al to synthesize pristine $\text{Mn}_3(\text{PO}_4)_2$ and $\text{Mn}_3(\text{PO}_4)_2$ /graphene foam composite with hexagonal microrod and graphene foam deposited hexagonal microrod structure respectively. The $\text{Mn}_3(\text{PO}_4)_2$ and $\text{Mn}_3(\text{PO}_4)_2$ /graphene foam composite provides a specific capacitance value of 41 F/g and 270 F/g respectively at 0.5 A/g current density in 6 M KOH electrolyte.²⁷ The electrochemical performance of the manganese phosphate with ultrathin nano sheet like morphology, was carried out by Ma et al. in both alkaline and neutral electrolyte, delivering a specific capacitance of 194 and 203 F/g in their respective electrolytes.²⁸ Kumar Raju and co-workers studied synthesized ammonium manganese phosphate (AMP) having well-defined 2 D nanosheet architecture with high aspect ratio and surface area. The AMP pseudocapacitive electrode delivered a specific capacitance of 423 F/g at a scan rate of 5 mV/s in 3 M KOH electrolyte.²⁹ Yang and co-workers developed Amorphous manganese phosphate nanoparticles with mesoporous structure by in situ transformation of manganese phosphate 2 D nanoplates. The amorphous manganese phosphate delivers a specific capacitance of 912.4 F/g at 1 A/g current density along with 97 % retention in specific capacitance after 5000 cycles of GCD was observed.³⁰ Although there are some reports

on the synthesis of manganese phosphite ($\text{Mn}_{11}(\text{HPO}_3)_8(\text{OH})_6$) but their energy storage performance is not reported till date. In a certain report, Cheetham group synthesized crystalline manganese phosphite via hydrothermal method. Where the crystal structure is comprised of MO_6 octahedra that shares a common face forming M_2O_9 dimers. These dimeric units share two common edges forming an infinite chain along (001) direction. Each such chains were connected to the four similar types of chains forming an open structure containing two types of channels.³¹ In another report, Jin et. al. synthesized manganese phosphite microrods through solvothermal method with varying water to DMF ratio.³² Therefore, it is essential to explore the supercapacitive performance of this cost-effective manganese-based material.

A single step hydrothermal synthetic route is employed for the synthesis of manganese phosphite/RGO hybrid having microrod architecture. By using SEM and TEM analysis, it has been observed that the microrods of manganese phosphite are unevenly distributed over the RGO layers. However, upon careful analysis it has been found that the microrods are actually composed of small nanoparticles of manganese phosphite. After step-by-step physicochemical characterizations, electrochemical analysis for supercapacitor application was thoroughly studied. Among all the hybrids Mn-HPO/RGO-10 shows best electrochemical performance compared to Mn-HPO/RGO-5 and Mn-HPO/RGO-20. The Mn-HPO/RGO-10 hybrid delivers a specific capacitance of 770 F/g in 1 M H_2SO_4 electrolyte with 70 % retention in specific capacitance after 5000 constant charge-discharge cycles at 5 A/g. The ASC device was fabricated by employing MXene as negative active material and manganese phosphite/RGO hybrid as positive active material that delivers maximum specific capacitance of 108 F/g, maximum energy and power density of 34 Wh/kg and 3105 W/kg respectively. Additionally, the device retains 94 % of its initial capacitance after 12000 cycles of constant charge-discharge at 2 A/g and retention in coulombic efficiency was around 95.3 %.

4.3 Experimental Section

4.3.1 Materials

Manganese acetate tetrahydrate [$\text{Mn}(\text{CH}_3\text{COO})_2 \cdot 4\text{H}_2\text{O}$], Titanium aluminium carbide [Ti_3AlC_2 (MAX phase)], Dimethyl formamide (DMF), N-methylpyrrolidone (NMP)

was procured from Sigma-Aldrich India and Sodium hypophosphite [$\text{NaH}_2\text{PO}_2 \cdot \text{H}_2\text{O}$], Lithium fluoride (LiF) was purchased from HiMedia. Hydrochloric acid (HCl) was procured from Thermo Fisher Scientific. Graphite powder and graphite sheet of thickness 5mm was purchased from Carbon India. Sulfuric acid (H_2SO_4) purchased from Finar chemicals. All the chemicals are used as received without further purification. All the reactions were carried out in deionised water (DIW). Binder-free glass microfiber filter was purchased from Whatman plc.

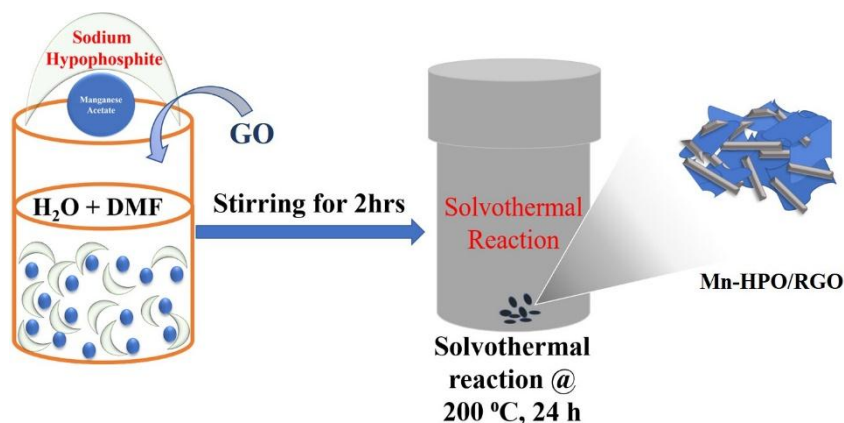
4.3.2 Synthesis of Manganese phosphite [$\text{Mn}_{11}(\text{HPO}_3)_8(\text{OH})_6$]

Manganese phosphite (Mn-HPO) was synthesised as per the report published elsewhere³² with slight variation in the amounts of manganese acetate tetrahydrate and sodium hypophosphite. A single step hydrothermal method was followed for the synthesis of microrod shaped Mn-HPO. In a typical procedure, 980 mg of $\text{Mn}(\text{CH}_3\text{COO})_2 \cdot 4\text{H}_2\text{O}$ and 848 mg of $\text{NaH}_2\text{PO}_2 \cdot \text{H}_2\text{O}$ was added to a mixture DIW/DMF (12 mL/8 mL) solvent. After stirring for 2 hours at room temperature the reaction mixture was transferred into a 50 mL of Teflon lined stainless steel autoclave and the autoclave was kept in an electric oven for 24 hrs at 200°C . The autoclave was cooled down to room temperature naturally and then the white products were collected by centrifugation with DIW. Prior to other physicochemical and electrochemical analysis, the samples were dried at 70°C overnight.

4.3.3 Synthesis of graphene oxide (GO)

Modified Hummer's method was employed to synthesize graphene oxide from graphite powder.^{33,34} Initially, 1 g of graphite powder was added into the 25 ml of concentrated H_2SO_4 in a round bottom flask. The flask is subjected to stirring in an ice bath. Then 3.5 g of KMnO_4 was slowly added to the above mixture with continuous stirring. The solution is further stirred for 2 hrs and the diluted with 50 ml of DIW. After that adequate amount of hydrogen peroxide (H_2O_2) till the gas evolution of gas is ceased. The suspension was then filtered with 0.1 M HCl and deionised water to completely remove the sulphate ions. The washed GO was dried and kept in vacuum desiccator for further use.

4.3.4 Synthesis of Manganese phosphite/RGO hybrid



Scheme 4.1 Schematic representation for the synthesis Mn-HPO/RGO hybrid.

A GO suspension (solution-A) was prepared by dispersing desired amount of synthesized GO in 10 ml of DIW. Afterwards solution-B was prepared by adding required amount of manganese acetate and sodium hypophosphite into a mixed solution of DIW (12 mL) and DMF (8 mL). Solution-A was then mixed with solution-B and the mixture were stirred for 2 hours to obtain a well dispersed uniform solution. The total mixture (solution- A + solution-B) was then transferred to 50 mL of Teflon lined stainless steel autoclave and put into a preheated electric oven at 200 ° C for 24 hours. The obtained samples (manganese phosphite/RGO) were then centrifuged several times with DIW and dried in an oven at 70 ° C overnight for further studies. The as synthesized [Scheme 4.1] hybrid sample is denoted as Mn-HPO/RGO hybrid. The Mn-HPO/RGO hybrid synthesized with the subsequent variation in the amount of GO (from 5 mg to 20) during hydrothermal step to obtain a series of hybrids denoted as Mn-HPO/RGO-5, Mn-HPO/RGO-10 and Mn-HPO/RGO-20 respectively.

4.3.5 Preparation of Ti₃C₂T_x MXene

Here a mild etching process was followed for the synthesis of Ti₃C₂T_x (MXene) by selectively etching the aluminium from the bulk Ti₃AlC₂ (MAX phase) as per the previous report.³⁵ In a typical procedure, 1 g of LiF was dissolved in 20 mL of 9 M HCl by stirring for 30 minutes. 500 mg of Ti₃AlC₂ was then added into this as prepared mild etchant and stirred for 24 hours at room temperature. The obtained suspension was washed repeatedly with DIW by centrifugation till the pH of the supernatant was ≥ 6. The final product was dried in an oven at 70 ° C overnight.

4.4 Characterization Techniques

Powder XRD pattern for the as synthesized sample was examined by using Bruker D8 Advance diffractometer with Cu K α ($\lambda = 1.5418 \text{ \AA}$) radiation of 1600 watt. Horiba scientific Raman analyser equipped with laser wavelength of 532 nm is used to observe the graphitic nature of the synthesized hybrid (Mn-HPO/RGO). X-ray photoelectron spectroscopy (Omicron Nanotechnology Ltd, Germany) with Mg K α radiation of 1253.6 eV as excitation energy is employed to analyse the surface chemical species of the hybrid sample. The surface morphology and energy dispersive X-ray spectra (EDS) of the sample was carried out by FESEM (Merlin Compact with GEMINI-I electron column, Zeiss Pvt. Ltd., Germany). TEM (transmission electron microscopy) and HRTEM (high resolution transmission electron microscopy) images were observed on JEOL JEM 2100F, with an accelerating voltage of 200 kV. A minimum quantity of the sample was well dispersed in DIW and then drop casted over a carbon coated copper grid and dried under Xenon-lamp prior to TEM analysis.

4.5 Electrode Fabrication and Electrochemical Measurements

The electrochemical characterizations were performed by using Biologic SP-200 electrochemical work station. We have selected Ag/AgCl (3 M KCl) as reference electrode and platinum wire as counter electrode. Freshly prepared aqueous 1 M H $_2$ SO $_4$ is used as an electrolyte. The working electrode was prepared by grinding the active material (Mn-HPO and Mn-HPO/RGO), acetylene black, PVDF binder in weight percentage ration of 80:10:10. A minimum quantity of NMP (N-methylpyrrolidone) was added to the above mixture and thoroughly mixed in order to achieve a uniform slurry. The slurry was then drop-casted over a graphite sheet of dimension 1 cm \times 1 cm followed by overnight drying and was used as a working electrode. The mass loading of the active material over the graphite sheet electrode was 1 mg/cm 2 . All the electrochemical measurements such as cyclic voltammetry (CV), galvanostatic charge-discharge (GCD) and cycling stability test were carried out in a potential window of 1 V (0 to 1 V). An AC frequency range of 100 kHz to 10 mHz along with an AC amplitude of 5mV is applied to investigate the electrochemical impedance spectroscopy (EIS). The specific capacitance, energy density and power density of the material is calculated by using following equations.^{36–38}

$$C_{sp} = I_m / (dV/dt) \quad (4.1)$$

$$\text{Energy density (E.D.)} = C_{sp} \times (\Delta V)^2 / (2 \times 3.6) \quad (4.2)$$

$$\text{Power density (P.D.)} = (E.D. \times 3600) / \Delta t \quad (4.3)$$

Where I_m , dV/dt , C_{sp} , ΔV and Δt denotes the mass normalized current density, slope of discharge curve, specific capacitance, potential window, discharge time respectively.

4.6 Fabrication of Asymmetric supercapacitor

An asymmetric supercapacitor (ASC) was assembled by soaking glass microfiber filter membrane in 1 M H_2SO_4 as electrolyte, Mn-HPO/RGO-10 hybrid as positive and MXene as negative electroactive material. The preparation of electrode for ASC follows the same procedure as in three electrode system along with the charge balance for both the electroactive material. Hence the mass loading of both the samples were calculated by the following equation;

$$m_+ / m_- = C_- \times \Delta V_- / C_+ \times \Delta V_+ \quad (4.4)$$

m_+ and m_- is the mass of positive and negative active material, C_+ and C_- is the specific capacitance of both the material at 20 mV/s and ΔV_+ and ΔV_- is operating potential for Mn-HPO/RGO-10 and MXene. The mass ratio was observed to be 0.4. The specific capacitance, energy density and power density were calculated as per equation (4.1), (4.2) and (4.3) respectively.

4.7 Results and Discussions

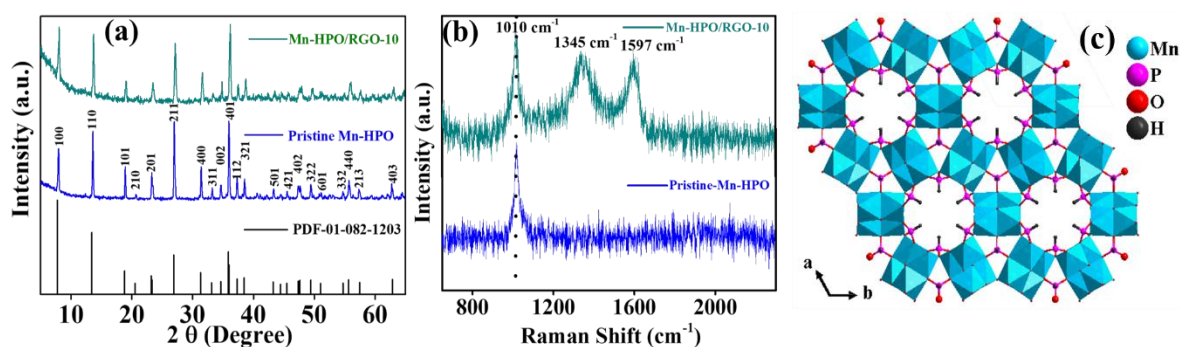


Figure 4.1 (a) Powder XRD pattern (b) Raman spectra of Pristine Mn-HPO and Mn-HPO/RGO-10 hybrid, (c) crystal structure of Mn-HPO based on ICSD-75269.

Phase purity and crystallinity of the pristine (Mn-HPO) and hybrid (Mn-HPO/RGO-10) samples were characterized from the powder XRD measurement as shown in Figure 4.1 (a). The peak positions at 2θ value of 7.8, 13.5, 18.9, 23.1, 27.04, 31.5, 35.8, 37.4 and 38.5 corresponds to the (100), (110), (101), (201), (211), (400), (401), (112) and (321) diffraction planes respectively, implying the hexagonal $\text{Mn}_{11}(\text{HPO}_3)_8(\text{OH})_6$ [PDF 01-082-1203]. The peak positions of Mn-HPO/RGO-10 are well consistent with the parent Mn-HPO. Along with the powder XRD pattern Raman spectrum in Figure 4.1 (b), shows the Raman shift value of 1010 cm^{-1} corresponding to $6(\text{A}_1)$ mode, that is present in both pristine Mn-HPO and Mn-HPO/RGO-10 hybrid sample.³⁹ The bands at 1345 cm^{-1} and 1597 cm^{-1} were assigned to the D and G-bands for Mn-HPO/RGO-10 hybrid is due to the presence of reduced graphene oxide (RGO) in the hybrid. The characteristic D and G band implies the presence of disordered and graphitic nature of the RGO. Again, the ratio of intensities of D and G-band suggest the degree of disorderedness in the graphitic structure. The $I_{\text{D}}/I_{\text{G}}$ ratio in this case was calculated to be 1.08 represents the successful reduction of graphene oxide after hydrothermal treatment. The presence of Raman bands at 1010 cm^{-1} , 1345 cm^{-1} , 1597 cm^{-1} confirm the successful formation of Mn-HPO/RGO-10 hybrid. Moreover, inorganic crystal structure database (ICSD-75269) is further used to represent the schematic crystal structure of Mn- HPO [Figure 4.1 (c)]. The large electron channels present in the material is advantageous for electron transport through the sample.

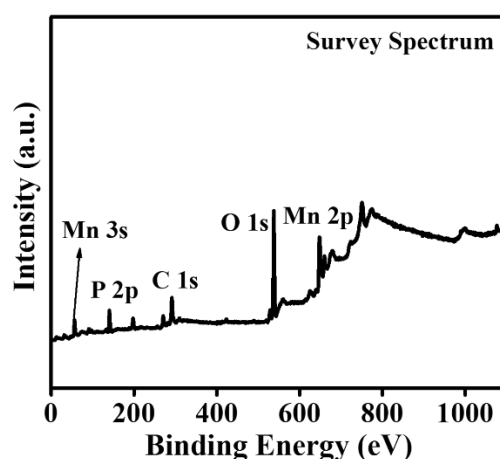


Figure 4.2 XPS survey spectrum of Mn-HPO/RGO hybrid.

Surface chemical species and elemental oxidation state of the as synthesized hybrid was explored with the help of X-ray photoelectron spectroscopy (XPS). The XPS survey spectra in Figure 4.2 confirms the presence of Mn, P, O and C elements in the as synthesized Mn-HPO/RGO-10 hybrid. Furthermore, high resolution XPS spectra of these elements were represented in Figure 4.3 (a-d). In Figure 4.3 (a) two distinct peaks located at 641.5 (Mn 2p_{3/2}) and 653.3 eV (Mn 2p_{1/2}) accompanying two satellite peaks around 645.2 and 656.4 eV respectively, aggregating with the valance state of manganese is +2 in Mn₁₁(HPO₃)₈(OH)₆.^{40–42}

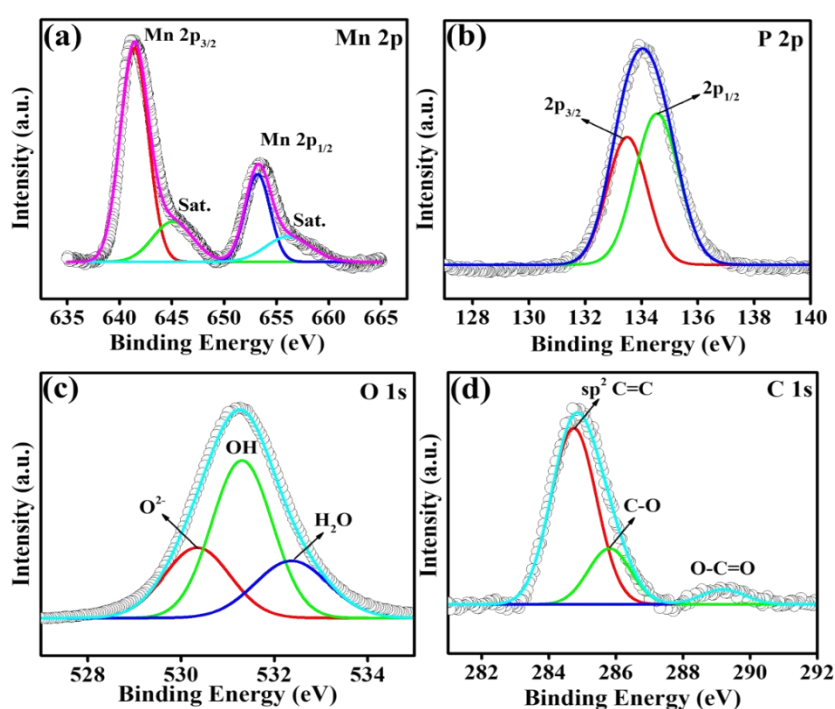


Figure 4.3 core level XPS spectra of (a) Mn 2p, (b) P 2p, (c) O 1s and (d) C 1s.

The peaks positioned at 133.5 and 134.5 eV in the high resolution XPS spectra of phosphorous (Fig. 4.3 (b)) correspond to the characteristic 2p_{3/2} and 2p_{1/2} attributed to the peaks of P (III).⁴³ The deconvoluted XPS spectra of oxygen in Figure 4.3 (c) consists of three peaks. The location of the peaks at a binding energy of 530.4, 531.3 and 532.4 eV are associated with the lattice oxygen (O²⁻), hydroxyl group (OH) and the surface adsorbed water molecules.⁴⁴ The high resolution XPS spectra of carbon in Figure 4.3 (d) consists of a dominant peak at 284.8 eV corresponding to sp² C=C. Again, two smaller components located at 285.9 and 289.3 eV correlated with the existence of C–

O and O–C=O respectively, signifying the presence of reduced graphene oxide in the material.^{45–47}

The FESEM images in Figure 4.4 provides the surface morphology of the pristine Mn-HPO and Mn-HPO/RGO-10 hybrid. The SEM images in Figure 4.4 (a) and (b) shows uniform microrods and the width of the microrod is approximately 600 nm. Similarly, the SEM images in Figure 4.4 (c) and (d) represents the morphology of Mn-HPO/RGO-10 hybrid from lower to higher magnification. The low magnification SEM image shows the non-uniform distribution of the microrods over the graphene sheets. However, the high-resolution SEM image shows the width of the microrods in the Mn-HPO/RGO-10 hybrid is same as that of pristine Mn-HPO. Elemental mapping in Figure 4.4 (e) shows the distribution of Mn, P, O and C throughout the surface of Mn-HPO/RGO hybrid. The EDX (energy dispersive X-ray spectroscopy) analysis (Fig. 4.5) presents the atomic percentage of the elements present in the sample.

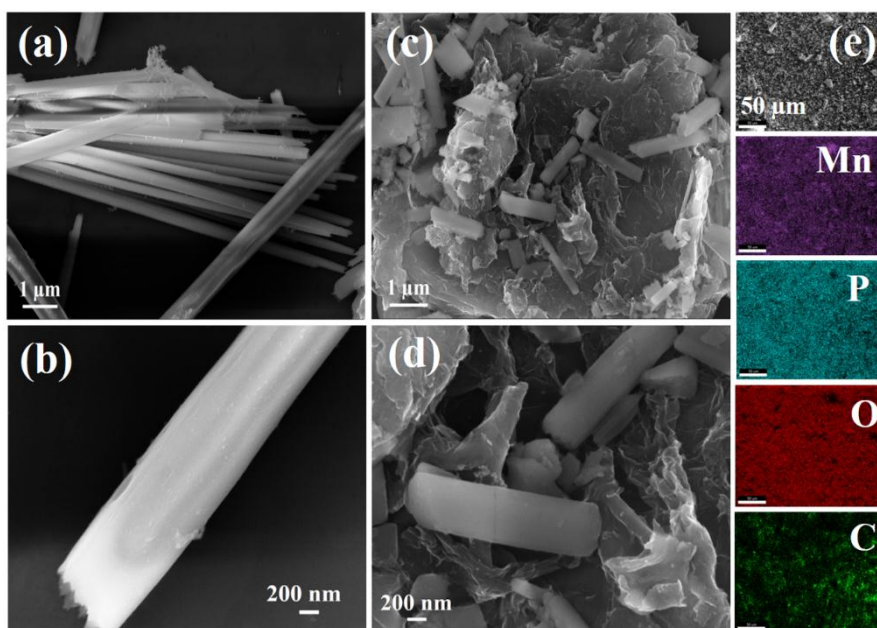


Figure 4.4 (a) & (b) FESEM image of Mn-HPO, (c) & (d) FESEM image of Mn-HPO/RGO-10, (e) EDX-mapped distribution of Mn, P, O, C in Mn-HPO/RGO-10

The morphology of the hybrid was further demonstrated by transmission electron microscopy (TEM) in Figure 4.6. The presence of microrods along with the graphene nanosheets can be clearly observed in low magnification TEM image in Figure 4.6 (a),

that is in accordance with the SEM images of the hybrid. With increasing the magnification of the TEM image to 100 nm, small nanoparticles were spotted (Fig. 4.6 (b)). The high-resolution TEM (HRTEM) image in Figure 4.6 (c) further reveals the presence of a large number of aggregated nanoparticles forming the microrod-shaped Mn-HPO in the hybrid. The fringes of Mn-HPO/RGO-10 hybrid can be distinctly observed in the HRTEM image Figure 4.6 (d). The d-spacing values of 2.70 Å and 2.58 Å were evaluated from Figure 4.6 (d) corresponding to the (311) and (002) crystal planes of Mn-HPO as already mentioned in PXRD pattern.

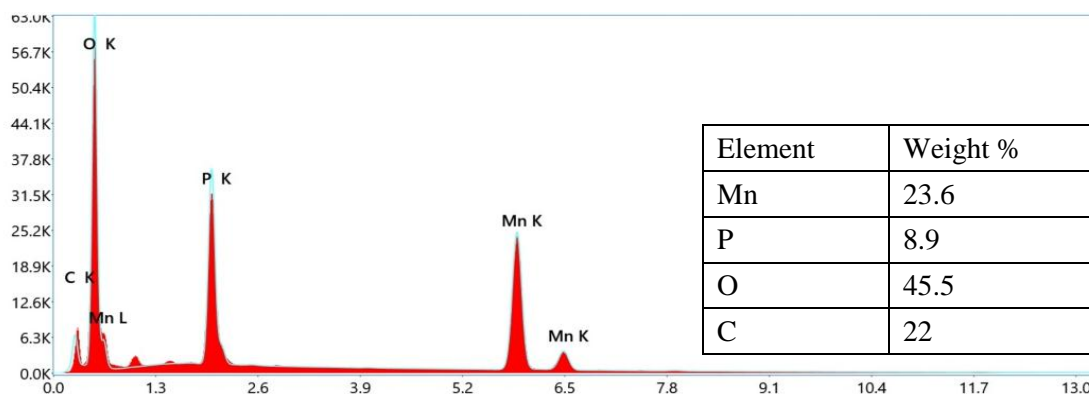


Figure 4.5 EDX spectrum of the Mn-HPO/RGO hybrid with atomic percentage of elements

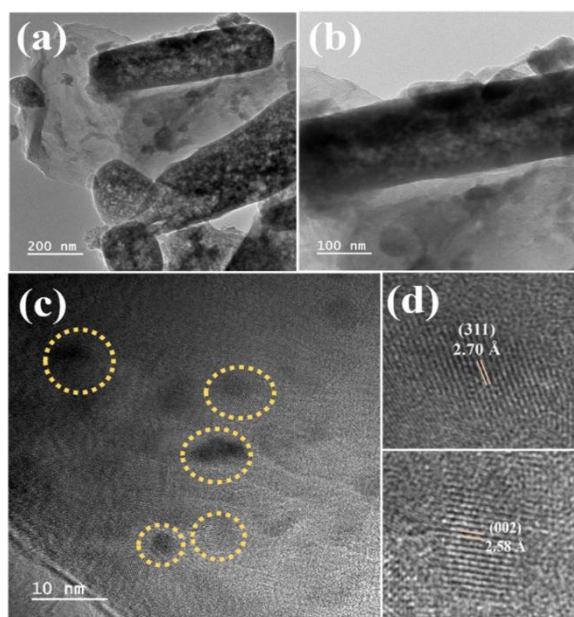


Figure 4.6 (a) and (b) Low-resolution TEM image of Mn-HPO/RGO-10, (c) HRTEM image showing the nanoparticles of Mn-HPO, (d) fringe width of Mn-HPO in Mn-HPO/RGO-10

Initially, the impact of GO concentration of the electrochemical charge storage performance has been accessed by recording the CV and GCDs at sweep rate of 5 mV/s and applied current density of 1 A/g respectively and presented in the following (Fig. 4.7). As seen from the CV curves the current response is increased while moving from Mn-HPO/RGO-5 to Mn-HPO/RGO-10 but again decreases for Mn-HPO/RGO-20. The suppressed electrochemical performance for the Mn-HPO/RGO-20 hybrid may be attributed to the dense distribution of RGO over Mn-HPO. This enables a restricted access of electrolyte to the active redox site of Mn-HPO/RGO-20 hybrid thereby decreasing the performance.

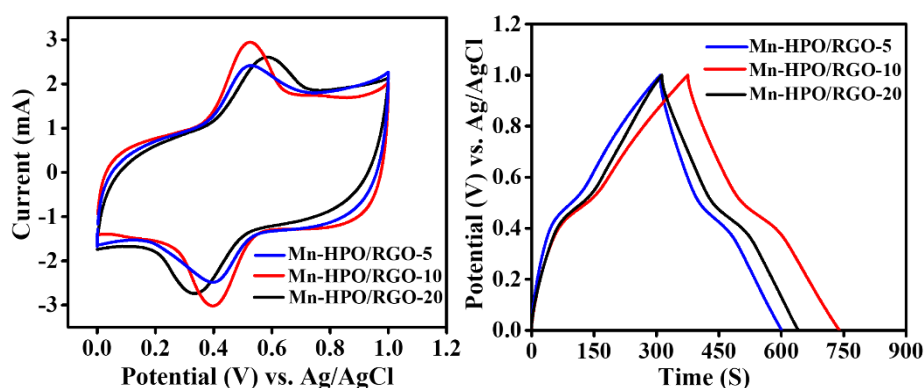


Figure 4.7 CV curves at 5 mV/s and GCD curves at 1 A/g for Mn-HPO/RGO-5, Mn-HPO/RGO-10 and Mn-HPO/RGO-20.

Afterwards, the CV curves for pristine Mn-HPO and Mn-HPO/RGO-10 hybrid were observed at varying scan rate ranging from 5 mV/s to 40 mV/s shown in Figure 4.8 (a) and (b). The quasi-rectangular shaped CV curve along with two redox peaks prevail the co-existence both EDLC and pseudocapacitive behaviour. Although the current response of the CV curve for both pristine Mn-HPO and Mn-HPO/RGO-10 hybrid has been increased with gradual increment in the scan rate (5, 10, 20, 30 and 40 mV/s) the quasi-rectangular shape of the CV curve is still maintained, confirming the material possesses good capacitive behaviour. The area under CV curves for Mn-HPO/RGO-10 hybrid is higher at all scan rate when compared with the pristine Mn-HPO suggesting the higher capacitive behaviour of the hybrid. This enhanced result of Mn-HPO/RGO-10 hybrid can be attributed to the synergistic effect of unique structural feature of Mn-HPO and RGO. The large electron channels of Mn-HPO having 1 D microrod morphology provides fast electron transport. Whereas, the presence of RGO increases

the electrolyte accessibility towards the electrode and shortens the ion diffusion pathway and thus, enhancing the conductivity and electrochemical performance of the overall hybrid.^{43,48}

The charge storage kinetics of pristine Mn-HPO and Mn-HPO/RGO-10 was examined by employing the power law $i = av^b$.⁴⁹ The equation can be re written as $\log(i) = \log(a) + b \log(v)$ where i is the peak current at a particular potential, a & b are variables and v is the scan rate. The slope of the graph between $\log(i)$ vs. $\log(v)$ provides the value of b . The value of $b=1$ suggests the charge storage process is capacitive whereas value of $b = 0.5$ indicates characteristic diffusion-controlled process. The b values obtained for both Mn-HPO and Mn-HPO/RGO-10 were 0.47 and 0.53 respectively, presented in Figure 4.8 (c) suggesting the charge storage process is diffusion-controlled. At a particular potential, the total current ($i(V)$) response is the combination of both surface capacitive current ($i_{capacitive}$) and diffusion controlled current ($i_{diffusion}$). If there is dominance of surface capacitive process, the current response is linearly proportional to v , while in case of diffusion-controlled process the current response is linearly proportional to $v^{1/2}$.⁵⁰ Hence for all possible cases a generalized equation can be written as below,

$$i(V) = i_{capacitive} + i_{diffusion} = k_1v + k_2v^{1/2} \quad (4.5)$$

The above equation can be rearranged as below

$$i(V)/v^{1/2} = k_1v^{1/2} + k_2 \quad (4.6)$$

Figure 4.8 (d) provides the quantitative information on surface capacitive contribution (k_1v) and diffusion-controlled contribution ($k_2v^{1/2}$) for Mn-HPO/RGO-10 hybrid. The surface capacitive contribution increases gradually with increasing the scan rate but the diffusion-controlled process is predominant at lower scan rate. The above results suggest the surface capacitive contribution is around 27 % at 40 mV/s whereas, the surface capacitive contribution is only 11 % at lower scan rate of 5 mV/s for Mn-HPO/RGO-10 hybrid.

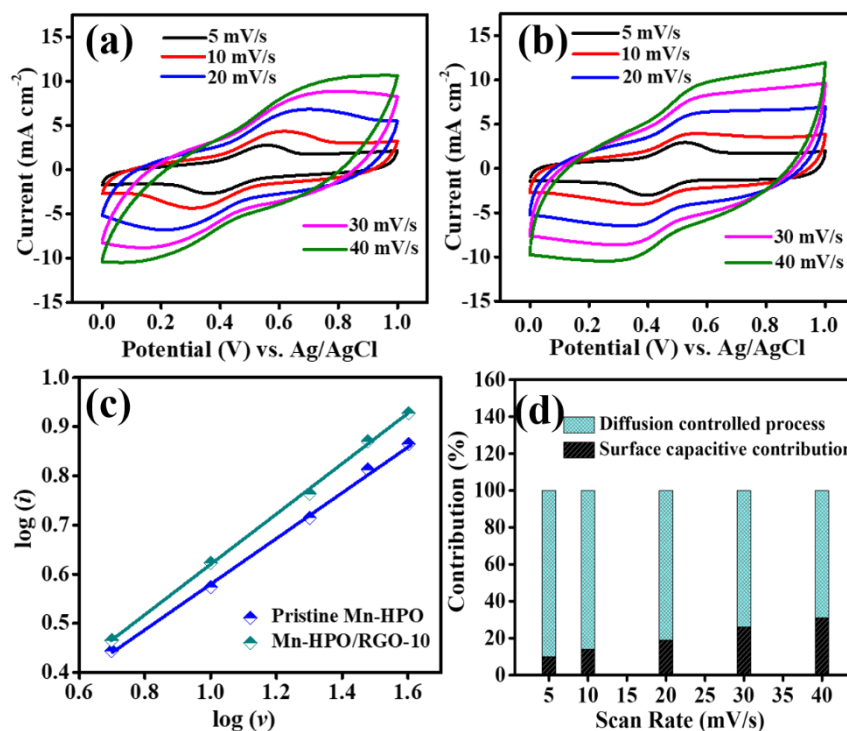


Figure 4.8 (a) CV profiles of Mn-HPO, (b) CV profiles of Mn-HPO/RGO-10 hybrid. (c) $\log(i)$ vs. $\log(v)$. (d) Percentage of the surface and diffusion-controlled process.

The specific capacitances for pristine Mn-HPO and Mn-HPO/RGO-10 were calculated from the galvanostatic charge discharge (GCD) curves. All the GCD measurements were carried out within a current density range of 1 to 5 A/g (1, 2, 3, 4 and 5 A/g) depicted in Figure 4.9 (a) and (b). The specific capacitances for Mn-HPO evaluated using Figure 4.9 (a) are 666, 513, 435, 400 and 358 F/g at a current density ranging from 1 to 5 A/g. Similarly, the specific capacitances are 770, 676, 600, 540, 505 F/g for Mn-HPO/RGO-10 hybrid when the applied current densities are 1, 2, 3, 4 and 5 A/g respectively. The rate capability of pristine Mn-HPO was observed to be 54 % and the same was 66 % for Mn-HPO/RGO-10 hybrid. Specific capacitance vs. current density graph in Figure 4.9 (c) depicts the above-mentioned trend for both Mn-HPO and Mn-HPO/RGO-10 hybrid. The decrease in the value of specific capacitance with increase in current density is associated with the kinetic limitations of the electrolyte ions. At high current density (5 A/g) only surface electrochemical reaction likely to occur as the electrolyte ions will get very short interaction time for electrochemical reaction. However, at lower current density there occurs bulk electrochemical reaction as the electrolyte ions having sufficient interaction time for diffusion towards the inner part

of the active electrode hence providing high specific capacitance at 1 A/g. To examine the durability of the material during charge storage process, GCD operation was carried out at 5 A/g for 5000 cycles and presented in Figure 4.9 (d). The retention of specific capacitance is nearly 70 % after constant GCD operation for 5000 cycles. Similarly, a retention in coulombic efficiency is found out to be 92.4 % suggesting that there occurs no parasitic reaction during this long operation time.

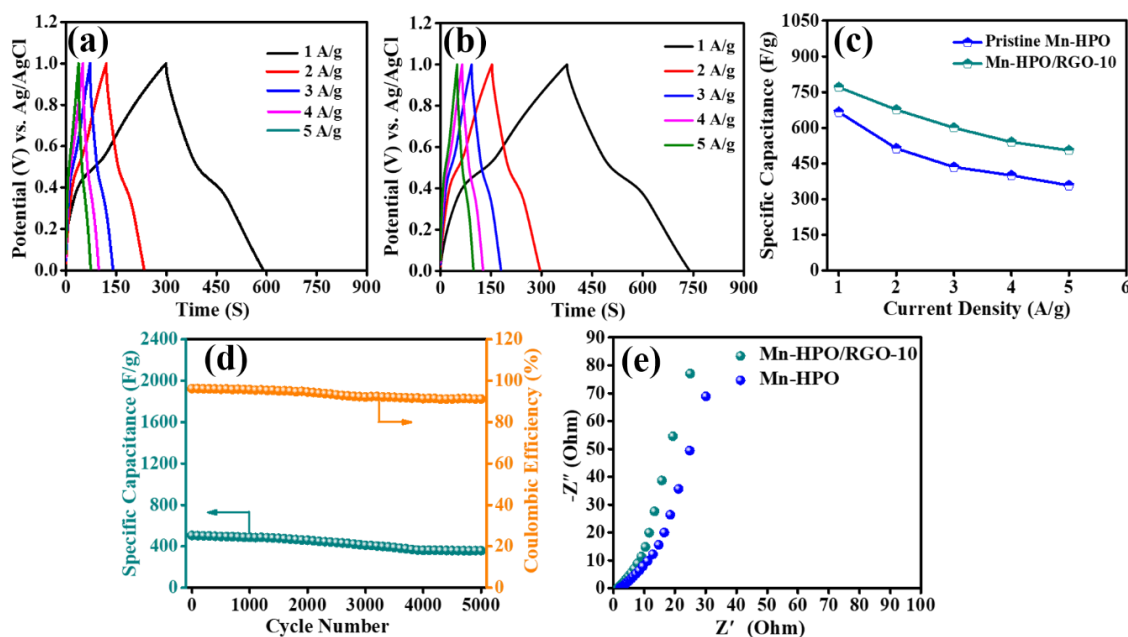


Figure 4.9 (a) GCD profile of Mn-HPO, (b) GCD profile of Mn-HPO/RGO-10, (c) C_{sp} vs. current density (d) coulombic efficiency and cycling stability of the Mn-HPO/RGO-10, (e) EIS of the Mn-HPO and Mn-HPO/RGO-10

Electrochemical impedance analysis is further employed to evaluate the overall electrochemical performance of the pristine and hybrid sample. Figure 4.9 (e) shows the Nyquist plot for both the samples. The interception of Nyquist plot with the real axis (Z') provides the equivalent series resistance, that is the combination of resistance of electrolytic ions, resistance of the electrode and the existing contact resistance between electrode and active material interface. The R_s value obtained for Mn-HPO and Mn-HPO/RGO-10 hybrid is 2.15 and 1.41 Ω respectively. The higher value of R_s for Mn-HPO is mainly due to the additional contact resistance between Mn-HPO and bare graphite sheet. Again, the lower R_s value for Mn-HPO/RGO-10 hybrid illustrates an easy pathway for ion transport and diffusion. The observed Warburg impedance (W) for Mn-HPO and Mn-HPO/RGO-10 hybrid is 9.8 and 5.8 Ω respectively, recommends

the diffusion- controlled behaviour of the material. The above-mentioned values are summarized in a tabular format in Table 4.1.

Table 4.1 Values of various parameters involved in EIS.

Name of the active material	Equivalent Series Resistance (Rs)	Warburg impedance (W)
Mn-HPO	2.15 Ω	9.8 Ω
Mn-HPO/RGO-10 hybrid	1.41 Ω	5.8 Ω

To widen the practical applicability of the as synthesized hybrid, an asymmetric supercapacitor (ASC) device was fabricated by taking Mn-HPO/RGO-10 hybrid as positive active material, MXene (Ti_3C_2) as negative active material and glass microfiber filters soaked in 1 M H_2SO_4 is used to separate the positive and negative electrodes. Good redox chemistry, reversible intercalation of cations, high electrochemical stability of $\text{Ti}_3\text{C}_2\text{T}_x$ MXene makes it an attractive choice for the fabrication of ASC device.^{51,52}

Before assembling electrodes and separator to fabricate the ASC device mass loading of the two active materials are balanced using equation 4.4. The CV experiment was operated at 20 mV/s for both positive and negative active material is presented in Figure 4.10 (a) for the calculation of active mass loading. The mass loading of Mn-HPO/RGO-10 and MXene was evaluated to be 0.4 and 1 mg/cm². The asymmetric device was assembled by enclosing the positive, negative active material and a separator in a coin cell setup (CR2032). The cyclic voltammetry operation (Fig. 4.10 (b)) is carried with a varying scan rate ranging from 5 mV/s to 40 mV/s with in a potential window of 1.6 V. As presented in Figure 4.10 (b) there is no such visible change is observed while increasing the scan rate suggests the outstanding reversibility, appreciable rate capability and good capacitive behaviour of the ASC device. A range of mass normalized current density (0.4 A/g to 2 A/g) is applied to obtain the GCD profiles of Mn-HPO/RGO-10/MXene ASC device, as shown in Figure 4.10 (c). The specific capacitances are calculated at each current density and presented in Figure 4.10 (d). A decrease in the specific capacitance values realised with increasing the current density value. A maximum specific capacitance value of 108 F/g is evaluated at 0.4 A/g whereas retention in specific capacitance is 64 % when the current density is increased 5 times to its initial value.

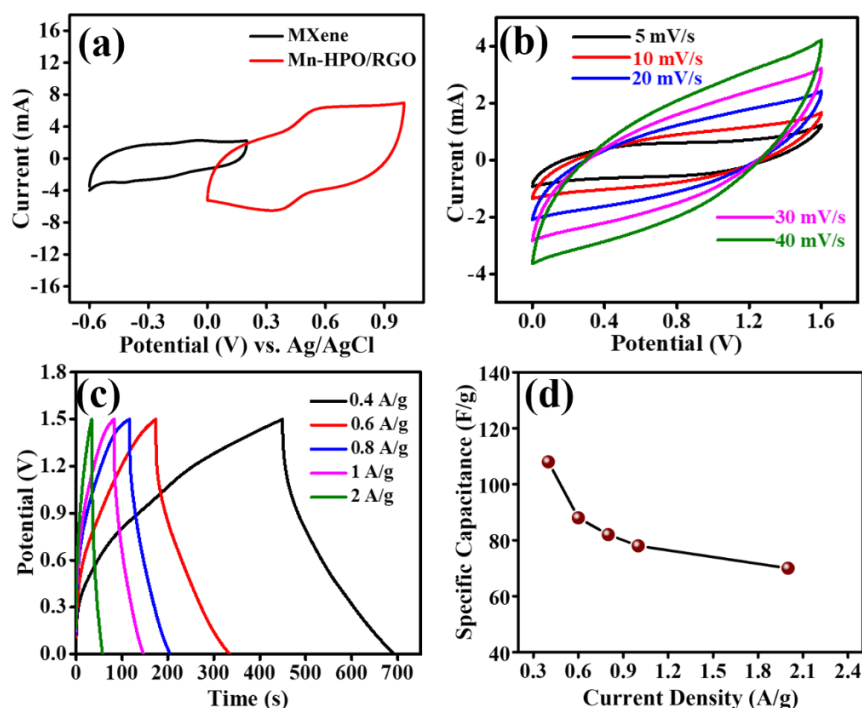


Figure 4.10 (a) CV of Mn-HPO and MXene at 40 mV s^{-1} , (b) CV and (c) GCD curves of the ASC device. (d) C_{sp} of ASC device at various current density

A constant galvanostatic charge-discharge was out at 2 A/g current density for 12000 cycles (Fig. 4.11 (a)) to study the stability of the material during operation. After the cyclic stability test of the ASC device, a capacitance retention of 94 % and the retention in coulombic efficiency is around 96 % suggests the enhanced stability of the material after device fabrication. The inset in Figure 4.11 (a) shows the EIS of the device before and after cyclic stability and it was inferred that the minimal increase in the equivalent series resistance and charge transfer resistance is the reason behind the excellent stability of the device throughout the GCD cycles. The obtained specific capacitance for the device is utilized to determine the energy density and power density of the as fabricated ASC device. The relationship between energy and power density at different current densities is represented by Ragone plot in Figure 4.11 (b). The observed specific energy based on the active mass loading, for the ASC device is 34 Wh/kg at a power density of 508 W/kg at 0.4 A/g and the device still maintains a specific power of 3105 W/kg at 2 A/g current density. It is realised that the electrochemical performance of our synthesized material is higher or close to the other reported manganese-based materials (Table 4.2).

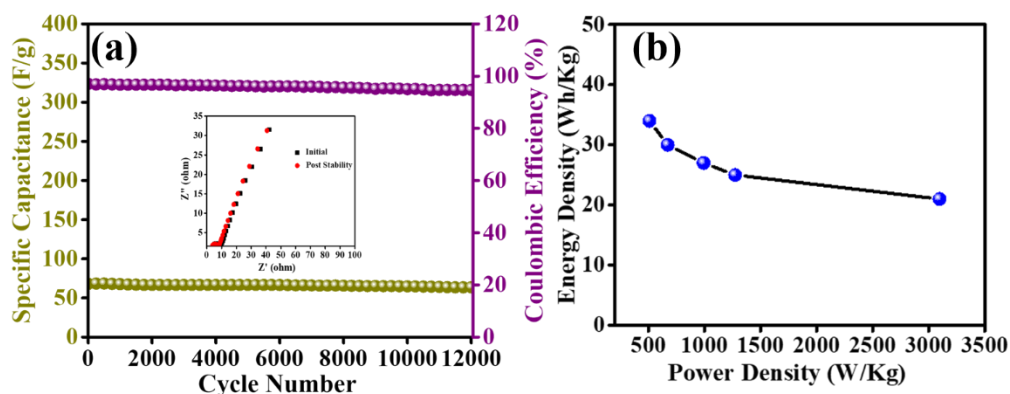


Figure 4.11 (a) Stability and Coulombic efficiency of the ASC device, (b) Ragone plot showing the relation between Power density vs. Energy density

Table 4.2 Comparison of supercapacitor performance of Mn-HPO/RGO with previous reports

Name of the Material	Specific Capacitance (F/g)	Electrolyte	Rate performance (in %)	Specific Capacitance of the device (F/g)	Energy Density of the Device (Wh/kg)	Cyclic Stability	References
MnO _x @C@MnO _x	350	6 M KOH	34.8 %	53.4	23	94 % up to 2000 cycles	<i>Small</i> , 2019, 15 , 1900862
ov-MnO ₂ @MnO ₂	452.4	1 M Na ₂ SO ₄	69.9 %	90.8	40.2	92.2 % up to 10000 cycles	<i>J. Mater. Chem. A</i> , 2018, 6 , 1601–1611
Ti ₃ C ₂ T _x (MXene)-δ-MnO ₂ ASC	-	1 M Na ₂ SO ₄	-	23.3	8.3	-	<i>Energy & Fuels</i> , 2022, 36 , 703–709
Mn ₃ (PO ₄) ₂ /GF	270	6 M KOH	-	28	7.6	96 % up to 10000	<i>J. Colloid Interfac</i>

						cycles	<i>e Sci.</i> , 2017, 494 , 325– 337
Mn ₃ (PO ₄) ₂	203	1 M Na ₂ SO ₄	88 %	46.8	16.64	90 % up to 10000 cycles	<i>RSC Adv.</i> , 2016, 6 , 40077– 40085
Mn ₃ (PO ₄) ₂	194	2 M KOH	85 %	41.9	14.89	90 % up to 10000 cycles	<i>RSC Adv.</i> , 2016, 6 , 40077– 40085
NH ₄ MnPO ₄ · H ₂ O	423	3 M KOH	65 %	65.4	29.4	93 % up to 100k cycles	<i>ACS Energy Lett.</i> , 2020, 5 , 23–30
Amorphous Manganese phosphate	912.4	1 M Na ₂ SO ₄ + PBS	66.6 %	205.59	126	95 % up to 5000 cycles	<i>Adv. Funct. Mater.</i> , 2021, 31 , 210047 7
Mn- HPO/RGO hybrid	770	1 M H₂SO₄	67 %	108	34	94 % up to 12000 cycles	This work

4.8 Conclusion

In summary, the hybrid material (Mn-HPO/RGO-10) was synthesized through a single step hydrothermal approach. The microrod type Mn-HPO is irregularly distributed over RGO sheets as distinguished from the FESEM analysis. Interestingly, the HRTEM study of the hybrid material reveals that the small nanoparticles of Mn-HPO are combined together forming a microrod type architecture. The Mn-HPO/RGO-10 hybrid delivers a specific capacitance of 770 F/g accompanied by a retention in specific capacitance around 70 % after 5000 cycles of GCD operation. Moreover, an ASC device was successfully fabricated by taking MXene as negative active material and Mn-HPO/RGO-10 as positive active material. The ASC device delivers a specific

capacitance of 108 F/g with a maximum energy and power density of 34 Wh/kg and 3105 W/kg respectively. The ASC device projects a capacitance retention of 94 % and retention in coulombic efficiency was 95.3 %, suggesting good durability of the ASC device after a continuous charge discharge operation of 12000 cycles. The aforementioned results provide us an ample of opportunity to further enhance the electrochemical performances of the as synthesized material towards its practical applicability.

4.9 References

- 1 P. G. Bruce, S. A. Freunberger, L. J. Hardwick and J. M. Tarascon, *Nat. Mater.*, 2012, **11**, 19–29.
- 2 R. M. Dell and D. A. J. Rand, *J. Power Sources*, 2001, **100**, 2–17.
- 3 K. Kalyanasundaram and M. Grätzel, *J. Mater. Chem.*, 2012, **22**, 24190.
- 4 Y. Wang, Y. Song and Y. Xia, *Chem. Soc. Rev.*, 2016, **45**, 5925–5950.
- 5 L. Liu, Z. Niu and J. Chen, *Chem. Soc. Rev.*, 2016, **45**, 4340–4363.
- 6 K. Song, J. Liu, H. Dai, Y. Zhao, S. Sun, J. Zhang, C. Qin, P. Yan, F. Guo, C. Wang, Y. Cao, S. Li and W. Chen, *Chem*, 2021, **7**, 2684–2694.
- 7 J. Zhang, Z. Meng, D. Yang, K. Song, L. Mi, Y. Zhai, X. Guan and W. Chen, *J. Energy Chem.*, 2022, **68**, 27–34.
- 8 P. Simon, Y. Gogotsi and B. Dunn, *Science (80-.)*, 2014, **343**, 1210–1211.
- 9 F. Wang, X. Wu, X. Yuan, Z. Liu, Y. Zhang, L. Fu, Y. Zhu, Q. Zhou, Y. Wu and W. Huang, *Chem. Soc. Rev.*, 2017, **46**, 6816–6854.
- 10 R. Bendi, V. Kumar, V. Bhavanasi, K. Parida and P. S. Lee, *Adv. Energy Mater.*, 2016, **6**, 1–6.
- 11 PATRICE SIMON AND YURY GOGOTSI, *Nat. Mater.*, 2008, **7**, 845–854.
- 12 M. Liu, L. Gan, W. Xiong, Z. Xu, D. Zhu and L. Chen, *J. Mater. Chem. A*, 2014, **2**, 2555–2562.
- 13 T. Tang, S. Cui, W. Chen, H. Hou and L. Mi, *Nanoscale*, 2019, **11**, 1728–1736.
- 14 M. Zhi, C. Xiang, J. Li, M. Li and N. Wu, *Nanoscale*, 2013, **5**, 72–88.

-
- 15 M. Toupin, T. Brousse and D. Bélanger, *Chem. Mater.*, 2004, **16**, 3184–3190.
 - 16 X. Su, L. Yu, G. Cheng, H. Zhang, M. Sun and X. Zhang, *Appl. Energy*, 2015, **153**, 94–100.
 - 17 N. Dalili, M. P. Clark, E. Davari and D. G. Ivey, *J. Power Sources*, 2016, **328**, 318–328.
 - 18 S.-B. Yoon and K.-B. Kim, *Electrochim. Acta*, 2013, **106**, 135–142.
 - 19 A. Bahloul, B. Nessark, E. Briot, H. Groult, A. Mauger, K. Zaghbi and C. M. Julien, *J. Power Sources*, 2013, **240**, 267–272.
 - 20 C. Masquelier and L. Croguennec, *Chem. Rev.*, 2013, **113**, 6552–6591.
 - 21 X. L. Hu, S. Piccinin, A. Laio and S. Fabris, *ACS Nano*, 2012, **6**, 10497–10504.
 - 22 Y. Liu, H. Wang, D. Lin, C. Liu, P.-C. Hsu, W. Liu, W. Chen and Y. Cui, *Energy Environ. Sci.*, 2015, **8**, 1719–1724.
 - 23 H. Pang, Y. Liu, J. Li, Y. Ma, G. Li, Y. Ai, J. Chen, J. Zhang and H. Zheng, *Nanoscale*, 2013, **5**, 503–507.
 - 24 T. Kim, A. P. Tiwari, K. Chhetri, G. P. Ojha, H. Kim, S.-H. Chae, B. Dahal, B. M. Lee, T. Mukhiya and H. Y. Kim, *Nanoscale Adv.*, 2020, **2**, 4918–4929.
 - 25 S. J. Marje, V. V. Patil, V. G. Parale, H.-H. Park, P. A. Shinde, J. L. Gunjekar, C. D. Lokhande and U. M. Patil, *Chem. Eng. J.*, 2022, **429**, 132184.
 - 26 W. Massa, O. V. Yakubovich and O. V. Dimitrova, *Solid State Sci.*, 2005, **7**, 950–956.
 - 27 A. A. Mirghni, M. J. Madito, T. M. Masikhwa, K. O. Oyedotun, A. Bello and N. Manyala, *J. Colloid Interface Sci.*, 2017, **494**, 325–337.
 - 28 X.-J. Ma, W.-B. Zhang, L.-B. Kong, Y.-C. Luo and L. Kang, *RSC Adv.*, 2016, **6**, 40077–40085.
 - 29 K. Raju, H. Han, D. B. Velusamy, Q. Jiang, H. Yang, F. P. Nkosi, N. Palaniyandy, K. Makgopa, Z. Bo and K. I. Ozoemena, *ACS Energy Lett.*, 2020, **5**, 23–30.
 - 30 D. Yang, Y. Song, M. Zhang, Z. Qin, R. Dong, C. Li and X. Liu, *Adv. Funct.*

-
- Mater.*, 2021, **31**, 2100477.
- 31 M. P. Attfield, R. E. Morris and A. K. Cheetham, *Acta Crystallogr. Sect. C Cryst. Struct. Commun.*, 1994, **50**, 981–984.
- 32 L. Jin, J. Hong and Y. Ni, *Mater. Chem. Phys.*, 2010, **123**, 337–342.
- 33 and R. E. O. Hummers Jr, William S., *J. Am. Chem. Soc.*, 1958, **80**, 1339–1339.
- 34 G. Goncalves, P. A. A. P. Marques, C. M. Granadeiro, H. I. S. Nogueira, M. K. Singh and J. Grácio, *Chem. Mater.*, 2009, **21**, 4796–4802.
- 35 Q. Jiang, N. Kurra, M. Alhabeab, Y. Gogotsi and H. N. Alshareef, *Adv. Energy Mater.*, 2018, **8**, 1703043.
- 36 X. Zheng, L. Yao, Y. Qiu, S. Wang and K. Zhang, *ACS Appl. Energy Mater.*, 2019, **2**, 4335–4344.
- 37 N. Wang, J. Liu, Y. Zhao, M. Hu and G. Shan, *Nanotechnology*.
- 38 D. Merum, R. R. Nallapureddy, M. R. Pallavolu, T. K. Mandal, R. R. Gutturu, N. Parvin, A. N. Banerjee and S. W. Joo, *ACS Appl. Energy Mater.*, 2022, **5**, 5561–5578.
- 39 A. John, D. Philip, A. K. Idrissi, G. Keresztury and S. Devanarayanan, *J. Raman Spectrosc.*, 2000, **31**, 1067–1071.
- 40 P. K. Katkar, S. J. Marje, S. S. Pujari, S. A. Khalate, P. R. Deshmukh and U. M. Patil, *Synth. Met.*, 2020, **267**, 116446.
- 41 P. K. Katkar, S. J. Marje, V. G. Parale, C. D. Lokhande, J. L. Gunjekar, H.-H. Park and U. M. Patil, *Langmuir*, 2021, **37**, 5260–5274.
- 42 G. Neher and T. T. Salguero, *Cryst. Growth Des.*, 2017, **17**, 4864–4872.
- 43 B. Li, Y. Shi, K. Huang, M. Zhao, J. Qiu, H. Xue and H. Pang, *Small*, 2018, **14**, 1703811.
- 44 H. Dan, K. Tao, Q. Zhou, Y. Gong and J. Lin, *ACS Appl. Mater. Interfaces*, 2018, **10**, 31340–31354.
- 45 A. Padhy, A. K. Samantara and J. N. Behera, *Sustain. Energy Fuels*, 2021, **5**, 3729–3736.
-

-
- 46 W. Ai, Z. Luo, J. Jiang, J. Zhu, Z. Du, Z. Fan, L. Xie, H. Zhang, W. Huang and T. Yu, *Adv. Mater.*, 2014, **26**, 6186–6192.
- 47 S. V. Otari, M. Kumar, M. Z. Anwar, N. D. Thorat, S. K. S. Patel, D. Lee, J. H. Lee, J.-K. Lee, Y. C. Kang and L. Zhang, *Sci. Rep.*, 2017, **7**, 10980.
- 48 A. K. Samantara, J. K. Das, S. Ratha, N. K. Jena, B. Chakraborty and J. N. Behera, *ACS Appl. Mater. Interfaces*, 2021, **13**, 35828–35836.
- 49 R. Ma, X. Zhang, J. Zhuo, L. Cao, Y. Song, Y. Yin, X. Wang, G. Yang and F. Yi, *ACS Nano*, 2022, **16**, 9713–9727.
- 50 T. - C. Liu, W. G. Pell, B. E. Conway and S. L. Roberson, *J. Electrochem. Soc.*, 1998, **145**, 1882–1888.
- 51 X. Sang, Y. Xie, M.-W. Lin, M. Alhabeab, K. L. Van Aken, Y. Gogotsi, P. R. C. Kent, K. Xiao and R. R. Unocic, *ACS Nano*, 2016, **10**, 9193–9200.
- 52 Y. Luo, C. Yang, Y. Tian, Y. Tang, X. Yin and W. Que, *J. Power Sources*, 2020, **450**, 227694.

CHAPTER-5

Electrochemical study of SnO₂/Ti₃C₂T_x hybrid towards supercapacitor application

5.1 Abstract

5.2 Introduction

5.3 Experimental Section

5.3.1 Materials

5.3.2 Synthesis of Tin Oxide (SnO₂)

5.3.3 Synthesis of Ti₃C₂T_x (MXene)

5.3.4 Synthesis of SnO₂/ Ti₃C₂T_x hybrid

5.4 Characterization Techniques

5.5 Electrode Fabrication and Electrochemical Measurements

5.6 Results and Discussions

5.7 Conclusion

5.8 References

5.1 Abstract

In this report we have synthesized SnO₂/Ti₃C₂T_x through a single step hydrothermal route with varying quantities of Ti₃C₂T_x (from 50 mg to 100 mg). The formation of hybrid increases the interlayer spacing of Ti₃C₂T_x that is confirmed from the HRTEM analysis. This increment in the interlayer spacing supports the charge transport towards bulk of the electroactive material. Thus, the resultant hybrid with 80 mg of Ti₃C₂T_x displays a specific capacitance of 620 F/g at 2 A/g current density. In three electrode set-up the electroactive material possesses a capacitance retention of 73 % after 10,000 cycles of continuous charge-discharge. The optimized electrode material shows improved specific capacitance and cyclic stability. The increased interlayer spacing helps in improving the electrolyte accessibility towards the interior of electrode material, enhancing the overall electrochemical performance of the hybrid and thus, the SnO₂/Ti₃C₂T_x.

5.2 Introduction

Considering the global energy crisis and demand, energy harvesters for renewable energy need to work in conjunction with energy storage devices to maintain constant power supply. In this scenario, a long cycle life for the energy storage device is more desirable. Compared to Na-ion batteries and Li-ion batteries, supercapacitors are one of the most crucial energy storage devices in daily life because of their advantages such as long cycle life, high power density, less toxic, needs less maintenance and fast charging and discharging rates¹⁻⁵ Electroactive material is one of the vital components to have enhanced supercapacitor behaviour in terms of achieving high specific capacitance, long cyclic stability.

Despite being a common electrode material for supercapacitors, carbon-based materials' utility is limited in some applications due to their poor specific capacitance and energy density. Combining pseudocapacitive metal oxides, such as RuO₂, MnO₂, NiO, Co₃O₄, Fe₂O₃, and SnO₂, with carbon can increase its specific capacitance.⁶ Among all metal oxides, SnO₂ has drawn increasing interest among the well-known metal oxides, as it is an n-type semiconductor with a large energy gap ($E_g = 3.62$ eV at room temperature), non-toxic nature, high stability and low cost. It can be applied to a variety of electrolytes, including acidic, neutral, and alkaline ones.⁷ The low electrochemical potential of SnO₂ leads to quick redox process and high chemical

stability, makes it an attractive choice for supercapacitor application.⁸ Additionally, by forming SnO₂/carbonaceous material's hybrid leads to increase in the surface kinetics between active sites and electrolyte ions. Thereby, enhancing the electrochemical performances of hybrid materials, that was previously restricted in pristine SnO₂. Several reports are already published on C/SnO₂ composite and/or hybrids, showing excellent electrochemical activity. Li et al. synthesized SnO₂ nanoflowers/graphene nanosheet composite through a facile hydrothermal method without any template. The as synthesized composite delivers a specific capacitance of 126 F/g at 0.2 A/g current density in 1 M H₂SO₄ electrolyte within a potential window of -0.2 to 0.8 V. When charge-discharge cycles were operated over 2000 cycles, 98.2 % retention in specific capacitance was observed.⁹ R. B. Rakhi and co-workers synthesized SnO₂ nanoparticles anchored on graphene nanosheets by chemical reduction method followed by low temp annealing. The designed composite provides a specific capacitance of 205 F/g at a constant current of 10 mA in 0 to 1 V potential range. SnO₂/GNs based symmetric supercapacitor retains 95 % of its initial capacitance even after 1000 cycles of constant operation, indicating the excellent cycle life of the composite material.¹⁰ Another group of researchers designed a novel architecture of uniformly distributed SnO₂ dots on the activated porous carbon nano fibre following a hard template route with a BET surface area of 595.31 m² g⁻¹. This new architecture of SnO₂ shows a specific capacitance 225.4 F/g at 1 A/g current density. To demonstrate the practical applicability a symmetric supercapacitor device is fabricated that delivers a specific capacitance of 43.3 F/g at 1A/g current density. The calculated energy density for the assembled device was found out to be 10.3 Wh/kg at a power density of 325 W/kg. The excellent surface area helps in the diffusion of electrolyte ions towards the inner part of the electrode material, thus improving the electrochemical performance of the composite material.¹¹ Surfactant assisted hydrothermal method was followed by Haldorai et al. to synthesize homogenously distributed flower like SnO₂ nanoparticles over the RGO (reduced graphene oxide) surface. In 1 M H₂SO₄ electrolyte the composite (SnO₂/ RGO) exhibits a specific capacitance of 396 F/g at 4.5 A/g current density and a capacitance retention of 92.6 % even after 10,000 continuous charge-discharge cycles. The excellent stability, good conductivity, high surface area and high specific capacitance resulted from the synergetic interaction between SnO₂ nano flowers and RGO.¹² SnO₂ nanocrystals are homogenously inserted in to the rGO sheets through pulse microwave-assisted

Chapter-5 Electrochemical study of SnO₂/Ti₃C₂T_x hybrid towards Supercapacitor application

deposition method forming SnO₂/rGO composite. In 1 M H₂SO₄ electrolyte the composite achieves a specific capacitance of 348 F/g at 50 mA/g current density. The composite delivers a maximum energy density of 32.2 Wh/kg at a power density of 1000 W/kg. The insertion of SnO₂ nanocrystals in rGO sheets serve as a spacer, that generates more active sites and maximizes the hydrophilic surface, which in turn is the reason behind the enhances specific capacitance of the composite.¹³ SnO₂/SWCNTs core-shell nano architecture was synthesized through electrodeposition strategy. The core-shell composite delivers a specific capacitance of 320 F/g at 6 mV/s in 1 M Na₂SO₄ electrolyte. The low electronic conductivity of the pristine SnO₂ was solved through the SWCNTs shell that provides an electronic conductive channel to enhance the conductivity and keeps the SnO₂ nanoparticles electronic connected thereby increasing the specific capacitance of the core-shell structure.¹⁴ Impregnation method was followed to synthesize SnO₂@C composite and its electrochemical performance was analysed in 1 M KOH electrolyte. A specific capacitance of 432 F/g was achieved at a current density of 1 A/g for SnO₂@C composite electrode. Again, the composite electrode shows an energy density of 29.4 Wh/Kg at a power density of 418 W/kg at 1 A/g current density and the composite retains 95.5 % of specific capacitance for 2000 cycles. The presence of both micropores and mesopores in carbon matrix makes an easy access of the electrolyte to SnO₂, thus improving overall electrochemical performance SnO₂@C composite.¹⁵ Lately, 2D transition metal carbides, carbonitrides and nitrides (MXenes) with general formula M_{n+1}AX_n (n = 1,2 or 3) are synthesized by selective etching of A groups from MAX phase. Here, M is an early transition metal (such as Ti, V, Nb, Mo, Cr and Ta), A is a group 13 or 14 element (e.g., Al, Si, Ga and In) and X is carbon or nitrogen (C or N).¹⁶ Among all the MXenes discovered titanium carbide (Ti₃C₂T_x) is the mostly studied and first reported one. Ti₃C₂T_x is synthesized by selectively removing Al group from Ti₃AlC₂ using hydrofluoric acid where, T_x is the surface functional groups like -F, -OH and =O.¹⁷ High electronic conductivity (upto 15,000 S cm⁻¹), packing density (4 g cm⁻³), increased hydrophilicity, the redox chemistry at metal oxide/hydroxide surface makes Ti₃C₂T_x MXene a suitable candidate for supercapacitor application.

The aforementioned behaviour of Ti₃C₂T_x and SnO₂ proves us to synthesize SnO₂/Ti₃C₂T_x hybrids. Thus, herein we report a single step hydrothermal route to synthesize SnO₂/Ti₃C₂T_x composites with varying the amount of Ti₃C₂T_x from 50 to

100 mg. After successful synthesis of the pristine SnO₂, Ti₃C₂T_x and SnO₂/Ti₃C₂T_x-80 hybrid, their morphology was analysed through FESEM, TEM and HRTEM. FESEM images of SnO₂ reveals the agglomerated morphology, that is further intercalated in between the Ti₃C₂T_x layers. TEM image of SnO₂ disclose that the agglomerated architecture is actually the composed of small rice grain type nanoparticles. Furthermore, increase in interlayer spacing of Ti₃C₂T_x layers in SnO₂/Ti₃C₂T_x-80 was observed from HRTEM analysis that supports the charge transport in this hybrid.¹⁸

Afterwards the electrochemical study of SnO₂/Ti₃C₂T_x-80 shows better supercapacitor performance compared to pristine SnO₂, and other synthesized hybrids. In three electrode set-up SnO₂/Ti₃C₂T_x-80 delivers a specific capacitance of 620 F/g with a rate capability of 45 %. After 10,000 cycles of constant charge and discharge at 10 A/g, it was found that the electrode retains 73 % of its initial capacitance.

5.3 Experimental Section

5.3.1 Materials

Tin chloride pentahydrate (SnCl₄.5H₂O), Ti₃AlC₂ (MAX) were procured from sigma Aldrich. Fuming hydrochloric acid (HCl), Urea (NH₂CONH₂) and potassium hydroxide (KOH) were purchased from Hi-Media chemicals. Deionised water (DIW) was used for all the chemical synthesis and electrochemical measurements.

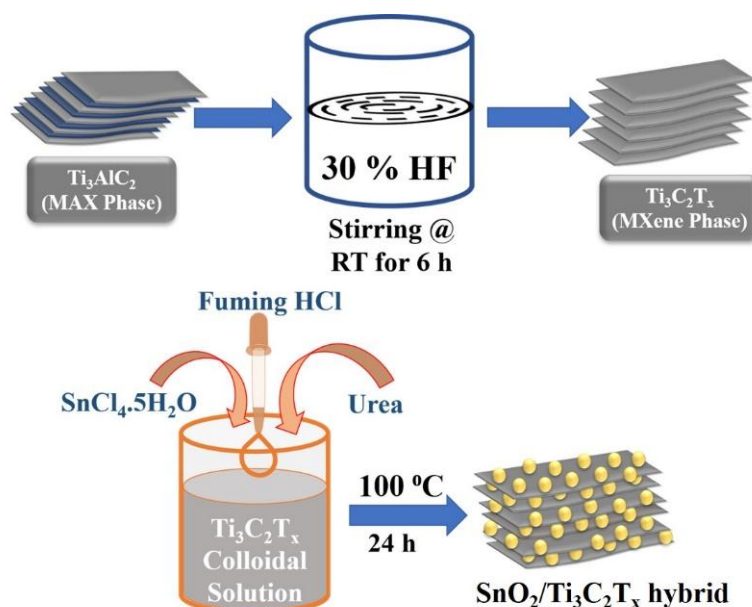
5.3.2 Synthesis of Tin Oxide (SnO₂)

SnO₂ was successfully synthesized through a simple hydrothermal method reported elsewhere²⁰ with slight modification in the temperature as depicted in scheme 5.1. Initially, 0.1 g of SnCl₄.5H₂O is dissolved in 40 ml of deionised water and then 1 g of urea is added to the SnCl₄.5H₂O solution. The mixed solution was stirred well to get a transparent solution. Afterwards, 2 ml of fuming HCl was added to it. The transparent solution was then transferred to a Teflon lined stainless steel autoclave having 50 ml capacity and kept in an electric oven. The oven was maintained at a constant temperature of 100 ° C for 24h. Then the autoclave was removed from the electric oven and allowed to cool down to room temperature. The white coloured SnO₂ powder from the autoclave was recovered by centrifugation followed by washing in DIW and ethanol several times and drying at 70 ° C.

5.3.3 Synthesis of Ti₃C₂T_x (MXene)

Selectively, aluminium etching strategy in Ti₃AlC₂ was followed to synthesize 2D layered Ti₃C₂T_x. Herein, we have used HF as an aluminium etchant for the synthesis of Ti₃C₂T_x as reported previously.²¹ 0.25 g of Ti₃AlC₂ powder was added to 5 ml of 30 % HF and stirred at room temperature for 6 h. After 6 h of constant etching the resultant product was separated by continuous centrifugation in DIW till the pH of the supernatant becomes ≥ 6 . The obtained product was then dried overnight in an electric oven maintained at 70 ° C.

5.3.4 Synthesis of SnO₂/Ti₃C₂T_x hybrid



Scheme 5.1 Schematic representation for the synthesis of SnO₂/Ti₃C₂T_x hybrid

The precursors for the synthesis of SnO₂ were added to the Ti₃C₂T_x colloidal solution with varying amount of Ti₃C₂T_x (50, 80 and 100 mg). Then the resultant mixture was stirred vigorously to get the uniform dispersion of Ti₃C₂T_x in the solution. The solution was then poured in a 50 ml autoclave and kept in an electric oven at 100 ° C for 24 h. Afterwards the autoclave was left to cool down to room temperature. Then the resultant hybrids were washed with DIW and ethanol alternatively for three times and dried in a vacuum oven for overnight. The dried powders were kept in a vacuum desiccator for further physicochemical and electrochemical characterizations. The obtained product was abbreviated as SnO₂/Ti₃C₂T_x-50, SnO₂/Ti₃C₂T_x-80, SnO₂/Ti₃C₂T_x-100.

5.4 Characterization Techniques

For powder XRD analysis of the as synthesized samples, Bruker D8 Advance diffractometer equipped with Cu K α radiation with wavelength (λ) 1.5418 Å and a diffractometer monochromator operated at a power of 1600 watt is used. For elemental composition and surface analysis PHI Versa Probe II X-ray photoelectron spectroscopy was used. The surface morphology of the sample was examined by FESEM (Merlin Compact with GEMINI-I electron column, Zeiss Pvt. Ltd, Germany). For HRTEM and TEM (HRTEM, JEOL JEM 2100F, with an accelerating voltage of 200 kV) analysis, a carbon-coated copper grid was drop casted with the evenly dispersed sample in deionized water. The grid was then completely dried under a xenon lamp before the microscopic study. The electrochemical characterizations were carried out in a Biologic SP-200 electrochemical workstation.

5.5 Electrode Fabrication and Electrochemical Measurements

The slurry of the electroactive material was prepared by thoroughly grinding acetylene black (conductive additive), PVDF (binder) and as synthesized material in weight percentage ratio of 10:10:80 respectively. A minimum quantity of DMF was added to the thoroughly ground mixture to have a thick slurry. The slurry was then coated over a graphite sheet having dimension 1 cm \times 1 cm using a doctor blade. The weight of the active material over the graphite sheet was calculated to be 1 mg/cm². Now, the electroactive coated graphite sheet was used as a working electrode and all the electrochemical measurements like cyclic voltammograms, galvanostatic charge-discharge, electrochemical impedance spectroscopy, cyclic stability was performed Biologic SP-200 electrochemical workstation. For all the three electrode measurements Hg/HgO and Pt wire was used as reference and counter electrode respectively. All the electrochemical measurements were carried out in freshly prepared 3 M KOH electrolyte due to the reason that in aqueous medium K⁺ ion having highest ionic conductivity among all cations after H₃O⁺ and OH⁻ having the highest ionic conductivity among all the anions.²² The following equations are involved to calculate the resultant specific capacitance, energy density and power density.²³

$$C_{sp} = I_m / (dV/dt) \quad (5.1)$$

$$\text{Energy density (E.D)} = C_{sp} \times (\Delta V)^2 / 7.2 \quad (5.2)$$

$$\text{Power density (P.D)} = (E.D \times 3600)/\Delta t \quad (5.3)$$

Where I_m , (dV/dt) , ΔV and Δt is the mass normalized current density, slope of the discharge curve, operating potential window and discharge time respectively.

5.6 Results and Discussions

Powder XRD patterns in Figure 5.1 (a) shows the phase purity of the as synthesized composites. The diffraction planes at (110), (101), (200), (211), (002), (301) correspond to the 2θ values of 26.57, 33.87, 37.95, 57.73, 57.83, 65.96 suggesting the tetragonal phase of SnO₂ having PDF 00-021-1250. The matching pattern of SnO₂ along simulated pattern is presented in Figure 5.2 (a). Successful synthesis of Ti₃C₂T_x from Ti₃AlC₂ is confirmed from the XRD pattern of both in Figure 5.2 (b).

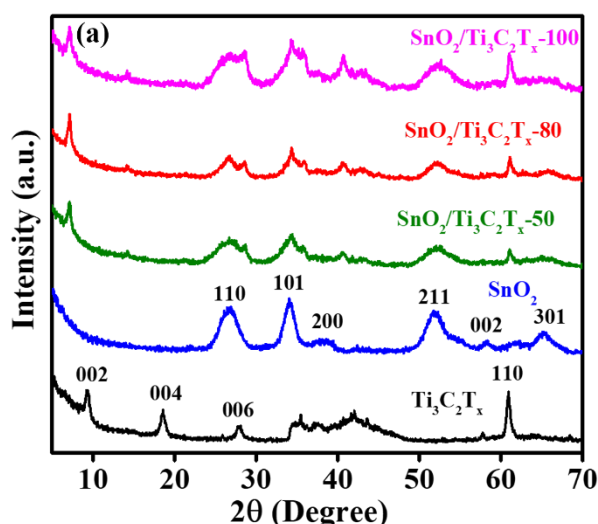


Figure 5.1 (a) PXRD pattern Pure Ti₃C₂T_x, SnO₂ and all the SnO₂/Ti₃C₂T_x hybrids

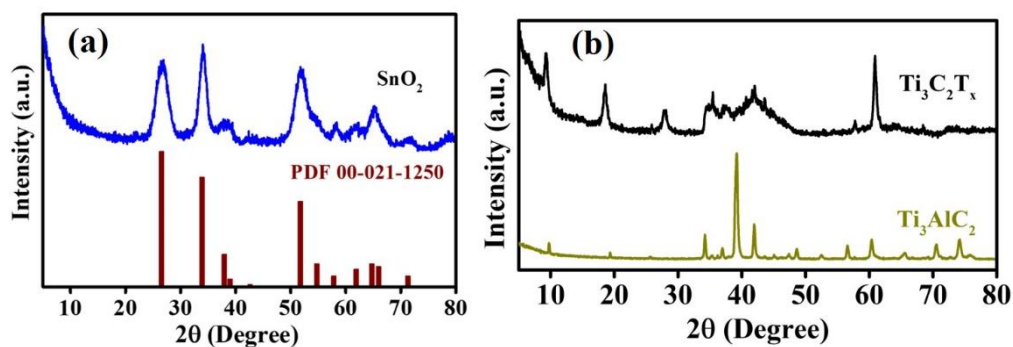


Figure 5.2 (a) PXRD pattern of SnO₂ matching with PDF 00-021-1250, (b) PXRD pattern of MAX & MXene phase

Additionally, the XRD the hybrids of SnO₂/Ti₃C₂T_x (SnO₂/Ti₃C₂T_x-50, SnO₂/Ti₃C₂T_x-80, SnO₂/Ti₃C₂T_x-100) were presented in the Figure 5.1 (a) reveals the consistency of the characteristic peaks of pristine SnO₂. Although there is no peak shift in the (110), (101) planes of SnO₂ in SnO₂/Ti₃C₂T_x but with increasing Ti₃C₂T_x quantity from 50 to 100 reflects the peaks of Ti₃C₂T_x in the hybrid suggesting the successful formation of the hybrids. Again, in all the three composites there exists distinctive peak of Ti₃C₂T_x at (002) plane but there is prominent shift in the peak position is observed. The shift of peaks position of (002) plane of Ti₃C₂T_x from 2θ value of 9.3 to 8.2 indicates there is increase in interlayer distance in the hybrids. The increase in interlayer distance may be attributed to the positioning of SnO₂ nanoparticles between/on the surface of 2D Ti₃C₂T_x layers, that is further confirmed from HRTEM analysis.

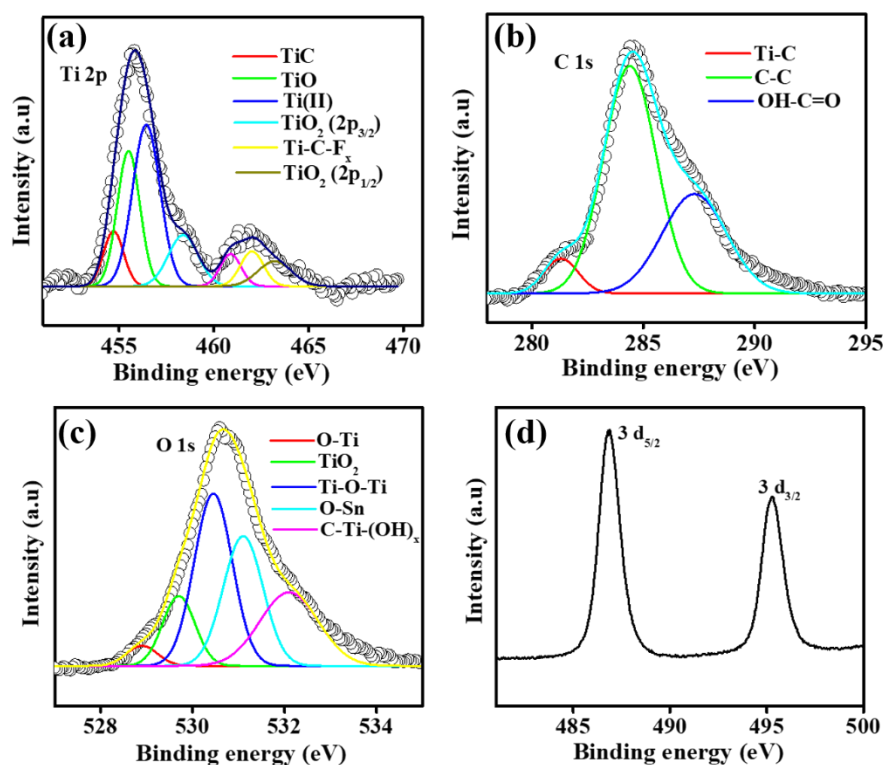


Figure 5.3 Core level XPS spectra of (a) Ti 2p, (b) C 1s, (c) O 1s, (d) Sn 3d

X-ray photoelectron spectroscopy is further employed to find out the bonding and oxidation state of SnO₂/Ti₃C₂T_x-80 is shown in Figure 5.3. Figure 5.3 (a) presents the high resolution XPS of Ti 2p, where six peaks for Ti–C, Ti–O, Ti (II), TiO₂ 2p_{3/2}, Ti–C–F_x, and TiO₂ 2p_{1/2} were observed at 454.7 (460.9), 455.2, 456.1, 458.7, 462.0, 464.2 eV binding energies respectively.^{24–28} The XPS of C 1s (Fig. 5.3 (b)) is deconvoluted

into three peaks at binding energies 281.2, 284.8 and 288.2 eV correspond to Ti-C, C-C and HO-C=O bond respectively.^{24,29} Similarly, the high resolution XPS of O 1s was depicted in Figure 5.3 (c). Five deconvoluted peaks are observed at binding energies 528.9, 529.9, 530.3, 531.5 and 532.4 eV correspond to O-Ti, TiO₂, Ti-O-Ti, O-Sn, C-Ti-(OH)_x bonds respectively.^{11,29-32} The XPS of Sn 3d presented in Figure 5.3 (d) shows two peaks at 487.59 eV for 3 d_{5/2} and a satellite peak at 496.09 for 3 d_{3/2} represents the +4 oxidation state of Sn. There are no other peaks corresponding to other chemical oxidation state of Sn suggesting the presence of only Sn⁴⁺ in the hybrid. The difference in the binding energies for Sn 3d_{5/2} and Sn 3d_{3/2} is 8.5 eV. The peak position and peak distance are identical to the binding energies reported for SnO₂.³³

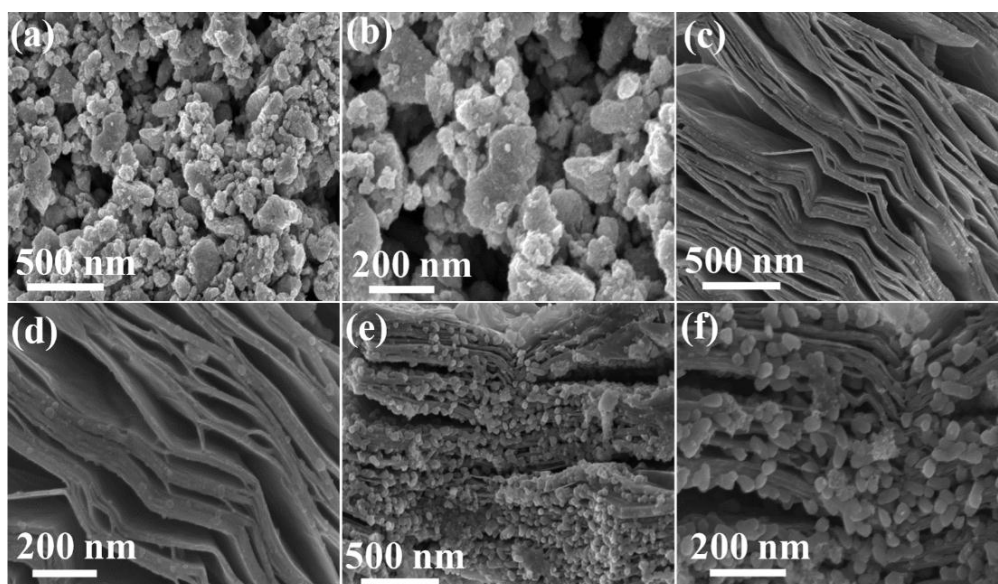


Figure 5.4 Low and High Magnification FESEM Image of (a) and (b) SnO₂, (c) and (d) Ti₃C₂T_x 2D layers, (e) and (f) SnO₂/Ti₃C₂T_x-80

Figure 5.4 displays the morphological analysis of the pristine SnO₂, pristine Ti₃C₂T_x and SnO₂/Ti₃C₂T_x-80 hybrid. The agglomerated morphologies of pristine SnO₂ were displayed in low magnification FESEM image of Figure 5.4 (a), that completely agrees with high magnification FESEM image of SnO₂ in Figure 5.4 (b). The surface morphology of Ti₃C₂T_x in Figure 5.4 (c) presents the accordion like architecture, that provides large active sites for holding the electrolyte ions. The high resolution FESEM image in Figure 5.4 (d) shows the successfully etching of Ti₃AlC₂ layers forming Ti₃C₂T_x. Compared to pristine SnO₂, reduced agglomeration of SnO₂ in the SnO₂/Ti₃C₂T_x-80 hybrid is observed and those SnO₂ particles are anchored over the

Ti₃C₂T_x layers as presented in Figure 5.4 (e). Whereas, upon close analysis of the SnO₂/Ti₃C₂T_x-80 hybrid it was clearly observed that in Figure 5.4 (f) the SnO₂ nanoparticles inserted in between the Ti₃C₂T_x layers preventing the restacking of the layers.

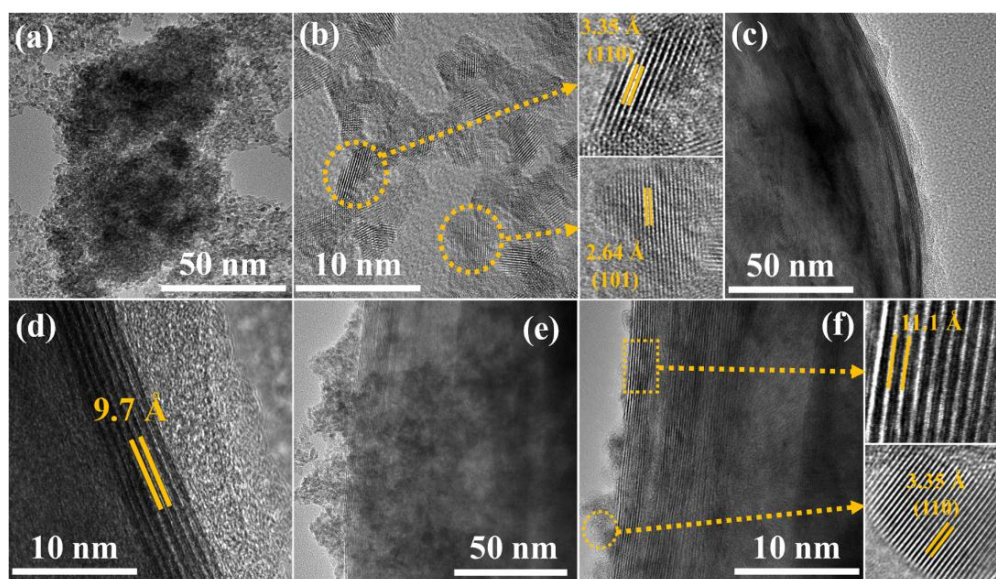


Figure 5.5 TEM and HRTEM image of (a) & (b) SnO₂, (c) & (d) Pristine Ti₃C₂T_x, (e) & (f) SnO₂/Ti₃C₂T_x-80 respectively.

Again, the morphology of agglomerated SnO₂ can be further verified from the TEM and HRTEM analysis in Figure 5.5 (a) and (b). In Figure 5.5 (a) it is clearly visible that the agglomerated morphology is mainly due to the aggregation of the rice grain type nano particles. The high-resolution TEM image in Figure 5.5 (b) provides us the information regarding the d-spacing values of the SnO₂ nanoparticles. It was evaluated that the d-spacing values are 3.35 Å, 2.64 Å suggesting the (110) and (101) plane of SnO₂. Furthermore, the TEM image of pure Ti₃C₂T_x in Figure 5.5 (c) shows the layered morphology whereas Figure 5.5 (e) reveals the successful intercalation of rice grain type SnO₂ nanoparticles in between the Ti₃C₂T_x layers in SnO₂/Ti₃C₂T_x-80 hybrid. However, the increase in interlayer distance of Ti₃C₂T_x in SnO₂/Ti₃C₂T_x-80 is confirmed from the d-spacing calculation of both the pure Ti₃C₂T_x and SnO₂/Ti₃C₂T_x-80 as presented in Figure 5.5 (d) and (f). The d-spacing value of (002) is 9.7 Å whereas in case of SnO₂/Ti₃C₂T_x-80 hybrid the d-spacing value is around 11.1 Å. The increase in d-spacing justifies the peak shift of (002) plane towards lower angle in powder XRD pattern after the formation of hybrid. The increase in d-spacing in Ti₃C₂T_x layers and

reduction in agglomeration of SnO₂ nanoparticles in SnO₂/Ti₃C₂T_x-80 may cause the easy charge transportation in the electroactive material and provides a facile pathway for electrolyte to access SnO₂ thereby enhancing the electrochemical performance of the hybrid.

The electrochemical performance of the pristine SnO₂, Ti₃C₂T_x, SnO₂/Ti₃C₂T_x hybrids were investigated by using three electrode configuration. In the three-electrode system, Pt wire was used as a counter electrode, Hg/HgO electrode as a reference electrode and electroactive material coated graphite sheet as working electrode. The electrochemical performance of the active material was studied by cyclic voltammetry (CV), galvanostatic charge-discharge (GCD) and electrochemical impedance spectroscopy (EIS) in 3 M KOH electrolyte within a potential window of 0.8 V (-1.0 V to -0.2 V).

The CV curves in Figure 5.6 (a) is for pure SnO₂ at scan rate ranging from 5 to 100 mV/s. The CV curves are of quasi-rectangular in nature and deviate while moving from low to high scan rate. Kinetic limitation, that restricts movement of electrolyte ions to the interior of the electroactive material at higher scan rate, thus deviating the shape of the CV curves. Moreover, no distinct redox peaks are observed during all the scan rates suggesting the capacitive behaviour of the material in a negative potential region. In order to verify the charge storage mechanism of pristine SnO₂ a graphical representation in Figure 5.6 (b) illustrates the relationship between current and scan rate at a particular potential. The current and scan rates were related to each other by the power law mentioned below;³⁴

$$i = av^b \quad (5.5)$$

Where a and b are the adjustable parameter.

Equation (5) can be rewritten in logarithmic form as below

$$\log(i) = \log(a) + b\log(v) \quad (5.6)$$

Linear plot between $\log(i)$ vs. $\log(v)$ provides us a value of b from the slope of the graph. Depending upon the value of b the charge storage mechanism is classified into two categories; (i) $b = 0.5$ means current is proportional to the square root of the scan rate and the charge storage mechanism is of diffusion-controlled battery type nature, (ii) $b = 1$ means current is linearly dependant on the scan rate and the charge storage mechanism is of capacitive in nature.³⁵ Here the value of b is found out to be 0.96

(Figure 5.6 (b)) reveals that the charge storage behaviour is mainly capacitive dominant. The capacitive nature comes from the adsorption and desorption of K⁺ ions from the electrolytic solution on to the SnO₂ surface as presented in the equation below,³⁶

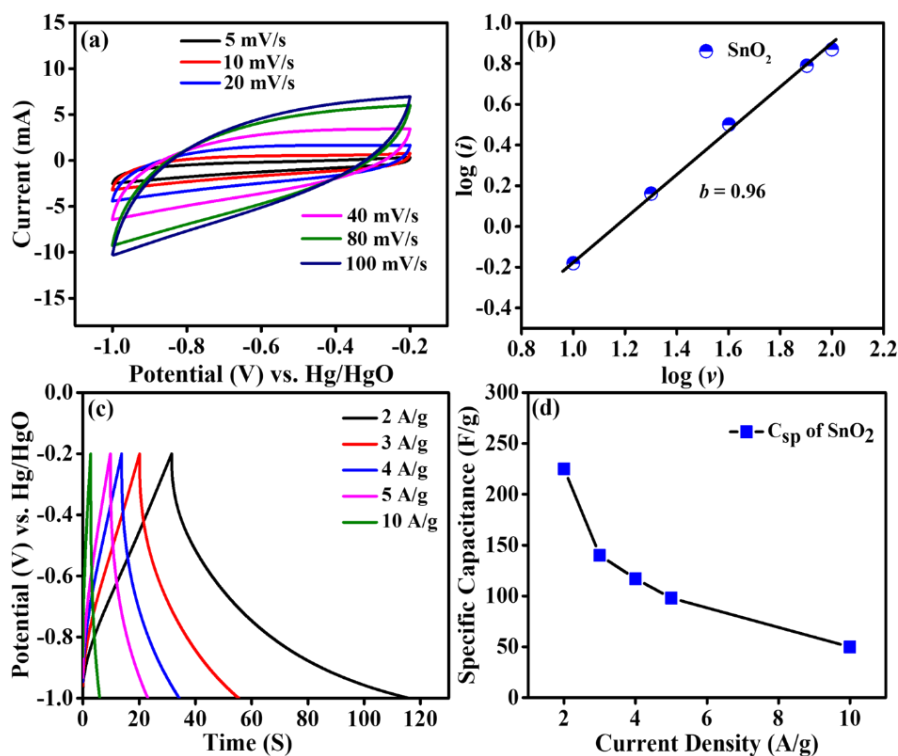
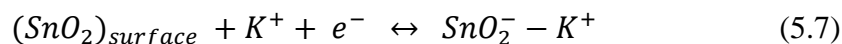


Figure 5.6 (a) CV curves of pristine SnO₂ (b) mechanism of charge storage process, (c) GCD curves of pristine SnO₂, (d) C_{sp} vs. current density.

The galvanostatic charge-discharge (GCD) for the pristine SnO₂ is carried out by employing a mass normalized current density ranging from 2 A/g to 10 A/g (Figure 5.6 (c)) and within a potential range of -1.0 to -0.2 V. The same GCD profiles were employed to calculate the specific capacitances of the as synthesized SnO₂. The GCD profiles displays asymmetric nature and have longer discharge time compared to the normal EDLC that again justifies the dominance of pseudocapacitive nature of the material. The specific capacitances were calculated using the formula presented in equation (5.1) and presented in Figure 5.6 (d). The highest specific capacitance value of 225 F/g is obtained at a current density of 2 A/g and retains only 23 % of its initial capacitance when the current density is increased to 10 A/g suggesting very low rate-capability of SnO₂. That can be further improved through hybrid formation with 2D layered Ti₃C₂T_x.

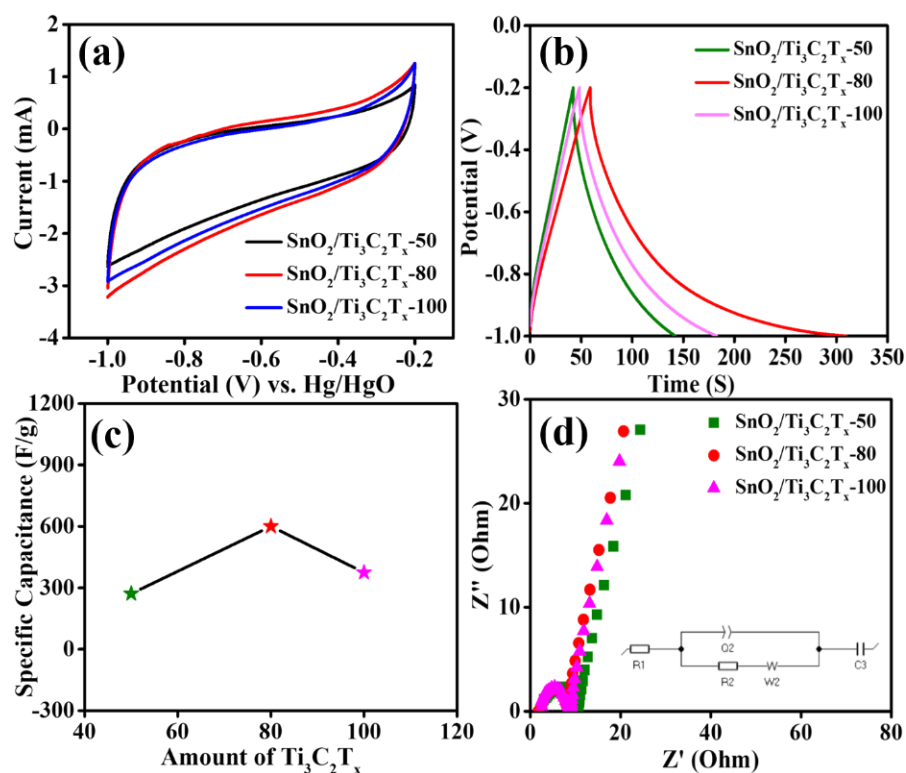


Figure 5.7 (a) CV at 5 mV/s and (b) GCD at 2 A/g for all the $\text{SnO}_2/\text{Ti}_3\text{C}_2\text{T}_x$ hybrids (c) C_{sp} values of all the hybrids at 2 A/g (d) EIS of all the $\text{SnO}_2/\text{Ti}_3\text{C}_2\text{T}_x$ hybrids

Although the fast-charging and slow discharging ability of pure SnO_2 in negative potential window is an attractive point but the lower specific capacitance and rate capability are vital limitations and need to be eradicated. Along with the enhanced hydrophilicity, high electronic conductivity, good redox chemistry and high chemical stability, cation intercalation/deintercalation during charge/discharge process in the layered $\text{Ti}_3\text{C}_2\text{T}_x$ provokes us to synthesize $\text{SnO}_2/\text{Ti}_3\text{C}_2\text{T}_x$ hybrid and study their electrochemical performance. A set of hybrids were synthesized by varying the amount of $\text{Ti}_3\text{C}_2\text{T}_x$ from 50 mg to 100 mg during the synthesis and were termed as $\text{SnO}_2/\text{Ti}_3\text{C}_2\text{T}_x$ -50, $\text{SnO}_2/\text{Ti}_3\text{C}_2\text{T}_x$ -80, $\text{SnO}_2/\text{Ti}_3\text{C}_2\text{T}_x$ -100. As presented in Figure 5.7 (a) $\text{SnO}_2/\text{Ti}_3\text{C}_2\text{T}_x$ -80 with largest CV area suggests the highest electrochemical activity towards supercapacitor application. Similarly, the GCD profiles in Figure 5.7 (b) tells us about fast charging and slow discharging ability of the material. From the GCD curves it's obvious that $\text{SnO}_2/\text{Ti}_3\text{C}_2\text{T}_x$ -80 having highest discharge time is one of the best performing electrode materials among all the hybrids. The GCD graphs were used to evaluate the specific capacitances of the hybrids. The specific capacitance vs. amount

of Ti₃C₂T_x curve displayed in Figure 5.7 (c) discloses that SnO₂/Ti₃C₂T_x-80 projects a maximum specific capacitance value of 620 F/g at 2 A/g while SnO₂/Ti₃C₂T_x-50 and SnO₂/Ti₃C₂T_x-100 delivers a specific capacitance of 271 and 374 F/g respectively at 2 A/g current density.

An AC frequency within a range of 100 kHz to 10 mHz with an AC amplitude of 5 mV is applied to record the electrochemical impedance spectroscopy of the hybrids at open circuit potential and presented in Figure 5.7 (d). The inset of Figure 5.7 (d) shows the corresponding equivalent circuit diagram. Small semicircles are obtained for all three hybrids. The 1st intercept between the semicircle and X-axis is defined as the equivalent series resistance denoted by R_s. The value of R_s is the combination of the electrode resistance, electrolyte resistance and contact resistance between electrode active material and current collector interface. The charge transfer resistance (R_{ct}) is represented by the diameter of the semicircle that signifies kinetics of the charge transfer between electrode and electrolyte interface. Lower the charge transfer resistance faster is the charge transfer. The equivalent series resistance of the hybrid was found out to be 2.7, 2.2 and 2.54 Ω for SnO₂/Ti₃C₂T_x-50, SnO₂/Ti₃C₂T_x-80 and SnO₂/Ti₃C₂T_x-100 respectively. The values of R_s for all the three hybrids are nearly equal reflecting uniform coating of all the hybrids on the graphite sheet current collector. On the other hand, the charge transfer resistances were observed to be 7.2, 5.2, 6.8 Ω for SnO₂/Ti₃C₂T_x-50, SnO₂/Ti₃C₂T_x-80 and SnO₂/Ti₃C₂T_x-100 respectively. Here, the smallest R_{ct} value for SnO₂/Ti₃C₂T_x-80 is 5.2 Ω indicates the faster charge transfer at the electrode/electrolyte interface compared to the other hybrids. Moreover, the Nyquist plot for all the hybrids possesses steeper rise in the low frequency region demonstrating the capacitive behaviour of the hybrid material. The synergistic interaction between Ti₃C₂T_x and SnO₂ not only lowers the R_{ct} value but also provides faster electrochemical kinetics at the electrode electrolyte interface, supporting the superior supercapacitor performance of SnO₂/Ti₃C₂T_x-80.

The electrochemical performance of SnO₂/Ti₃C₂T_x-80 is carried out in a potential range of -1.0 V to -0.2 V and in 3 M KOH electrolyte. The CV profiles in Figure 5.8 (a) were recorded at scan rate of 5 mV/s to 100 mV/s. With increasing the scan rate, the quasi-rectangular shape of the CV curves suggesting the reversible nature of SnO₂/Ti₃C₂T_x-80 at the applied potential window in KOH electrolyte. Here the logarithmic form of the power law has been employed to have a plot between $\log(i)$ vs. $\log(v)$, that

provides the value of $b = 0.98$ from the slope of the linear plot as shown in Figure 5.8 (b). The value of b for both pristine SnO₂ and SnO₂/Ti₃C₂T_x-80 is above 0.95 suggesting the mechanism of charge storage is purely capacitive in nature rather than battery type behaviour. Additionally, $b = 0.98 \approx 1$ proves that electrochemical activity towards supercapacitor performance of SnO₂ is greatly improved after formation of hybrid with Ti₃C₂T_x.

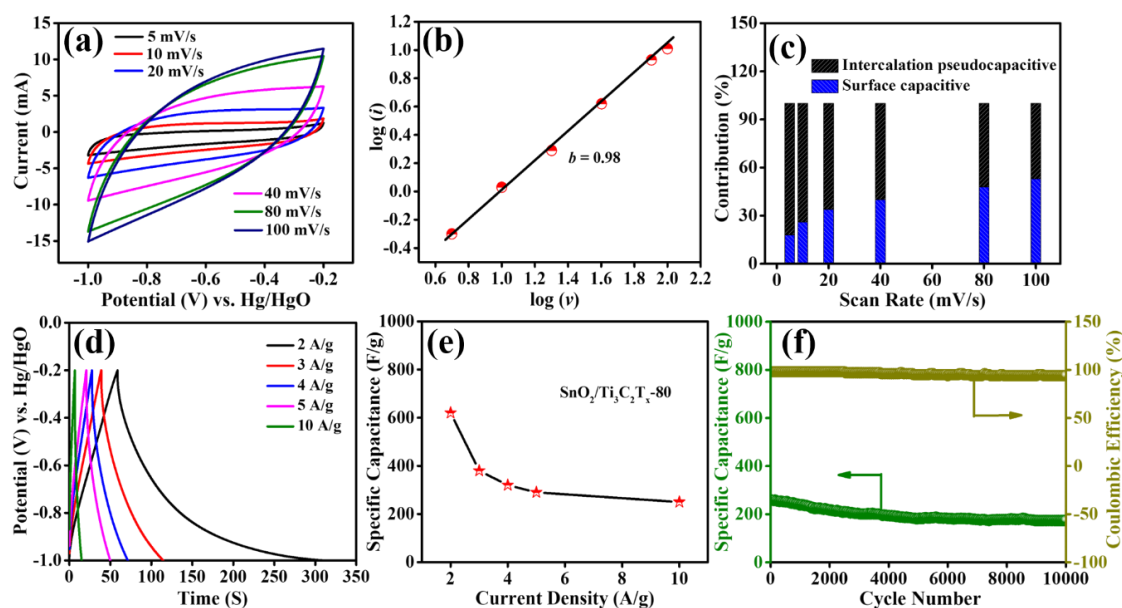


Figure 5.8 (a) CV curves of SnO₂/Ti₃C₂T_x-80, (b) charge storage mechanism determined by using power law, (c) percentage contribution towards total current calculated from CV profile, (d) GCD profiles of SnO₂/Ti₃C₂T_x-80, (e) specific capacitance vs. applied current density, (f) stability and coulombic efficiency after 10000 cycles of charge-discharge

Furthermore, to calculate charge storage contributions the current response in each CV curve is divided into two parts as presented in the equation below;

$$i(V) = k_1v + k_2v^{1/2} \quad (5.8)$$

k_1v and $k_2v^{1/2}$ are the current contributions at a particular potential that represents the surface capacitive process (EDLC and pseudocapacitance) and diffusion-controlled (intercalation pseudocapacitance) process respectively.³⁷ It is calculated using the above equation that at 5 mV/s the surface capacitive contribution of the current is 24 % and is increased to 53 % when the scan rate is increased to 100 mV/s. The Figure 5.8 (c) again represents the percentage contribution of the charge storage when the scan rate is gradually changed from 5 to 100 mV/s.

The GCD experiments for SnO₂/Ti₃C₂T_x-80 were carried out at an applied current density of 2 A/g to 10 A/g (Figure 5.8 (d)). At 2 A/g current density SnO₂/Ti₃C₂T_x-80 delivers a maximum specific capacitance of 620 F/g, while on increasing the current density to five times of its initial value the observed specific capacitance is 279 F/g the specific capacitance vs. applied current density curve is presented in Figure 5.8 (e) demonstrates the rate capability of SnO₂/Ti₃C₂T_x-80 is found out to be 45 %. The cyclic stability curves in Figure 5.8 (f) projects that the electrode material is subjected to a continuous charge-discharge cycles of 10,000 counts at 10 A/g current density. The electrode material (SnO₂/Ti₃C₂T_x-80) shows an excellent stability with 73 % retention in its initial capacitance and 94 % retention in coulombic efficiency suggesting no parasitic reaction occurs during the constant charge-discharge operation. The good redox chemistry and hydrophilicity of Ti₃C₂T_x and higher chemical stability of SnO₂ in alkaline media synergistically affect the rate capability and electrochemical stability of SnO₂/Ti₃C₂T_x-80.

5.7 Conclusion

we report a single step hydrothermal route to synthesize SnO₂/Ti₃C₂T_x composites with varying the amount of Ti₃C₂T_x (from 50 to 100 mg). After successful synthesis of the pristine SnO₂, Ti₃C₂T_x and SnO₂/Ti₃C₂T_x hybrids, the phase purity is confirmed through powder XRD analysis, the morphology was analysed through FESEM, TEM and HRTEM. FESEM images of SnO₂ reveals the agglomerated morphology that is further intercalated in between the Ti₃C₂T_x layers in the hybrid material. Moreover, the TEM image of SnO₂ disclose that the agglomerated architecture is actually the composed of small rice grain type nanoparticles. However, the interlayer spacing of Ti₃C₂T_x in SnO₂/Ti₃C₂T_x-80 hybrid is increased can be observed from HRTEM analysis. This increase in interlayer spacing again facilitates the charge transport in supercapacitor electrode.¹⁰ Afterwards the electrochemical study of SnO₂/Ti₃C₂T_x-80 shows better supercapacitor performance compared to pristine SnO₂, and other synthesized composites. In three electrode set-up SnO₂/Ti₃C₂T_x-80 delivers a specific capacitance of 620 F/g with a rate capability of 45 %. After 10,000 cycles of constant charge and discharge at 10 A/g, it was found that the electrode retains 73 % of its initial capacitance. Additionally, the electrode material delivers a highest energy density of 55.11 Wh/kg at a power density of 992 W/kg. These physicochemical and electrochemical studies reveals that the as synthesized hybrid material SnO₂/Ti₃C₂T_x-80 can be further used in the fabrication energy storage devices.

5.8 References

- 1 S. Fleischmann, J. B. Mitchell, R. Wang, C. Zhan, D. Jiang, V. Presser and V. Augustyn, *Chem. Rev.*, 2020, **120**, 6738–6782.
- 2 L. Yu, Z. Fan, Y. Shao, Z. Tian, J. Sun and Z. Liu, *Adv. Energy Mater.*, 2019, **9**, 1901839.
- 3 X. Geng, Y. Zhang, Y. Han, J. Li, L. Yang, M. Benamara, L. Chen and H. Zhu, *Nano Lett.*, 2017, **17**, 1825–1832.
- 4 P. Simon and Y. Gogotsi, *Nat. Mater.*, 2020, **19**, 1151–1163.
- 5 P. Simon, Y. Gogotsi and B. Dunn, *Science (80-.)*, 2014, **343**, 1210–1211.
- 6 M. Y. HO, P. S. KHIEW, D. ISA, T. K. TAN, W. S. CHIU and C. H. CHIA, *Nano*, 2014, **09**, 1430002.
- 7 Y. Zhang, Z. Hu, Y. Liang, Y. Yang, N. An, Z. Li and H. Wu, *J. Mater. Chem. A*, 2015, **3**, 15057–15067.
- 8 E. Samuel, B. Joshi, H. S. Jo, Y. Il Kim, M. T. Swihart, J. M. Yun, K. H. Kim and S. S. Yoon, *J. Alloys Compd.*, 2017, **728**, 1362–1371.
- 9 J. Li, X. Zhang, J. Guo, R. Peng, R. Xie, Y. Huang and Y. Qi, *J. Alloys Compd.*, 2016, **674**, 44–50.
- 10 R. B. Rakhi, W. Chen, D. Cha and H. N. Alshareef, *J. Mater. Chem.*, 2011, **21**, 16197.
- 11 Y. Luan, G. Nie, X. Zhao, N. Qiao, X. Liu, H. Wang, X. Zhang, Y. Chen and Y.-Z. Long, *Electrochim. Acta*, 2019, **308**, 121–130.
- 12 Y. Haldorai, Y. S. Huh and Y.-K. Han, *New J. Chem.*, 2015, **39**, 8505–8512.
- 13 C.-T. Hsieh, W.-Y. Lee, C.-E. Lee and H. Teng, *J. Phys. Chem. C*, 2014, **118**, 15146–15153.
- 14 Z. J. Li, T. X. Chang, G. Q. Yun and Y. Jia, *Powder Technol.*, 2012, **224**, 306–310.
- 15 M. U. Rani, V. Naresh, D. Damodar, S. Muduli, S. K. Martha and A. S. Deshpande, *Electrochim. Acta*, 2021, **365**, 137284.

- 16 B. Anasori, M. R. Lukatskaya and Y. Gogotsi, *Nat. Rev. Mater.*, 2017, **2**, 16098.
- 17 M. Alhabeb, K. Maleski, B. Anasori, P. Lelyukh, L. Clark, S. Sin and Y. Gogotsi, *Chem. Mater.*, 2017, **29**, 7633–7644.
- 18 M. Boota, B. Anasori, C. Voigt, M.-Q. Zhao, M. W. Barsoum and Y. Gogotsi, *Adv. Mater.*, 2016, **28**, 1517–1522.
- 19 Q. Liu, L. Zhou, D. Zhao, C. Wan, P. Sun, X. Lv, X. Sun and L. Fang, *J. Power Sources*, 2022, **533**, 231344.
- 20 G. Xi and J. Ye, *Inorg. Chem.*, 2010, **49**, 2302–2309.
- 21 M. Alhabeb, K. Maleski, B. Anasori, P. Lelyukh, L. Clark, S. Sin and Y. Gogotsi, *Chem. Mater.*, 2017, **29**, 7633–7644.
- 22 A. Padhy, R. Samal, C. S. Rout and J. N. Behera, *Sustain. Energy Fuels*, 2022, **6**, 2010–2019.
- 23 A. Padhy, R. Kumar and J. N. Behera, *Dalt. Trans.*, 2022, **51**, 16256–16265.
- 24 V. Schier, H.-J. Michel and J. Halbritter, *Fresenius. J. Anal. Chem.*, 1993, **346**, 227– 232.
- 25 O. Mashtalir, K. M. Cook, V. N. Mochalin, M. Crowe, M. W. Barsoum and Y. Gogotsi, *J. Mater. Chem. A*, 2014, **2**, 14334–14338.
- 26 J. Yan, C. E. Ren, K. Maleski, C. B. Hatter, B. Anasori, P. Urbankowski, A. Sarycheva and Y. Gogotsi, *Adv. Funct. Mater.*, 2017, **27**, 1701264.
- 27 B.-S. Shen, H. Wang, L.-J. Wu, R.-S. Guo, Q. Huang and X.-B. Yan, *Chinese Chem. Lett.*, 2016, **27**, 1586–1591.
- 28 A. Liu, M. Gao, X. Ren, F. Meng, Y. Yang, Q. Yang, W. Guan, L. Gao, X. Liang and T. Ma, *Nanoscale*, 2020, **12**, 10933–10938.
- 29 J. Zhao, L. Zhang, X.-Y. Xie, X. Li, Y. Ma, Q. Liu, W.-H. Fang, X. Shi, G. Cui and X. Sun, *J. Mater. Chem. A*, 2018, **6**, 24031–24035.
- 30 J. Guo, Y. Zhao, A. Liu and T. Ma, *Electrochim. Acta*, 2019, **305**, 164–174.
- 31 J. Halim, K. M. Cook, M. Naguib, P. Eklund, Y. Gogotsi, J. Rosen and M. W. Barsoum, *Appl. Surf. Sci.*, 2016, **362**, 406–417.
- 32 X. Liang, A. Garsuch and L. F. Nazar, *Angew. Chemie*, 2015, **127**, 3979–3983.

- 33 J. Guo, P. Li, L. Chai, Y. Su, J. Diao and X. Guo, *RSC Adv.*, 2017, **7**, 30070–30079.
- 34 J. K. Das, A. Padhy, S. Parida, R. M. Pathi and J. N. Behera, *Dalt. Trans.*, 2022, **51**, 11526–11535.
- 35 Y. Wang, Y. Song and Y. Xia, *Chem. Soc. Rev.*, 2016, **45**, 5925–5950.
- 36 Q. Wang, Y. Tian, S. Guan, Z. Peng and X. Fu, *ACS Appl. Energy Mater.*, 2020, **3**, 11333–11342.
- 37 J. Li, X. Yuan, C. Lin, Y. Yang, L. Xu, X. Du, J. Xie, J. Lin and J. Sun, *Adv. Energy Mater.*, 2017, **7**, 1602725.

SUMMARY AND FUTURE SCOPE

In conclusion, the thesis "Metal Phosphate and Oxide-Based Electroactive Material for Energy Conversion and Storage Applications" highlights the significant potential of metal phosphate and oxide materials in advancing energy conversion and storage technologies. Through comprehensive research and analysis, the thesis demonstrates that these materials exhibit remarkable electrochemical properties, including high specific capacitance, excellent cycling stability, and efficient energy conversion characteristics in terms of low overpotential, Tafel slope and high durability.

The investigation reveals that metal phosphate and oxide-based materials possess various advantages, such as low cost, abundant availability, and environmental friendliness, making them attractive candidates for next-generation energy conversion and storage electrode material. Their remarkable performance in oxygen evolution reaction and supercapacitor paves the way for efficient and sustainable energy conversion and storage solutions to address the growing demands of renewable energy, portable electronics, and electric vehicles. Moreover, the study highlights the importance of optimizing material synthesis methods and composite formation to enhance the electrochemical performance of these materials further.

Overall, this thesis contributes valuable insights into the field of electroactive materials for energy conversion and storage, providing a solid foundation for future advancements in the design and application of sustainable energy technologies. The findings from this research have the potential to revolutionize the energy landscape, contributing to a cleaner, more efficient, and sustainable future.